Faculty of Physics and Astronomy

University of Heidelberg

Diploma thesis

in Physics

submitted by

Sebastian Menk

born in Groß-Gerau

2009

A Cryogenic Trap for Fast Ion Beams

This diploma thesis has been carried out by *Sebastian Menk* **at the**
Max-Planck-Institut für Kernphysik
under the supervision of
Prof. Dr. Andreas Wolf

Kurzfassung

Eine kryogene Falle für schnelle Ionenstrahlen

Die kryogene Falle für schnelle Ionenstrahlen (CTF) wurde gebaut, um Kühltechniken und thermische Isolationsmethoden von ionenoptischen Elementen für die Entwicklung des elektrostatischen kryogenen Ionenspeicherrings (CSR) zu untersuchen. Diese herausfordernden Projekte werden ein neues Feld im Rahmen von Experimenten mit Ionen bei keV-Energien in der Atom- und Molekülphysik eröffnen. Die ultra-kalten Bedingungen von 2-10 K reduzieren die Schwarzkörperstrahlung und führen zu extrem geringen Restgasdichten (entsprechend einem Druck von $\approx 10^{-13}$ mbar bei Raumtemperatur), welches in langen Speicherlebensdauern und für Molekülionen in einem Kühlen der inneren Anregungen bis zum Rotationsgrundzustand resultiert.

Im Rahmen dieser Arbeit wurde der Zusammenbau dieser Ionenfalle vervollständigt, welcher unter anderem die Realisierung der Wärmestrahlungschilde, das Positionieren der Temperatursensoren und das Installieren von Hochspannungselektronik beinhaltet. Des weiteren wurden die ersten kryogenen Kühltests und der erste Speicherbetrieb von Ionen durchgeführt. Messungen der Speicherlebensdauer der Ionen wurden benutzt, um die Vakuumbedingungen im Fallenbereich unter kryogenen Temperaturen zu bestimmen. Zusätzlich wurden Simulationen der Ionenoptik mit SIMION durchgeführt, um die Eigenschaften der experimentell ermittelten Fallen- und Injektionseinstellungen genauer zu charakterisieren.

Abstract

A Cryogenic Trap for Fast Ion Beams

The Cryogenic Trap for Fast ion beams (CTF) was built to explore cooling techniques and test thermal decoupling of ion optics for the development of the electrostatic Cryogenic Storage Ring (CSR). These challenging projects will lead to a new experimental field within atomic and molecular physics with keV ion beams. The cold conditions of 2-10 K minimize the blackbody radiation field and are expected to lead to extremely low restgas densities (equivalent pressure at room temperature $\approx 10^{-13}$ mbar) which result in long storage lifetimes and the opportunity for molecular ions to radiatively cool to their rotational ground states.

In this work, the final assembly has been accomplished consisting of the mounting of radiation shields, temperature sensor positioning as well as installing high-voltage electronics. Furthermore, the first cryogenic cooling tests and ion trapping have been performed. The measurements of the trapped ion storage lifetime have been used to determine the vacuum conditions in the trapping area at cryogenic temperatures. In addition, simulations of the ion optics have been performed with SIMION in order to characterize more precisely the trapping and injection properties for the experimentally derived settings.

Contents

1. Introduction and Motivation

The opportunity to store energetic ion beams opens a considerable field of physical experiments such as fundamental research in atomic, molecular, optical and nuclear physics. It also overlaps with other scientific fields like chemical reactions and radiative transitions in astrophysics or biophysics. Dependent on the vacuum conditions in the experimental region and the used types of particles, the ion beam can be stored for several seconds or minutes.

The required devices such as heavy-ion storage rings and ion beam traps have been developed out of the fields of high-energy accelerator rings and low-energy ion traps. One advantage of ion storage in energy ranges of keV up to tens of MeV is the observation of long time developments, for instance, to perform lifetime measurements of metastable states or radioactive isotopes. During storage time an improved beam preparation can be accomplished like the cooling of internal degrees of freedom or external phase space cooling to reach well defined ion properties as low-excited stats or precise energy distributions. A further use is to investigate fragmentation or pickup-reactions of particles in fast motion such as for example recombination processes in an overlapped electron beam. Also photodissociation or photoionization studies with crossed or merged laser beams are performed.

The various assets and drawbacks between heavy-ion storage rings and ion beam traps cannot be exhaustively discussed in this work and, moreover, often depend on the particular experimental goal. A ring device obviously has the advantages of a fixed energy distribution around the circumference and the ability to include for example an electron cooler in order to prepare the stored ion beam. On the other hand, ion beam traps can be constructed with more compact dimensions and offer a more localized ion distribution.

1.1 Electrostatic storage devices

Heavy-ion storage rings have been mainly designed with magnetic bending and focusing elements and in practice were mostly used to store high energetic ions down to about 1 MeV of kinetic energy due to the decreasing stability of low magnetic fields. Furthermore, the requirement of investigations with massive particles like clusters or biomolecules has initiated the development of electrostatic storage devices whose storage capabilities are basically mass independent [1]. Comparing the bending radii R_M and R_E of ions in a magnetic and electrostatic device, respectively, which are given by

$$R_M = \frac{1}{q\,B}\sqrt{2\,m\,E_{kin}}\,, \tag{1.1}$$

$$R_E = \frac{1}{q\,E}\,2\,E_{kin}\,, \tag{1.2}$$

the electrostatic case is independent of the ion mass m and only dependent on the kinetic energy E_{kin} and charge q. Besides the higher range of ion masses, another advantage of electrostatic storage is the possibility to confine different particle species with identical energies at the same time. Furthermore, the electrostatic storage rings have a more compact size and require no high energy accelerators due to their low storage energy.
Considering the larger energy range covered by storage devices, it is important to discuss the process limiting storage lifetime for various energies. For ion energies above the MeV range, the dominant process is the stripping on restgas particles which changes the ion charge state and modifies their bending radius. In contrast, for lower energies the electron capture and multiple scattering processes gain more importance. Based on the generally higher cross sections of these loss processes with decreasing energies, the storage lifetimes for slower beams often become smaller. As all the loss mechanisms are dependent on the residual gas density, electrostatic storage devices require improved vacuum conditions to reach long storage times.
The first electrostatic storage ring for heavy ions, ELISA (Electrostatic Ion Storage Ring, Aarhus), was built in 1998 in Denmark [2], followed by the KEK ring in Japan created in 2002 [3]. All the currently existing rings have a very similar layout consisting of two 180° corners and two straight sections for experiments.
The design of the electrostatic ion beam trap, which was used in the cryogenic device of this work, was developed in Israel [4] and presently several of these traps are operated for example in Rehovot (Israel) or on the free electron laser (FLASH) in Hamburg (Germany) [5]. However, for all of them exclusively a room temperature operation is possible.

Investigations on these devices has been performed in various fields of physics like lifetime measurements of metastable states [6], impact detachments with a crossed electron beam [7] as well as mass spectroscopy measurements with a very high precision [8].

1.2 Cryogenic ion storage

The usage of the previously mentioned devices at cryogenic temperatures offers two essential improvements through extremely high vacuum conditions and an extensive reduction of the blackbody radiation acting on the stored ions. On the other hand, the realization of suitable cryogenic devices poses a number of challenges.
Starting with improved pressures, a device whose experimental chamber has been cooled to temperatures of a few Kelvin, is operating like a huge cryo pump which adsorbs the remaining rest gas particles on the cold surfaces due to a condensation or deposition process. For the main components in air like nitrogen, oxygen, argon as well as water or hydrocarbons, temperatures of 10 Kelvin are sufficient to initiate the adsorption. In contrast, hydrogen, the remaining component, requires temperatures of at least 2 Kelvin to reach room temperature equivalent pressures of 10^{-13} mbar. The partial vapor pressure of hydrogen decreases in this temperature range by several orders of magnitude and with a sufficient amount of 2 Kelvin surfaces inside the vacuum chamber, the desired pressure can be achieved. As the main ion storage loss processes are dependent on the pressure, the storage lifetime can be decisively enhanced.
The second improvement due to cryogenic temperatures is provided by the low blackbody radiation background for the stored ions. In exclusively all magnetic storage rings an electron cooler has been included where merged ion and electron beam perform phase space cooling and also cooling of the internal vibrational states of stored molecular ions [9]. Electronic excitations of the ions as well as ro-vibrational excitations of infrared active molecular ions will decrease due to radiative relaxation during the storing process. Rotational excitations below roughly 25 meV stay unaffected in a room temperature environment and cooled states can also be additionally excited again by the high radiation background.
The low radiation background in a cryogenic device decrease the re-excitations and by means of the low pressures with corresponding long storage lifetimes, the ions can finally reach their internal ro-vibrational ground states. For experiments, the well defined ground state of the ions provides the opportunity to observe low-energy excitations and allows to reproduce condition as they are found in interstellar space.

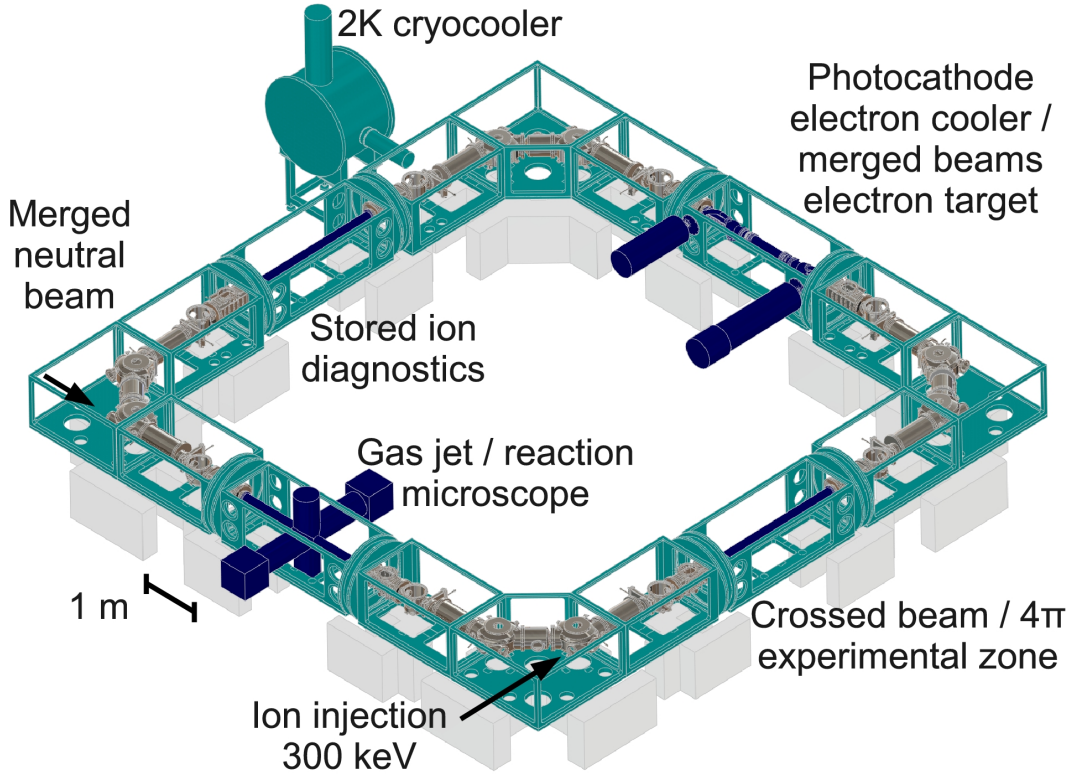

Figure 1.1: *Schematic view of the electrostatic Cryogenic Storage Ring (CSR) including the refrigeration system, the electron cooler as well as the reaction microscope*

1.3 Principle of the CSR and motivation for the CTF

The project of a Cryogenic Trap for Fast ion beams (CTF) ([10],[11]) has been created to explore the cooling techniques and test the thermal decoupling of the ion optics for the development of the electrostatic Cryogenic Storage Ring (CSR) ([12],[13],[14],[15]). For this trap, several concepts of thermal isolation or cooling principles are implemented which are very similar to the design of the CSR. The CSR will use the same closed-cycle refrigeration system to achieve the cryogenic temperatures, which produces superfluid helium at temperatures below 2 Kelvin. The radiation shielding and thermal insulation via an isolation vacuum surrounding the experimental vacuum are also concepts both devices have in common.

The CSR will be a new unique device which includes all the advantages of electrostatic ion storage, cryogenic temperature induced extremely high vacuum conditions, as well as

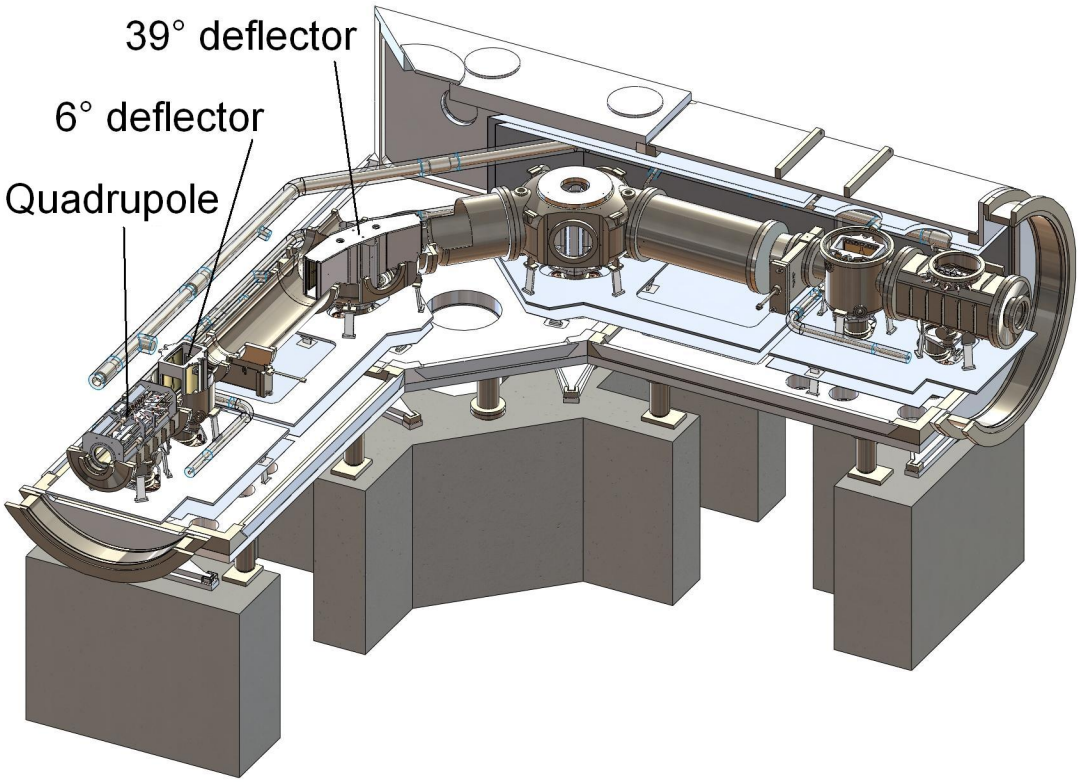

Figure 1.2: *Current design of one CSR corner including the two 39° and 6° deflectors, the quadrupole lenses as well as the parts of the isolation vacuum chamber and radiation shields*

a reduced blackbody radiation incident onto stored ions. The energy range of the stored atomic and molecular ions up to clusters and biomolecules will be in the region of 20-300 keV. The device is currently under construction and the assembly beginning with the first corner close to the refrigeration system will start in May 2009.

Unlike all other electrostatic storage rings, the CSR will consist of 4 straight sections for experiments and diagnostics. Besides a reaction microscope and a beam observation section, the first electron cooler to operate at this low ion energy range will be included. Using these elements, various experiments with electrons, lasers or neutral particles are possible whether in a crossed or merged beam configuration. For the corners a combination of two electrostatic 39° deflectors, two 6° bending electrodes and two quadrupole lenses will be used.

The experimental vacuum chamber is surrounded by two layers of radiation shields cooled to 40 and 80 Kelvin, respectively, and many layers of super insulation, all of which are contained inside a huge isolation vacuum chamber. Two closed-cycle helium pipe systems are used to cool the experimental chamber as well as the radiation shields using helium

in a superfluid state at 2 Kelvin and 5 Kelvin in gas phase, respectively. Special copper blocks will be used as a cryogenic hydrogen pump which have direct contact with the superfluid helium on one side and reach into the high vacuum chamber with the other side.
Figure 1.1 shows a schematic layout of the current CSR design and figure 1.2 gives a detailed view of one corner including on the right side the inner cold chamber, parts of the radiation shields and isolation vacuum chamber. The left part of the CSR corner allows an inside view on the ion optics like the 39° and 6° deflectors and shows a helium pipe to cool the chamber.
The CTF was built as a prototype in order to develop the techniques and methods which are necessary to construct the CSR. In addition, this device also creates a new field of possible experiments and will therefore continue to be used after the initial tests.
The verification of the cryogenic cooling principles in terms of material and quantity of cooling connections, the thermal isolation concept, and the realization of the estimated cryogenic temperatures are some of the goals. Moreover, the determination of the extremely high vacuum of 10^{-13} mbar (room temperature equivalent) is one of the first aims that has to be proven by measuring the storage lifetimes of the trapped ions. Due to the fact that pressures in this low range can not be measured with available pressure gauges and furthermore, the included ion gauges inside the cold chamber can not be operated at cryogenic conditions due to the increased heat input, the remaining possibility is the pressure estimation by the linear dependence of the inverted storage lifetime on the pressure.

2. Principle of a linear ion trap

This chapter describes the properties of the linear electrostatic ion beam trap by using simulations performed with SIMION to predict stable trap settings or verify those which have been experimentally obtained. Furthermore, the dominant loss processes in the ion trap are introduced where the electron capture process was used to measure the storage lifetime of the trapped ions and estimated the vacuum.

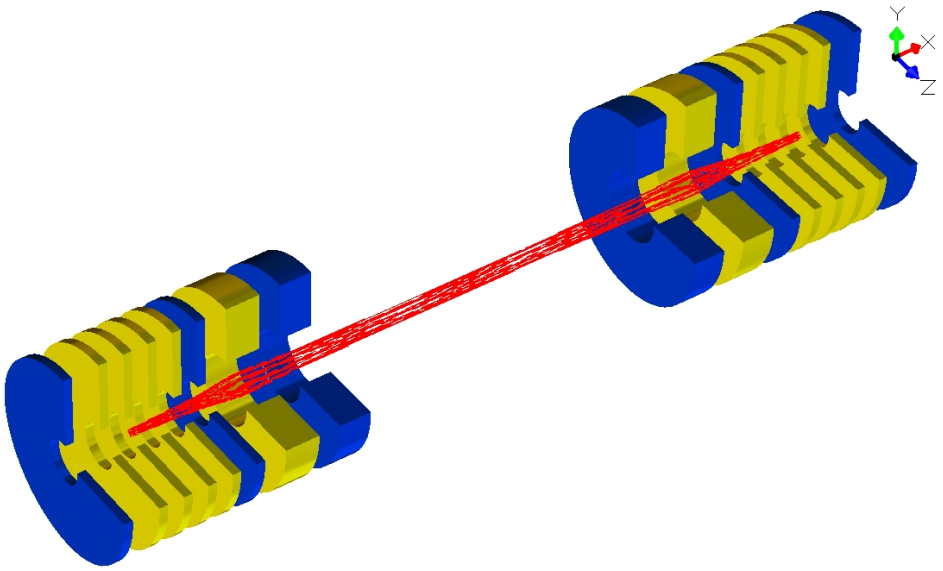

Figure 2.1: *Schematic view of the electrostatic ion beam trap consisting of two stacks of mirror electrodes. Voltages of up to 30 keV can be applied to the yellow electrodes whereas the blue ones are always grounded. The trapped ion beam is shown in red.*

2.1 Trapping of fast ions

This section describes the general properties of an electrostatic linear ion beam trap [4]. This type of ion trap gives the opportunity to store high energetic ions with energies in the order of 2 to 20 keV which, for example, corresponds to velocities of 100-400 $mm/\mu s$ for singly charged molecular nitrogen N_2^+. In the electrostatic trap ions are stored between two electrostatic mirror electrodes each of which consists of eight metal rings. These stacks act as mirrors where the ions are decelerated and accelerated back towards the other side.

All electrode rings have an outer diameter of 200 mm, whereas the inner diameter varies from 40 to 64 mm (see fig. 2.2). The outermost electrodes (H) are grounded and thereby, shield the charged electrodes from the outside of the trap. The position of the next four electrodes (D-G), especially the outer two of these, is the region where the ions get decelerated to an almost vanishingly small kinetic energy. To these four electrodes, voltages of up to 30 kV can be applied independently, thereby reaching a well controlled potential shape. Shifting the height of this potential changes the path length of the trapped ions. By varying the slope of the potential one can also modify the path length for different kinetic energies of the ions. This fact provides the opportunity to create some interesting effects like the so called self-bunching mode where the space charge induced broadening of an ion bunch gets compensated by the shape of the reflection potential.

The inner three electrodes (A-C) function as an internal trap einzel lens. The outer electrodes are grounded, whereas the inner one focuses the beam into the reflection potential and in the outer direction providing a nearly parallel beam towards the other mirror electrodes.
For injection, one of the electrode stacks is grounded to allow the entrance of the ions. The voltages are then quickly switched to the same values as the other stack, thereby trapping the ions between both electrode stacks. In the case of singly charged molecular nitrogen, the revolution time in the trap is a few microseconds. So to reach a nearly filled trap the time constant τ_C of the voltage switching has to be in the order of some hundreds of nanoseconds. The definition of the time constant τ_C is given in equation 2.1 by the time dependent electrode voltage:

$$U(t) = U_0 \cdot (1 - e^{-\frac{t}{\tau_C}}) \,. \tag{2.1}$$

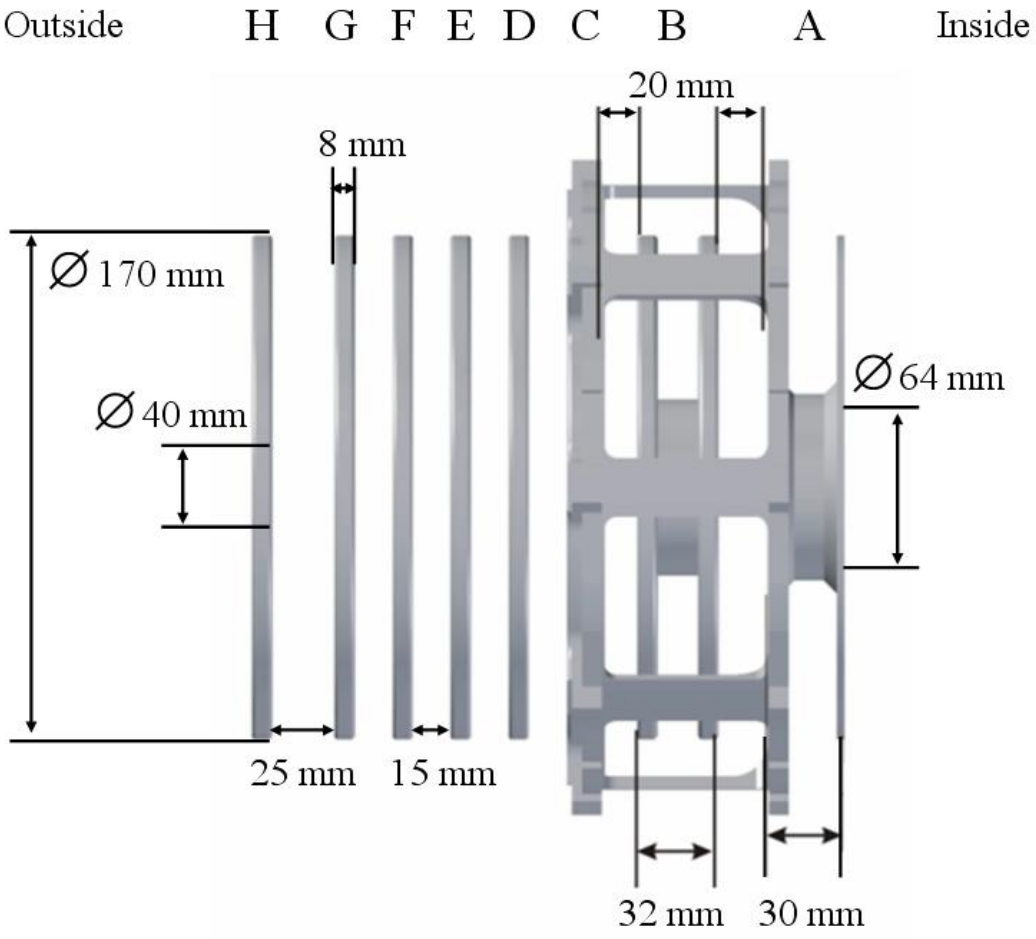

Figure 2.2: *One electrode stack composed of 8 ring-shaped plates. The trap center is located on the right hand side.*

2.2 Dynamic trap simulations with N_2^+

This section describes the properties such as energy or position of the trapped ions in SIMION ([16]) simulations with singly charged molecular nitrogen N_2^+. The electrode potentials for these simulations were developed by optimizing the actual voltages with respect to the storage lifetime and number of trapped ions in the performed experiments.

2.2.1 SIMION simulations for the linear electrostatic ion trap

The trap model which has been used for the simulations consists of all of the 16 cylindrical mirror electrodes surrounded by a cylinder barrel which defines the border of the grounded vacuum chamber. The grid size for the simulation was chosen to be one millimeter. As

the electrodes in the simulation can not easily be switched on after the injection, the initial start position of the ions was the trap center, the field free region, and the voltages are always applied.
Desired values like the position, velocity or energy can be recorded as a function of the time of flight and stored in a data file for later use and analysis. It is, thereby, possible to start several ions at the same time by scanning through one or more values, so that one obtains a distribution of this value in one simulation. The coordinate system for all simulations was defined by having the injected beam flying in the positive x-direction. The two other perpendicular directions are y for the vertical direction and z for the horizontal. Most of the simulations are only using x and y since the trap electrodes are symmetric.
In the following, some results of the simulation are shown which not only helped to understand the movement of the ions in the trap but also made predictions comparable to the experiment or the other way around.

2.2.2 The electrode potential

Figure 2.3 shows the characteristic shape of the trap potential along the axis of the trap and as the electrodes have a ring profile, the whole potential is radially symmetric. In this case, the optimized potential for the storage of ions with 7.1 keV kinetic energy is displayed. Electrode G has a voltage of 9.25 kV which is high enough to store the ions along the axis of the trap. To focus the beam after the reflection into the other part of the trap, the einzel lens or electrode B, is applied with a voltage of 6.55 kV. The complete set of voltages starting with electrode A (the inner most) is $\{V_A, ..., V_H\}$=$\{$0, 6.55kV, 0, 2.53kV, 4.73kV, 7.57kV, 9.25kV, 0$\}$.

2.2.3 Ion trajectories and transversal phase space

As this symmetric ion trap is of the cavity-type there is an obvious analogy to classical optics. Thus, similar to an optic resonator one can give a condition of stability which the beam of ions has to fulfill to be trapped ([4]):

$$\frac{L}{4} < f < \infty \tag{2.2}$$

where L is the distance between the two mirrors, and f the focal length.
For electrode potentials which fulfill this condition, some ion trajectories in the position space are shown in figure 2.4 (left panel). In each of the simulations the pathway of one

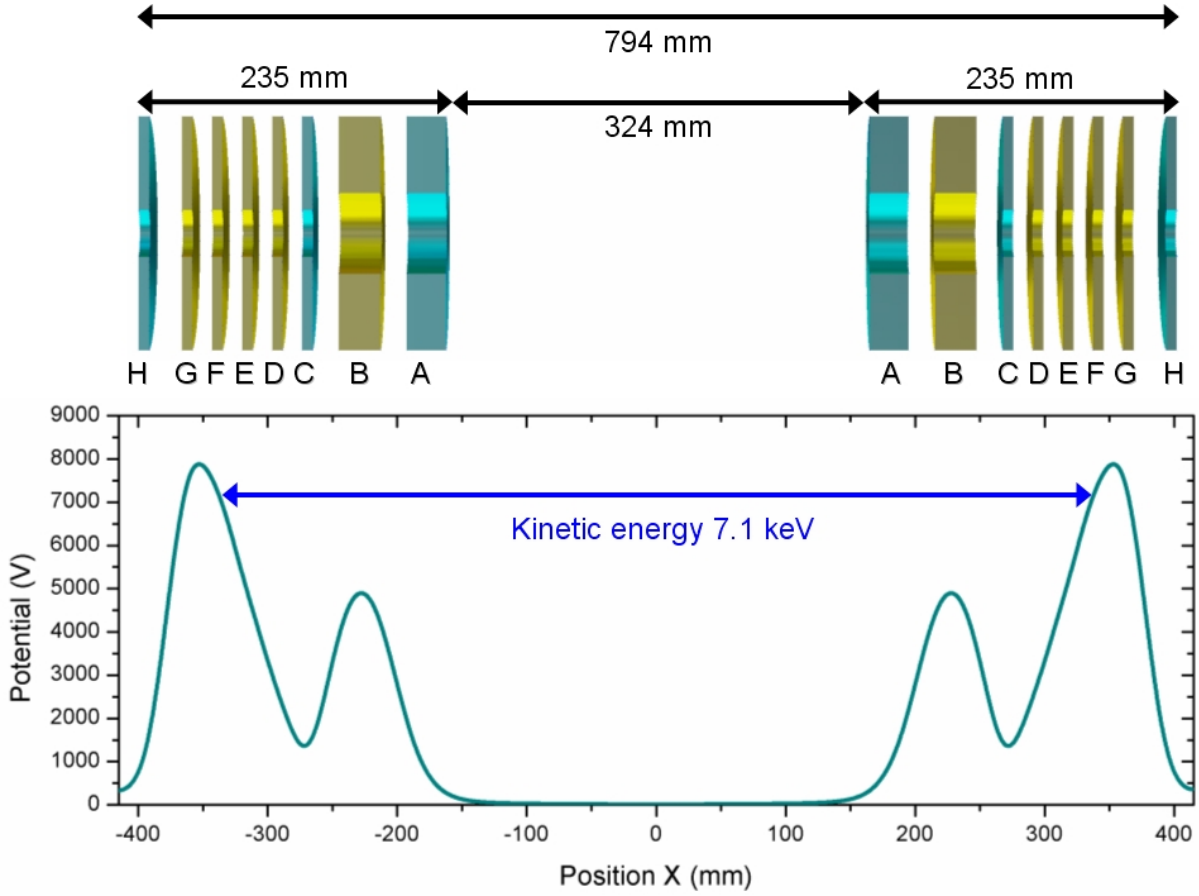

Figure 2.3: *Electrode potential for 7.1 keV ion energy. Yellow marked electrodes are at high voltage, green electrodes are grounded.*

ion is shown over a hundred revolutions. The difference in the three trajectories is the maximal distance to the ideal path in the center of the trap. Even for beam sizes with 10 mm diameters there are stable trajectories possible in the trap.

While the trajectories (a) and (c) differ mainly by their maximum distance from the axis, trajectory (b) is a special case of ion movement in the trap. The very localized path of the ions leads to a resonant movement and thereby to an unstable trajectory. This will be discussed in more detail later when the islands in the phase space and the tune are introduced.

Phase space is normally defined by the position and the momentum. For particles in a beam, it is also often represented by the transversal angle y' related to the momentum component along y by $p_y = y' \cdot p_0$, where p_0 stands for the larger longitudinal momentum. As it is usually used in storage ring physics, the transversal position y and the angle y' are

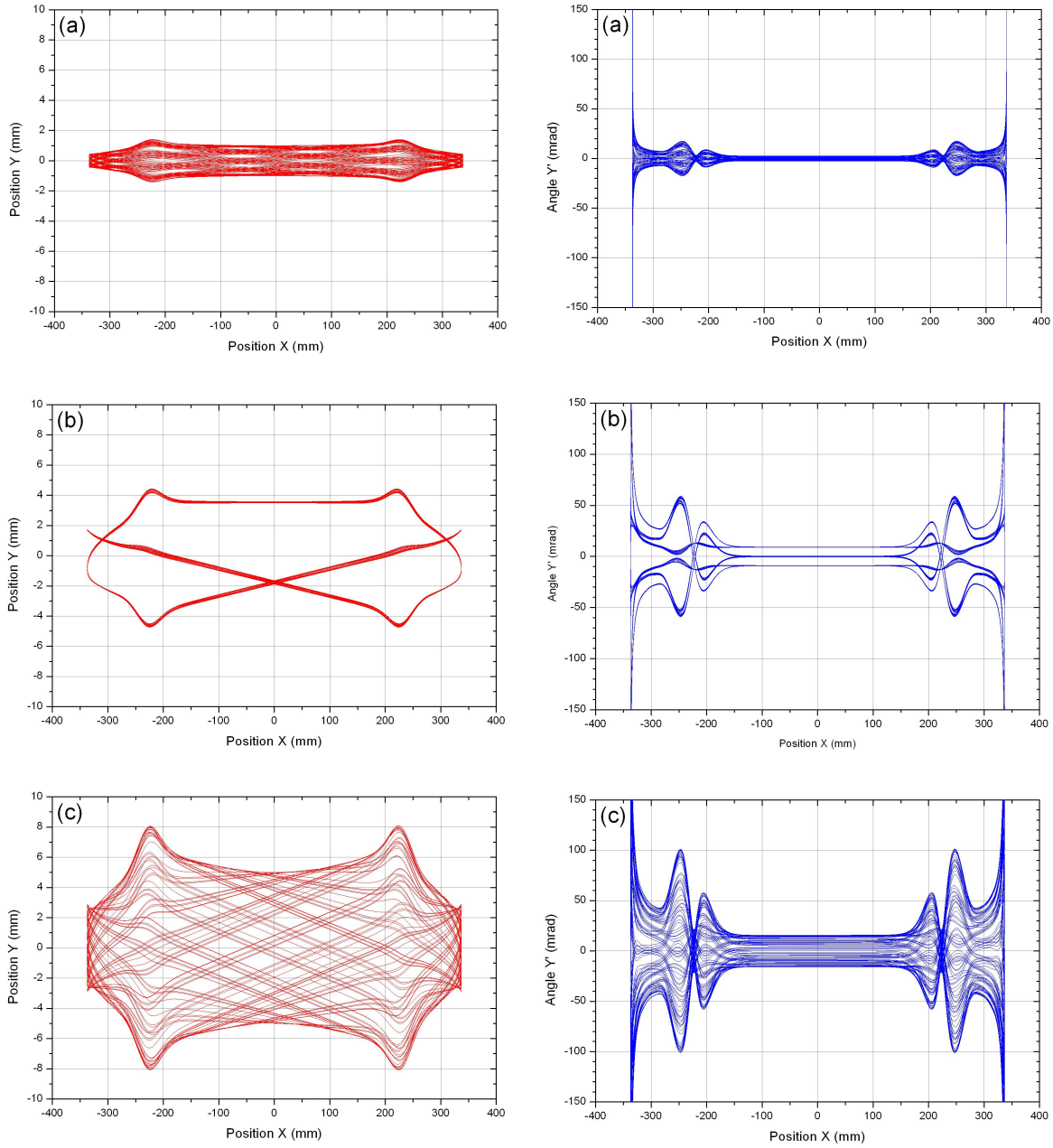

Figure 2.4: *Ion trajectories in the position space (y,x) (left panel) and transversal angle y' (right panel). The x direction is the main direction of the ion beam in which the majority of the kinetic energy is stored. Each of these simulations show the path of one ion during 100 revolutions. From trajectory (a) to (c) the maximal transversal variation in y-direction to the center path changes from 1 to 5 mm.*

used to create a transversal phase space. The angle y' is defined as the derivation of the transversal direction y with respect x. The very small transversal variations compared to the longitudinal movement depend linearly on the transversal momentum p_y:

$$y' = \frac{dy}{dx} = \frac{p_y}{p_x} \approx \frac{1}{v} \cdot v_y = \frac{1}{p} \cdot p_y. \tag{2.3}$$

It is important to note that as the potential is radially symmetric the trajectories and the phase space for the second transversal direction z are identical to y. Instead of y one could also use a radial direction r, but the y direction has the advantage of being exactly defined in space.
The corresponding transversal phase space of the ion trajectories is shown in figure 2.5. This diagram is created by plotting the position and the angle of the ions for successive passages through the mid plane in the free space between the mirror stacks, $x = 0$, defined as the center of the trap, and taking only passages with positive velocity v_x. For instance, ions in the center of the phase space belong to a short distance to the beam axis and a small angle, respectively.
In this figure each ellipse corresponds to one ion oscillating in the trap for a hundred times. Thereby, the ion is changing its position in the phase space by larger factors but it always stays on the same ellipse. So the movement in the phase space does not correspond to a continuous change of the values rather more to a jumping in the phase space.
The three red marked curves belong to the trajectories (a)-(c) in figure 2.4. The inner and outer of these trajectories are forming closed orbits in the phase space, whereas trajectory (b) shows a localized distribution which is limited to three positions in the phase space.
Without any perturbations or scattering effects, the ions always stay on the same orbit which gives the opportunity to define an ion trajectory by the maximum transversal variation $\hat{y}$. For the three example trajectories (a)-(c) these values are given by $\hat{y}_a = 1$ mm, $\hat{y}_b = 3.5$ mm and $\hat{y}_c = 5$ mm.

2.2.4 The Tune in a linear electrostatic ion trap

At this point the introduction of the tune Q will lead to a better understanding of the ion movement. The tune is an important value in storage ring physics and one can transfer it to ion beam traps. It is defined as the number of betatron oscillations per revolution of one ion in the trap. Thereby, the betatron oscillation is the transversal motion of the ions with respect to their major movement and is generated by the focusing properties of the trap electrodes. The tune is roughly in the order of 1 to 2 and strongly dependent on

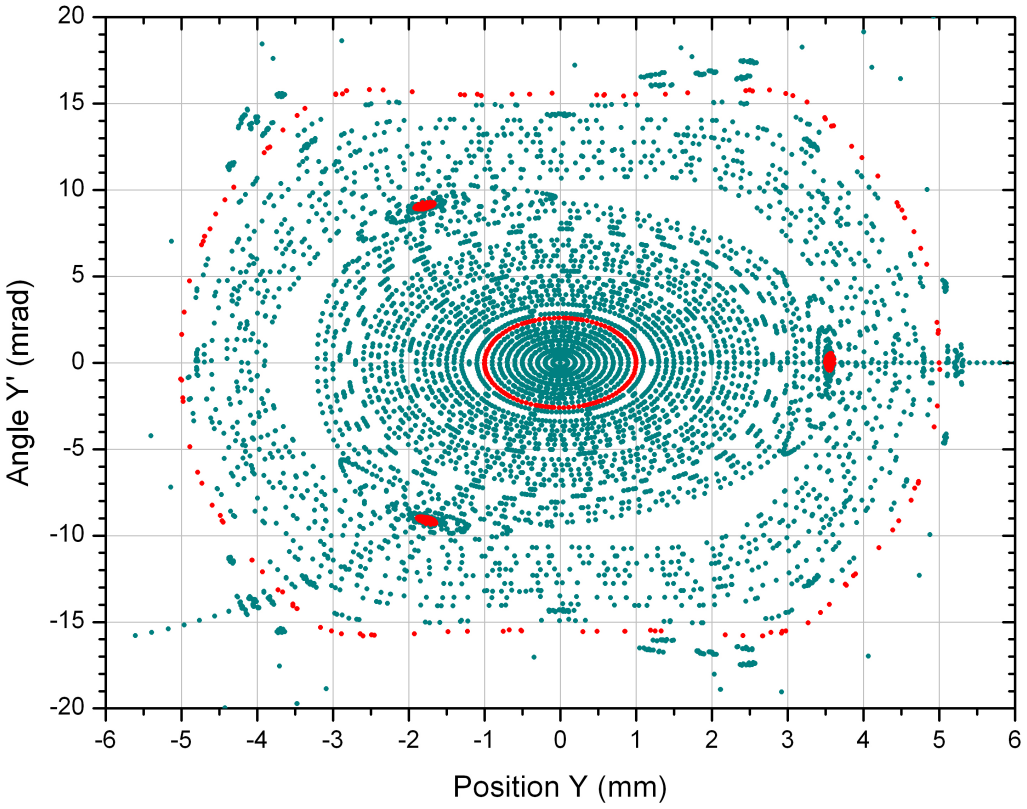

Figure 2.5: *Transversal phase space (y,y′) in the center of the trap for an ion energy of 7.1 keV. The three trajectories of figure 2.4 are marked in red: The inner ellipse corresponds to (a), the three small islands to (b), and (c) is the outer red path.*

the energy and the distance of the ion trajectory to the center path.
Especially, for an integer tune this ion trajectory leads to a strong resonant movement in the trap. Thereby, the ion stays on a localized path and notices iteratively each local periodic perturbation. These influences on the path will be amplified until the ion is kicked out of the stable trap region. The strongest resonances will occur for integer values of the tune but also half-integers and thirds lead to unstable trajectories through resonances. Therefore, one aims at achieving a non-rational number of Q. However, at first, it will be illustrated how the tune can be calculated with the help of simulations.

$$y(n,x) \;=\; y_0(x)\, sin(2\,\pi\, Q_y\, n \;+\; \phi) \tag{2.4}$$

Equation 2.4 shows the transversal position y of the ion dependent on the number of revolutions n as well as the longitudinal position x. At first, one needs a position in the longitudinal direction to observe the ion movement. This was chosen to be the trap center.

Plotting the transversal direction y versus the number of revolutions n and fitting a sinus wave leads to the floating point fraction q_y of the tune. The smallest positive value is usually chosen by the fitting program. The integer part is not accessible by this method since the sinus is, due to its periodicity, not determined for phases of 2π. In addition, the relation $sin(\alpha) = -sin(-\alpha)$ shows that the tune Q_y is just defined by

$$Q_y \, = \, n_y \, \pm \, q_y \, , \tag{2.5}$$

where n_y is the integer part and q_y the floating point fraction of the tune.
The integer part and the sign can be accessed by plotting the transversal position y in the course of time. Roughly, the number of oscillations in one revolution can be determined by counting the number of zero-crossings. For an even number, for example 2, the tune has to be between 1 and 1.5 because the ion performs slightly more than one betatron oscillation per trap revolution. In this case, the integer part is 1 with a positive sign in equation 2.5. Odd numbers like 3, for instance, correspond to a tune between 1.5 and 2, and here the integer part is 2 with a negative sign.
After the tune is determined with the help of simulations it can be observed for different oscillation amplitudes for orbits up to ≈5 mm. Figure 2.6 shows the tune depending on the maximum transversal variation $\hat{y}$ of the trajectory which defines the populated ellipsis in the transversal phase space. The tune increases with $\hat{y}$ which can be explained by considering non-linearities in the focusing potential. Due to the higher electric field close to the electrodes, trajectories with larger distance y receive deflection forces which are stronger than linearly dependent on y. According to this increased deflection, the transversal oscillation frequency gets higher and the tune rises with larger distances.
Furthermore, in this distribution, the tune crosses the value of 4/3 which has been previously found to be a resonant value. The corresponding position y is 3.5 mm which exactly fits to the position of the right island in the transversal phase space diagram (compare fig. 2.5), and hence, to the trajectory in figure 2.4 (b). Compared to other trajectories, this one is limited to the three islands in the phase space and forms the described unstable resonant path.
In the next figure (2.7) the tune is shown for different ion energies and in addition for a band of trajectories $\hat{y}$ represented by the colors. The ion energy has been changed for this simulation, but the trap potential has always been the optimized for the energy of 7.1 keV.
Beginning at the left side, the tune decreases towards higher energies. Lower energy and velocity correspond to a longer duration in the electrode potential and lead thereby to a stronger deflection. Additionally, the ratio between deflection voltage and ion energy is

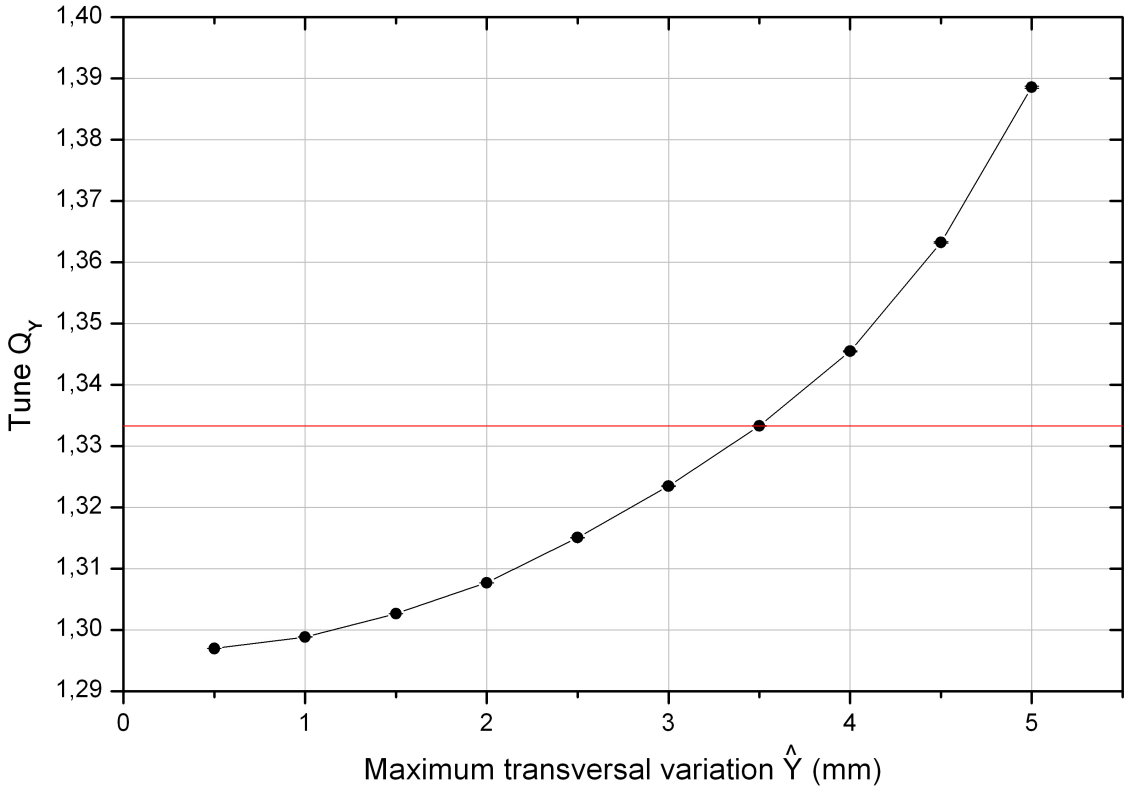

Figure 2.6: *The tune Q_y as a function of different trajectories which are defined by their maximal transversal variation $\hat{y}$ and with an ion energy of 7.1 keV.*

slightly higher for low energies.
On the side of high energies, another effect has to be taken into account and even overcompensates the decrease. For lower energies than the mean energy of 7.1 keV the potential at the point of return has a steep and constant slope (compare 2.3). The ion path length varies for different energies but the duration does not change appreciably. Ions with a higher energy dive deeper into the potential as it becomes more flat at the top. The duration in the potential gets longer and leads thereby to a stronger deflection.
An other important aspect is also that the critical value of the tune at 4/3 is moving for lower energies towards the center line of the trap. Hence, the inner stable region in the phase space which is far away from the critical tune in figure 2.5 becomes very small for slightly lower energies as for example 7.0 keV.
However, the characterization of ions in the trap is more difficult than for a storage ring, for instance, because the ions are more strongly focused and in particular they are decelerated almost to a zero kinetic energy. This fact also provokes difficulties for other

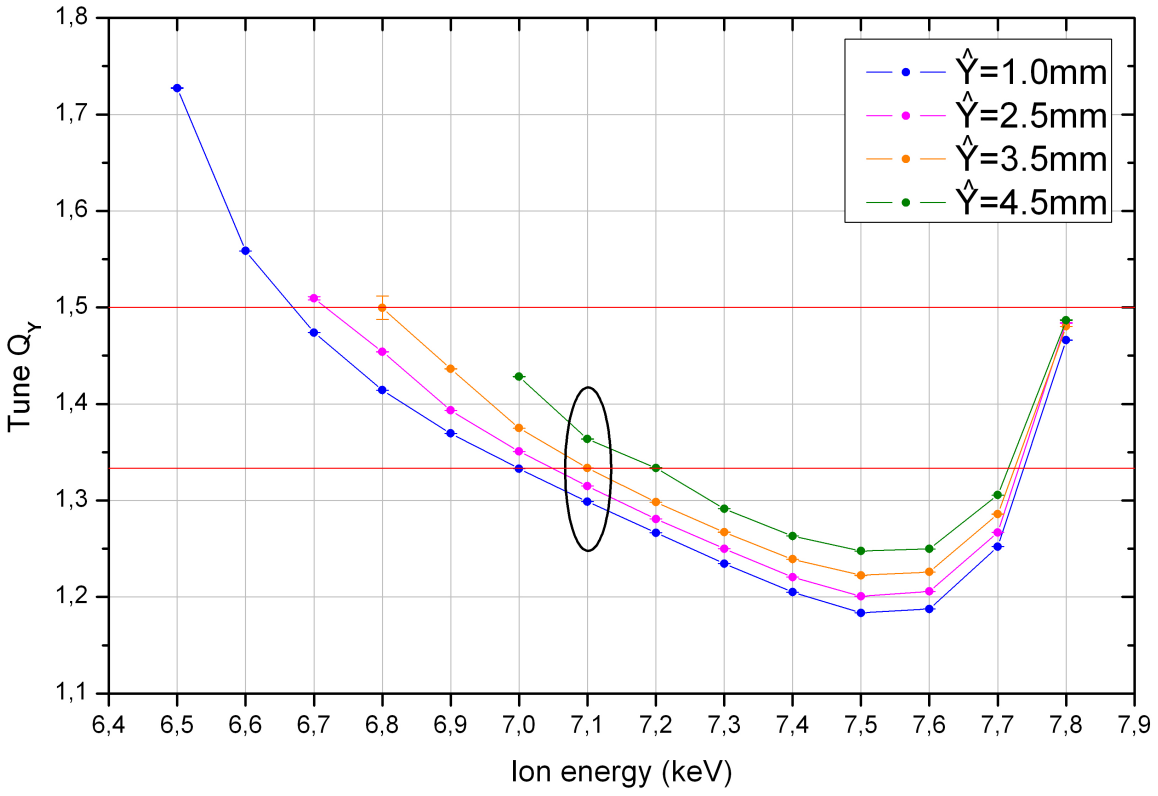

Figure 2.7: *The tune Q_y as a function of the ion energy and with different maximal transversal variations $\hat{y}$. The optimized trap potential used for ion energies of 7.1 keV.*

mathematical descriptions like the ion loss processes in the following section.

2.2.5 Oscillation frequency and the η parameter

The oscillation frequency of ions in the trap can only be observed by having a bunch of ions oscillating. The periodic signal produced by the bunch on a pick-up is used to estimate the oscillation frequency. The pick-up is a tube of 2 cm length and 4 cm diameter and is positioned in the center region of the trap (compare fig. 3.18). When the ion bunch passes through the pick-up a voltage is induced, afterwards amplified and conducted to a spectrum analyzer, where the signal is converted to a frequency spectrum by a Fourier transformation.

However, the ion bunch will lose coherence over time which is caused by two effects. The coulomb repulsion between the ion charges pushes them apart, and the finite width of

their kinetic energy distribution causes an additional spread of the bunch. At first, the dependency on the energy distribution will be introduced and the space charge effect will be neglected.
Using a step function as a simplified model for the potential, the ion oscillation frequency would change with the energy by

$$\Delta f \;=\; f_0 \,\frac{1}{2\,E_0}\,\Delta E, \tag{2.6}$$

where E_0 and f_0 are the mean energy and mean oscillation frequency of the bunch, respectively. In this case, the path length for one revolution is independent on the energy, the faster and slower ions would depart from each other and the bunch would spread out very quickly.
This effect, however, can be influenced by changing the path length for different energies in such a way that faster ions have a longer path and vice versa. This is automatically realized by the real potential of the trap even though the slope needs to have the correct shape to compensate a broad distribution of energies. Here, the path length is dependent on the ion energy and has to be taken into account.
In addition, the kinetic ion energy does not stay constant during one revolution. This can be included by using an average velocity $\bar{v}$. In general, the frequency is given by $f = \bar{v}/L$ and the corresponding variation by

$$\frac{\Delta f}{f} \;=\; \frac{\Delta \bar{v}}{\bar{v}} \;-\; \frac{\Delta L}{L}\,. \tag{2.7}$$

Here, the variation of the path length ΔL is a function of the trap potential at the point of return. Around the mean point of return $\tilde{x}_0$ for the mean energy E_0 the potential slope can be approximated with a linear dependence:

$$\Delta L \;=\; 4\,\frac{1}{\frac{\delta\phi(\tilde{x}_0)}{\delta x}\,q}\,\Delta E\,, \tag{2.8}$$

where q is the ion charge and $\delta\phi(\tilde{x}_0)/\delta x$ the gradient of the potential at point $\tilde{x}_0$.
Now the slipfactor η will be introduced which gives a direct indication if the bunch movement will disperse, converge or retain the initial shape. The η parameter is defined as the normalized ratio of oscillation frequency variation Δf and the energy variation ΔE and combined with equation (2.7) it can be written as

$$\eta_E \;=\; \frac{\Delta f/f_0}{\Delta E/E_0} \;=\; \frac{\Delta \bar{v}/\bar{v}}{\Delta E/E_0} \;-\; \alpha_E\,, \tag{2.9}$$

with

$$\alpha_E = \frac{\Delta L/L}{\Delta E/E_0} = 4\,\frac{1}{\frac{\delta\phi(\tilde{x}_0)}{\delta x}\,q}\,\frac{E}{L}\,. \tag{2.10}$$

The definition shows that if η equals zero for a certain energy, the frequency variation Δf has to vanish too. Due to this, the frequency for this energy is equal to f_0 corresponding to the mean energy E_0. For small values of η, ions with energies around E_0 have the same oscillation frequency and a bunch formed out of these energies retains the initial shape.
By using a scaling factor κ, the the average velocity $\bar{v}$ can be written as

$$\bar{v} = \kappa(E) \cdot v_{max}\,, \tag{2.11}$$

with the energy dependent scaling factor κ and the maximum velocity v_{max}.
Taking into account the variation of the average velocity as well as using equation (2.9), the complete slipfactor η_E for the linear ion trap becomes

$$\eta_E = \frac{1}{2} + \frac{\Delta\kappa/\kappa}{\Delta E/E_0} - \alpha_E\,. \tag{2.12}$$

A simulation of the oscillation frequency and the η parameter using the actual trapping potential is shown on figure 2.8 as a function of the ion energy. The mean energy is 7.1 keV and is marked in the diagram with the corresponding values for f and η. The trap potential is optimized with respect to this energy, and the η parameter is close to zero for this energy.
Furthermore, if one also considers the space charge induced broadening of the longitudinal bunch shape, this influence can be compensated by the η parameter too. For this purpose, η has to be negative as it is show on figure 2.9 compared to the normal trapping mode introduced previously.
If considering a Gaussian shape of the bunch in the longitudinal direction, ions in front of the maximum obtain the coulomb force of ions behind and get accelerated; ions on the opposite side get decelerated. Even if the ions keep their position in the bunch due to the equal frequency at $\eta = 0$, they will be accelerated further. Assuming a negative η, the faster ions will be pushed in the direction of the bunch maximum, and furthermore due to their unchanged energy, they will reach the low-energy side of the bunch. At this side, the coulomb repulsion is now able to decelerate the energetic ions, and they will be shifted again towards the bunch maximum because of their changed energy.
Depending on the exact shape of the potential and the starting position of the ions in the bunch, the ions will oscillate with different amplitudes around the bunch maximum. Here, it is possible to retain the bunch.

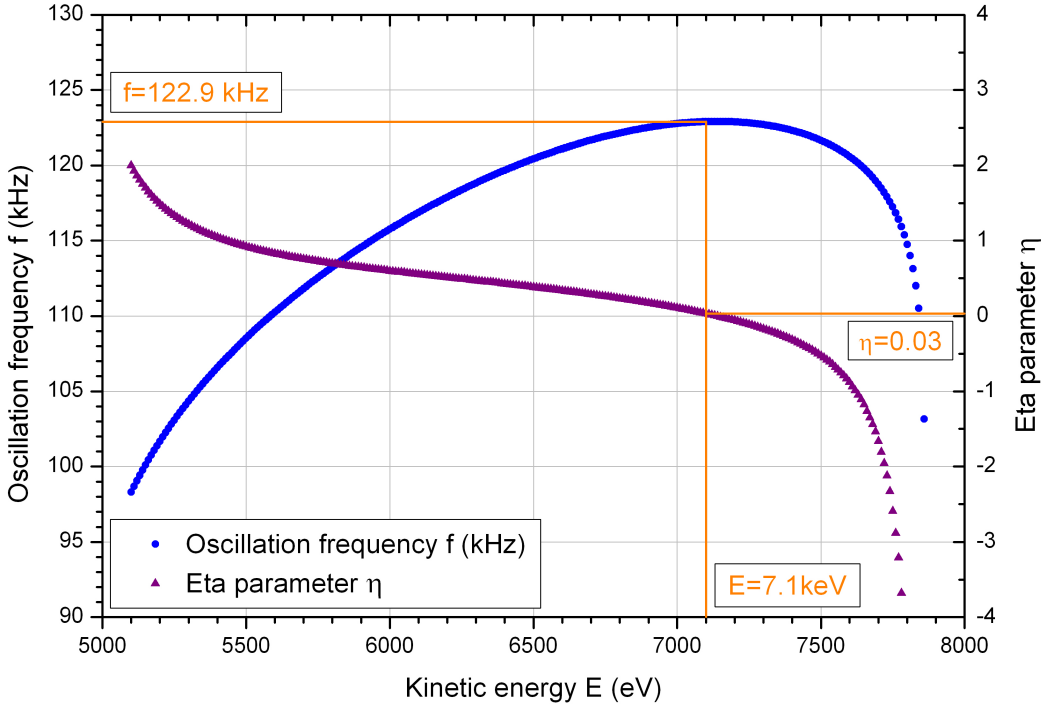

Figure 2.8: *Oscillation frequency and η parameter for the optimized electrode potential for an ion energy of 7.1 keV*

The latter phenomenon is the so called 'self-bunching' where a bunch is automatically formed out of a homogeneous filled trap. Small fluctuations on the ion distribution rep-

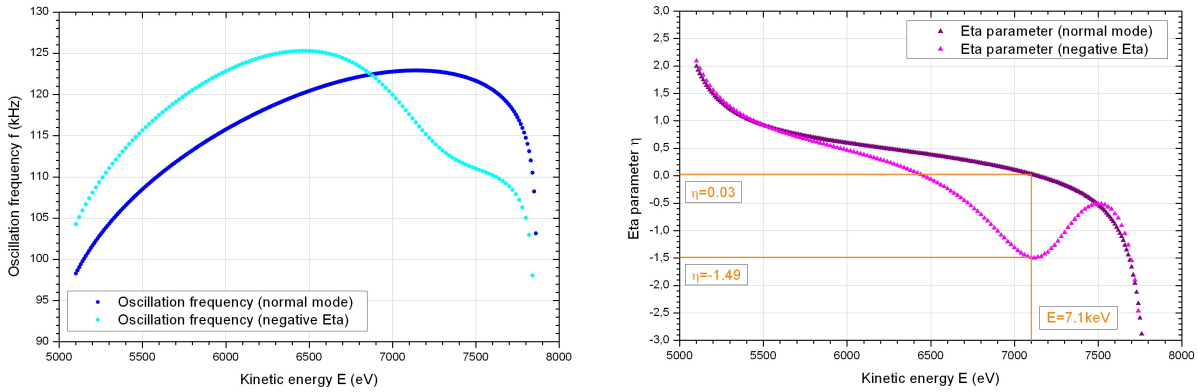

Figure 2.9: *Comparison of the oscillation frequency and η parameter for normal mode and the self-bunching mode of electrode potential for 7.1 keV*

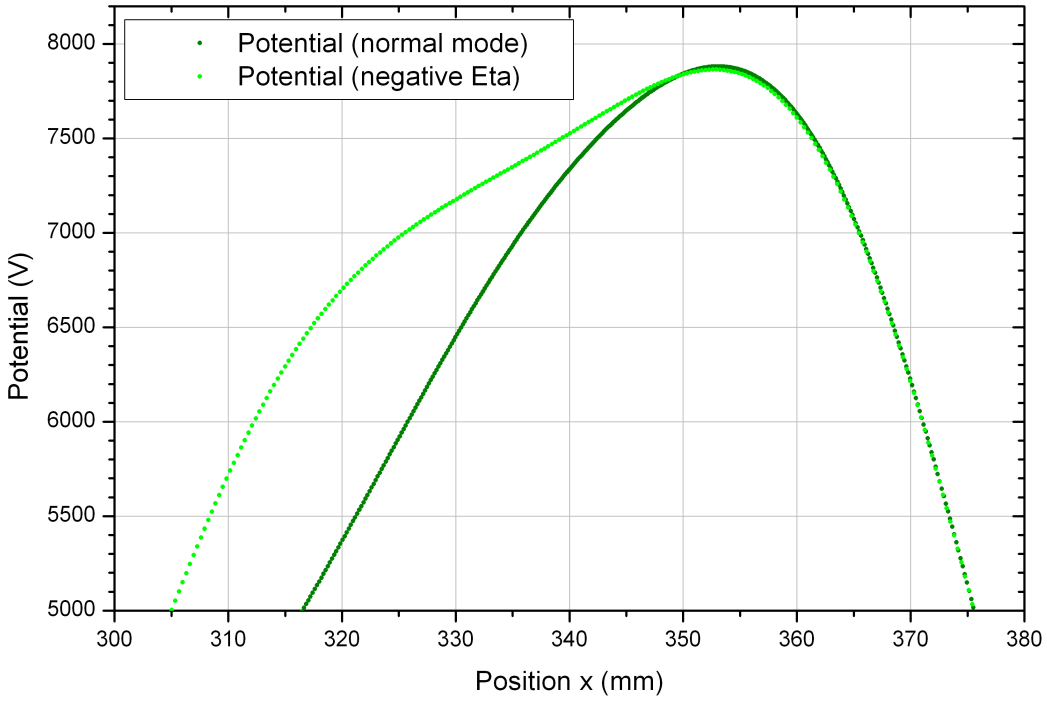

Figure 2.10: *The maximum of the bounding potential compared for the normal mode (dark green) and the self-bunching mode with negative η (light green)*

resent the provisional bunch and initiate this process. Once again, the bunch is pushed together by the potential and the space charge effect, so that more ions will be included in the bunch.

To realize a negative η parameter in the trap the value α_E has to be increased and hence, the slope $\delta\phi(\tilde{x}_0)/\delta x$ has to be reduced (compare eqn. 2.10 and 2.9). This can be provided by mainly varying electrode E and F which changes the slope of the potential at the point of return, and thereby leading to a modified dependency of the path length and oscillation frequency on the ion energy. The maximum of the bounding potential is shown in figure 2.10 (light green curve) in comparison with the normal potential shape.

2.3 Ion loss processes in a linear ion trap

The storage of ions in a linear ion trap is limited due to different types of loss processes. The electron capture process is only influenced by the pressure conditions in the trapping area, whereas single and multiple scattering are also dependent on the finite volume of stable trapping, the trap acceptance. Additional loss processes are possible which are independent of the vacuum, like ion-ion scattering induced broadening of the ion distribution out of the trap acceptance or external perturbations caused by fluctuations on the electrode voltages.
Important for the performed measurements is primarily the relation between the storage lifetime and the trap pressure which gives the opportunity to estimate the vacuum conditions by storing ions and counting the neutralized particles from the electron capture process.
Considering an exponential decay of the trapped ions, the time dependent number of ions in the trap N and the corresponding loss rate dN/dt, respectively, are given by

$$N(t) = N_0\, e^{-\frac{t}{\tau}}\,, \tag{2.13}$$

$$(\frac{dN}{dt}) = -\frac{N_0}{\tau}\, e^{-\frac{t}{\tau}}\,, \tag{2.14}$$

where N_0 is the initial ion quantity and τ the lifetime.
If several exponential loss processes are involved, the different individual lifetimes have to be summed reciprocally. The total loss rate can then be written as the sum over the constituent:

$$\frac{1}{\tau_{total}} = \sum_i \frac{1}{\tau_i}\,, \tag{2.15}$$

$$(\frac{dN}{dt})_{total} = \sum_i (\frac{dN}{dt})_i = -N_0 \sum_i \frac{1}{\tau_i}\, e^{-\frac{t}{\tau}}\,. \tag{2.16}$$

Whether due to a neutralization or a scattering process, the lifetime is linear dependent on the inverse residual gas density:

$$\tau \propto \frac{1}{n}\,. \tag{2.17}$$

Using the ideal gas law, the residual gas density is linear dependent on the pressure for a given temperature: $n = p/k_B T$. For the temperature in Kelvin and the pressure in millibar the restgas density is given by

$$n\,(m^{-3}) \;=\; 7.246 \cdot 10^{24}\;\frac{p\,(mbar)}{T\,(K)}, \tag{2.18}$$

where n is in units of inverse cubic meters. For a pressure of 10^{-11} mbar and a room temperature of 300 K, for instance, the restgas density is approximately $2.4 \cdot 10^{11}$ particles per cubic meter.

The non-constant velocity distribution of ions in the trap and especially the very low energy at the point of return lead to difficulties in describing the process. If the cross section is independent of the velocity, an averaged value $\hat{v}$ over one revolution in the trap can be used. For the opposite case the velocity dependency has to be extracted out of the cross section and averaged afterwards.

However, the characterization of the loss process is a difficult task and can not be done with accurate precision.

2.3.1 Electron capture process

Electron capture is the neutralization of the stored ions through electron exchange with residual gas atoms or molecules. The neutralized ion will keep the initial speed but probably decay into fragments in the case of a molecular ion through the additional energy of the electron. However, for the lifetime estimation the loss rate does not have to be measured absolutely, so that only sufficient amount of neutral fragments need to hit the detector.

The residual gas consists almost exclusively of hydrogen, as in cryogenic conditions other gases like nitrogen, oxygen or argon, for instance, are frozen out on the cold chamber walls. But also for room temperature measurements, it is mainly hydrogen as the turbo and ion getter pumps as well as the cryo pump are effectively pumping most of the other gases.

Some experimental determined cross sections of the electron capture process are shown in figure 2.11. The cross sections are given for N_2^+ in H_2 and N_2 as a function of the ion beam energy which is in the range of the energy distribution in the trap. For the low energy region the cross section has a slight difference between H_2 and N_2 and also a small discrepancy to the high energy is visible. Considering the small range of the displayed data, the values are only changing by at most a factor of two and will be considered to be constant for this energy range.

With the assumption of an energy-independent cross section the lifetime can be written as

$$\tau_{Capture} = \frac{1}{n\,\sigma\,\bar{v}}\,, \tag{2.19}$$

where n is the residual gas density, σ the energy independent cross section and $\bar{v}$ the average ion velocity.

Assuming the optimized trap potential, the average absolute velocity and the average energy, respectively, for a single charged molecular nitrogen N_2^+ with 7.1 keV ion energy are given by

$$\bar{v} = 167.7 \pm 1.4\,\frac{mm}{\mu s} \tag{2.20}$$

$$\bar{E} = 4543 \pm 55\,eV\,, \tag{2.21}$$

with the maximum values of $v_{max} = 221.2$ mm/s and $E_{max} = 7100$ eV.

Using the mean energy value, the residual gas density for a pressure of 10^{-11} mbar and an average cross section of $28 \cdot 10^{-20}$ m^2 results in a lifetime due to electron capture of approximately 88 seconds.

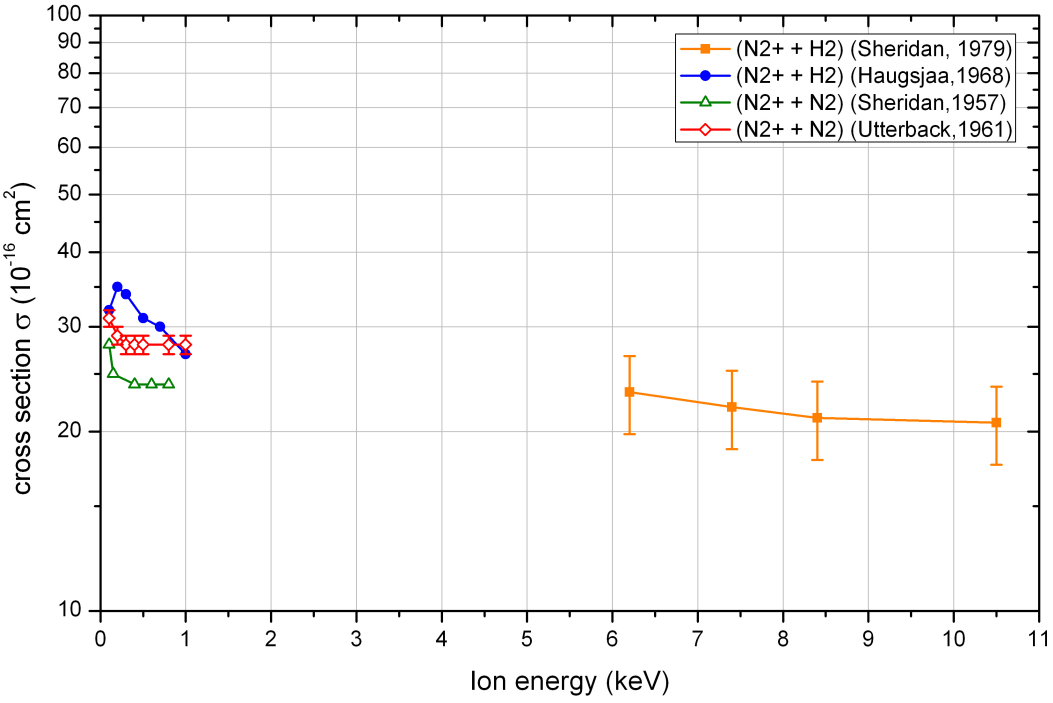

Figure 2.11: *Measured electron capture cross sections for N_2^+ in H_2 and N_2, respectively, as a function of the ion beam energy ([17], [18], [19] and [20])*

2.3.2 Single and multiple scattering processes

In these processes, the ions leave the trap due to a scattering process with residual gas particles which directs them out of the stable region of the trapping area. As mentioned before, the stable region is called the trap acceptance and is defined by

$$A = \pi\, y_{max}\, y'_{max}\,, \tag{2.22}$$

where y_{max} and y'_{max} are the maximal stable values of the transversal position and angle, respectively. The acceptance for the trap center can be determined with the help of the phase space shown in figure 2.5. Possible trajectories are given up to $y = 5$ mm and $y' = 15$ mrad but the region of a linear ion movement without resonances is $y_{max} = 3$ mm and $y'_{max} = 8$ mrad. However, exact values are difficult to define as the phase space and the acceptance values depend on trap positions.
Assuming a Rutherford scattering cross section, it is well known that the energy dependencies are proportional to $1/E^2$ and not negligible in this case. If one uses the equation 2.19 and extracts the energy dependency out of the cross section, the result for the lifetime dependency on the energy and velocity would be

$$\tau_{Multiple\,scattering} \propto E^{3/2} \propto v^3\,. \tag{2.23}$$

For the angular dependency, one has to integrate over the differential cross section using the angular acceptance. Considering again the Rutherford scattering cross section, the scattering probability for larger angles descends rapidly. The characterization of the trap lifetime by only using this angular scattering dependency would be the single scattering process.
As the probability for large angle scattering strongly decreases, the multiple scattering process becomes much more likely. Here a stochastic scattering process of many small angles leads finally to the ion loss out of the trap acceptance. However, the characterization of this processes is very difficult, particularly as the trap acceptance changes during the propagation of the ions in the potential and also the ion energy vanishes at the point of return.
A good description of this loss process for protons in a storage ring has been developed by W. Hardt [21] in a formula for a round vacuum chamber. In this case the important dependencies of the storage lifetime are given by

$$\tau_M \propto \frac{A\, v^3}{p}\,, \tag{2.24}$$

where A is the acceptance, v the velocity and p the pressure in the vacuum chamber.

2.3.3 Pressure-independent loss processes

The two pressure independent loss processes that could occur in the trap are the intrabeam scattering and a trap specific loss of ions due to fluctuations on the electrode voltages. For both processes no theoretical formulation will be given in this work but rather a short characterization of the processes.
In the first mentioned process, the intrabeam scattering, the ions are scattering off each other, thereby their distribution in the trap becomes broader and similar to multiple scattering, the ions leave the acceptance. So the first point is that this process also leads to an increasing lifetime with the size of the acceptance.
Additionally, the ion density in the trap plays an important role as this defines the mean distance of the ions to each other and the corresponding strength of the coulomb repulsion. Especially at the point of return the density increases as the ions are focused into the reflection potential by electrode B (compare for example trajectory 2.4 (a)). So particularly at this position the intrabeam scattering could become significant.
Furthermore, due to their small velocity, the ions spend more time at the returning point and so the gained deflection momentum by coulomb repulsion becomes rather large compared to their initial momentum.
For a lifetime measurement using different injection energies, the expected lifetime curve should increase with the energy. More energy leads to a weaker influence by the deflection force. On the other side, it has to be also taken into account that with faster velocity, the ions more often pass the point of return within a comparable time scale. However, this process describes a non-exponential decay, and it should be visible in the observed lifetime curves.

The second process, involving voltage fluctuations on the electrodes, has not been proven yet but the measured noise of the voltage could lead to a loss of ions. These fluctuation are produced by the high-voltage switches, so they only influence one side of the trap.
One fluctuation has been determined to have mainly a sinus like shape of one period with an approximated length of 400 ns. Thereby, the intensity is independent on the applied voltage and at most 40 volts peak to peak. Furthermore, these periodic fluctuation occurs roughly each 300 ms.
The mentioned voltage changes are not high enough to generate an exit for the ions at

the borders of the potential, but they could accelerate them to the limiting energy. Furthermore, ions could be kicked out of the trap acceptance.
However, as the intensity of the fluctuations are independent on the applied voltage, ions with higher energy will gain a lower deflection angle and smaller acceleration force compared to their momentum. So the corresponding lifetime would increase with the ion energy. Additionally, as the duration and occurrence of the fluctuations are constant, the loss rate will be proportional to the number of currently trapped ions, and accordingly, this loss process will lead to an exponential decay.
Summarizing the entire loss processes, the total lifetime τ is defined by

$$\frac{1}{\tau} = \frac{1}{\tau_C} + \frac{1}{\tau_M} + \frac{1}{\tau_I} + \frac{1}{\tau_T}, \tag{2.25}$$

where τ_C is the electron capture process, τ_M the multiple scattering, τ_I the intrabeam scattering and finally τ_T the trap voltage fluctuations.

2.3.4 Measurable loss process

Because the employed detector can only be reached by neutral particles, the accessible quantity in (2.16) is the partial loss rate due to the electron capture process. By fitting an exponential decay curve on the measured count rate, the two obtained values are the amplitude A_C and the total lifetime τ. The total number of neutral fragments counted by the detector per injection is then given by

$$N_C = A_C \tau . \tag{2.26}$$

The complete number of neutrals escaping out of the trap N_0^C is proportional to this value, if the efficiency ϵ of the detection stays constant:

$$N_C = 1/2 \, \epsilon \, N_0^C = 1/2 \, \epsilon \, N_0 \frac{\tau}{\tau_C} . \tag{2.27}$$

The efficiency ϵ is dependent on, for instance, the angular acceptance and the counting efficiency of the detector. The factor $1/2$ occurs because the detection takes place only on the exit side of the trap and half of the neutrals are leaving the trap in entrance direction. The detection efficiency in ϵ is approximately 60 % for a MCP hit by keV atoms or molecules. However, a lot of neutral particles may be much slower depending on where in the trap the neutralization reaction occurs.

3. The design and experimental setup of the CTF

The Cryogenic Trap for Fast ion beams (CTF) consists of a linear ion trap described in the previous chapter housed in a cryogenic beam pipe. The trap is used as a 'Cryogenic Test Facility' and in accordance with this acronym it is first of all operating as a test device for the cryogenic concept of the Cryogenic Storage Ring (CSR). The primary goals are to test the cryogenic cooling technique via a closed-circuit superfluid helium refrigeration system, perform experiments with different materials for thermal connections or decoupling and not the least also the verification of the extremely low pressure conditions in the inner vacuum system. One important task is also to answer the question whether the option of baking the inner vacuum system of the CSR is necessary. Therefore, the CTF is equipped with a baking system in order to explore the differences in the pressure at cold conditions for a baked and non-baked system. This chapter will show the construction of the CTF, the analogy to the CSR and some modifications in the concept of the CSR by experiences during construction and operation of the CTF.

3.1 Mechanical and cryogenic design

To reach the low temperatures of a few Kelvin in the experimental area, the isolation to the outside at room temperature has to prevent all types of energy coming into the inner system. To provide sufficient insulation an outer isolation vacuum system surrounding the inner experimental vacuum chamber of the trapping area is necessary. Using this concept the heat convection from the borders of the isolation vacuum to the inner chamber is reduced. This and other concepts of the cooling and thermal insulation are presented here.

Figure 3.1: *Overview of the CTF with the ion source and injection line on the left and a part of the helium refrigeration system in the background*

3.1.1 Cryogenic trapping area and trap design

The basic idea of the design is to achieve the lowest temperatures around the trapping area on the inside of the inner vacuum chamber. Therefore, the trap is positioned in the center of the whole device and has the best thermal connections to the cooling system. As shown in the side view of the CTF on figure 3.2 the two yellow marked stacks of electrodes are defining the trapping area in the center. The ions are injected through the left side of the beam pipe into the trap. The distance of the outermost electrodes is nearly 80 centimeters. The isolation vacuum chamber has a length of roughly three meters and a volume of three cubic meters.

The inner vacuum chamber electrode stacks have to be cooled to the low temperature too. To accomplish that, the stacks are thermally connected to the cold vacuum chamber by sapphire, which is a good electrical insulator and conducts heat well. Additionally, the electrodes are cooled via the high voltage connections.

As illustrated in figure 3.3 a cage is surrounding the electrodes and thereby holding them in position. As well as the electrodes it is made out of aluminum with a thin gold

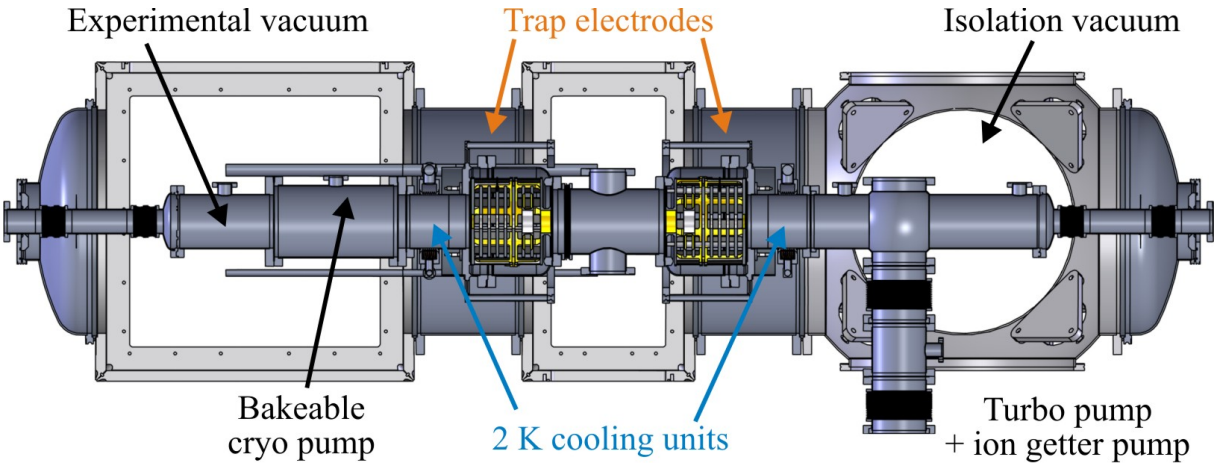

Figure 3.2: *Schematic side view of the CTF: The cold experimental vacuum chamber including the two trap electrode stacks (yellow) and the bakeable cryo pump surrounded by the isolation vacuum chamber (Radiation shields are not shown). The 2K cooling units are located behind each electrode stack.*

layer on top. The cage has a good thermal connection to the inside of the cold vacuum chamber and the constantly grounded electrodes are automatically cooled through the fact that they are a part of this cage itself. The other electrodes are linked to the cage by sapphire spacers (see fig. 3.4) which get pressed more and more together during the shrinking processes of the cage when the device is cooled down. This effect leads to a better thermal contact at cold temperatures and a more effective cooling.
The shrinking effect is also used for the second cooling method of the electrodes. The high voltage wires for the electrodes are cooled with four sticks of sapphire forming a cross (fig. 3.5). The wire is fed through the middle of the cross and during the shrinking of the outer circular aluminum frame the sapphire sticks get pressed onto the wire. From the feed-through on the outer chamber to the inner, each of the high voltage wires traverses two of these sapphire crosses thermally connected to the cold chamber and the 40 K radiation shields which are discussed later.

As mentioned before, the inner cold vacuum system is separated from room temperature by an isolation vacuum system. To prevent the thermal flux from outside the cold chamber has to be mounted in a very well isolated way but also sufficiently stable to hold the weight of the chamber. Therefore, the construction of a heat flow reducing wire suspension had been developed (Fig. 3.6). The idea is to fix all parts of the cold chamber by thin stainless steel wires on the inside of the isolation chamber. The total weight of the chamber is distributed over a large amount of wires as described below.

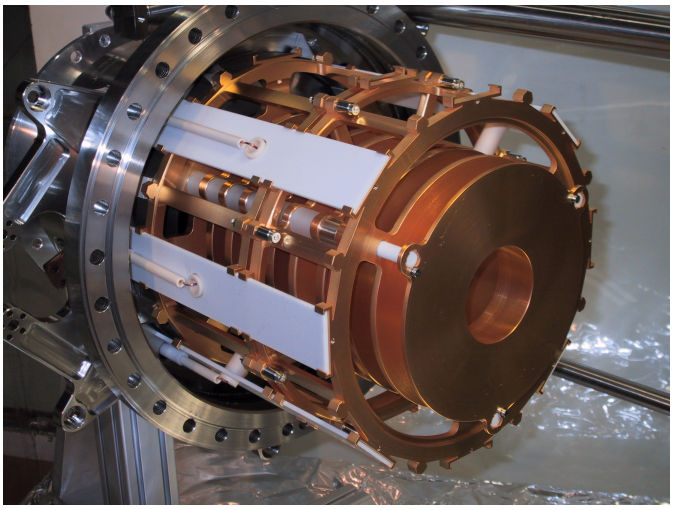

Figure 3.3: *Electrode stack connected a part of the vacuum chamber. The white ceramic plates isolate the high-voltage wires from the grounded cage. Electrode A is shown in the front (compare fig. 2.2).*

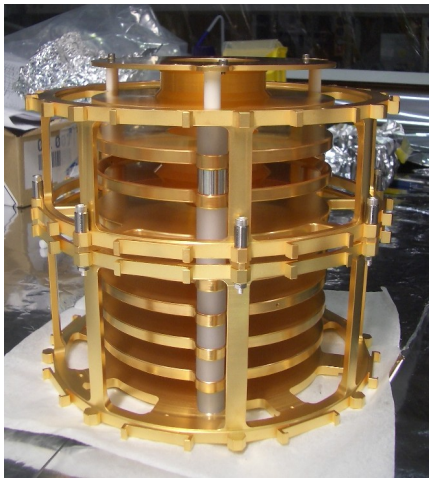

Figure 3.4: *One electrode stack surrounded by the grounded cage. The electrode plates are electrically isolated by sapphire spacers and hence, cooled by the good thermal contact*

These suspension wires are also used for the alignment of the two separated stacks of electrodes. Each of the trap parts is positioned inside of a vacuum chamber and connected with each other by a third chamber in between. This middle chamber has a small bellow at one side and thus, the two trap parts can be aligned separately towards the

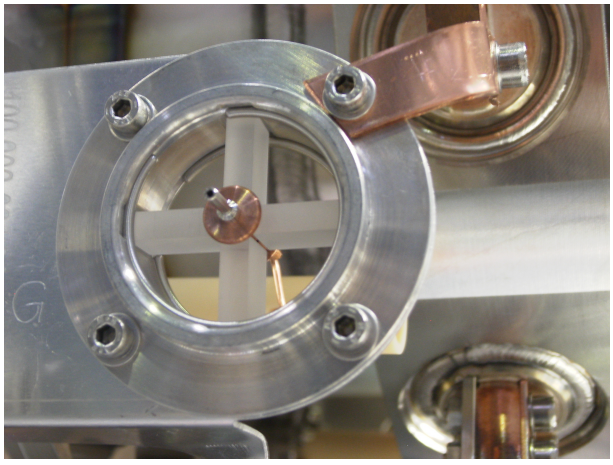

Figure 3.5: *Sapphire cross to cool the high-voltage wire to the electrodes. Due to the shrinking of the aluminum ring at cryogenic temperatures, the sapphire sticks are pressed on the wire.*

center of the beam line and to each other. Therefore, the wires are not only on the top of the chamber but also on the sides. In particular they are spanned more diagonally in the isolation chamber, for instance, from the one side at the top of one chamber diagonal down in direction of the other one. Hence, it is also possible to rotate the chamber by a small amount.
As there are only six degrees of freedom per electrode chamber, the usage of twelve suspension wires is obviously a disadvantage for the alignment. But the idea of this symmetric suspension system was the important point of keeping the alignment at the cold temperatures. For a sufficient alignment of the two trap parts, a precision of 0.1 mm has to be achieved. Here, it is important to note that the temperature difference between room temperature and 2 Kelvin leads to a shrinking process for stainless steel of 0.3 %. Hence, the length of the suspension wires would be reduced by approximately a factor of 30 higher amount as the required precision and this effect has to be compensated by the symmetric suspension system.
For the CSR a new support method has been developed because in addition to the complicated alignment, the electrostatic deflectors in the ring corners need an asymmetric wire suspension which would not keep the alignment during the cooling process. In the new concept, the ion optical deflectors as well as the ion diagnostics are standing on support bases at room temperature instead of hanging on wires and hence, they are decoupled from the cold chamber, shields and isolation vacuum chamber. The isolation is realized by the special structure consisting of different layers which are thermally anchored at the shields and cold chamber. All the types of deflectors, beam optics and diagnostics can be aligned at room temperature and during the cool-down process their position with respect to each other can not change due to temperature gradients. The shrinking process of the support bases itself will only change the height of the optics and not the alignment and thus, the beam will just be in a slightly lower level.

3.1.2 Cryogenic techniques and thermal shielding

The cold chamber

As already mentioned in previous sections the whole device is cooled to cryogenic temperature of a few Kelvin by a closed-circuit refrigeration system employing superfluid helium in the coldest stage. Actually, there are two separated closed circuits of helium pipes inside of the CTF. One of them is cooling the experimental chamber exclusively whereas

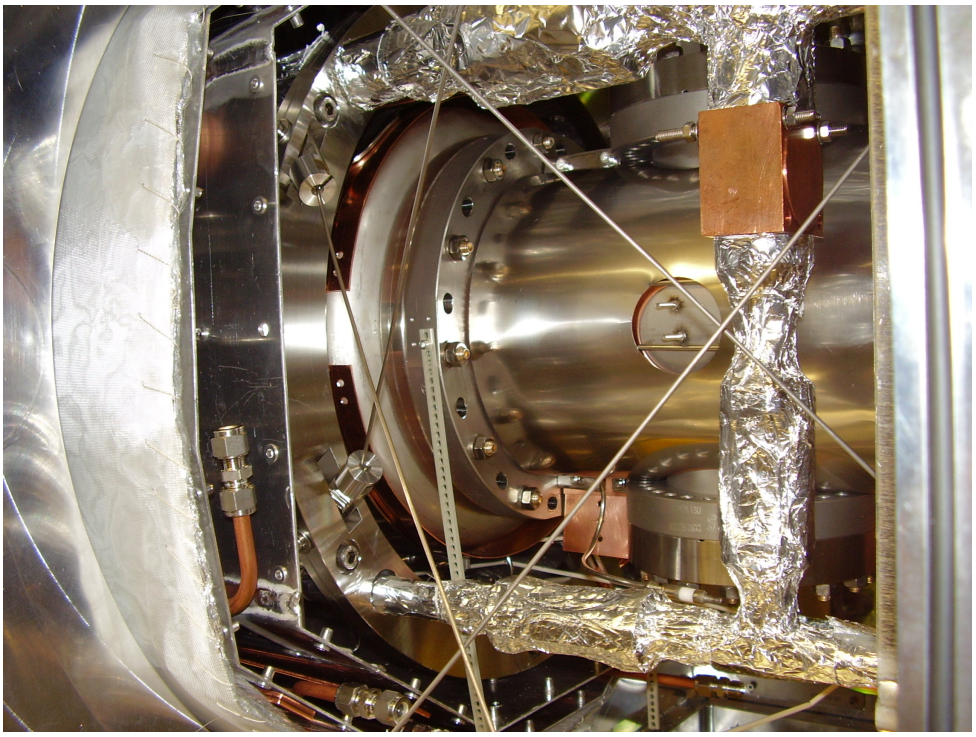

Figure 3.6: *The CTF middle chamber between the two stack electrodes (compare fig. 3.2). On the left are the 40K and 80K radiation shields shown as well as the multi-layer insulation. In addition, 2K pipes for the superfluid helium wrapped in multi-layer insulation are shown and some of the stainless steel wires for chamber suspension.*

the other one is conducting the heat from the isolation shields which will be introduced afterwards. The only connection technique used between all pieces of the pipe systems is to weld them. On several positions bellows are included in the pipes to account for the stress of the shrinking material during cool-down.

The experimental vacuum chamber is cooled by a helium pipe system at a temperature of 2 Kelvin and at a pressure of 18 mbar in cold operation, which means that the helium is in a superfluid state inside the CTF. This pipe system consists of two parallel pipes on top of each other with connections at several positions. The superfluid helium is guided through the lower pipe and stands in it and in the perpendicular connections. As the upper pipe has a larger diameter it is used to pump the evaporating helium from the surface area back to the refrigeration system. Thereby, the heat transfer is effected while the superfluid helium keeps its temperature.

The perpendicular connections between the two pipes are linked to parts on the cold chamber to cool it. The positions of importance are the two cooling units where the

perpendicular connection is forming a ring and the superfluid helium is standing directly around the experimental beam pipe (see fig. 3.7). These cooling units are positioned behind the electrode chamber on both sides (see fig. 3.2).
In addition to this direct contact of the chamber walls with the helium there are also some copper blocks in direct contact with the superfluid helium which are used to conduct the heat from other parts of the chamber via additional strips attached to this block. Also near the middle chamber between the two electrodes a perpendicular connection of the helium pipes is made where a copper block (Fig. 3.6) gives the opportunity to connect several parts of the chamber. For all the connecting strips high-purity copper of 99.997 % was used which has a much higher thermal conductivity than normal copper at low temperatures.
To control the level of the superfluid helium inside the CTF a helium level sensor was installed at one of the vertical connection pipes. The sensor consists of a long stick made out of a superconducting material which stands in the superfluid helium. By measuring the resistance of the stick one can calculate the height of the level and keep it constant by a regulation loop.

Isolation shields

The basic requirement in cryogenic devices is to keep the heat input into your system lower than the cooling power provided by the refrigeration system. Here different types of heat input have to be taken into account like the thermal radiation coming from the isolation vacuum chamber, the convection heat through air, the heat conduction of the suspension system of the cold chamber. As shown schematically in figure 3.7 the CTF consists of different types of layers which all prevent the heat input from room temperature.
The blackbody radiation of 300 K room temperature is prevented by 15-20 layers of multi-layer insulation, depending on available space and the two types of helium cooled radiation shields. At first, the cold inner vacuum chamber is surrounded by the 40 Kelvin radiation shields and around them are the 80 Kelvin shields. They are both connected to the second system of helium pipes. The helium enters the system at an initial temperature of 5 Kelvin and thus, is permanently in a gaseous phase. During the first loop in the isolation vacuum chamber the helium pipes are positioned inside the 40 Kelvin shields and thereby, linked to them by copper strips. The helium heats up to approximately 40 Kelvin and the shields reach a temperature below that. Afterwards the helium pipes are guided between the two shield systems and connected to the 80 Kelvin shields. The 80

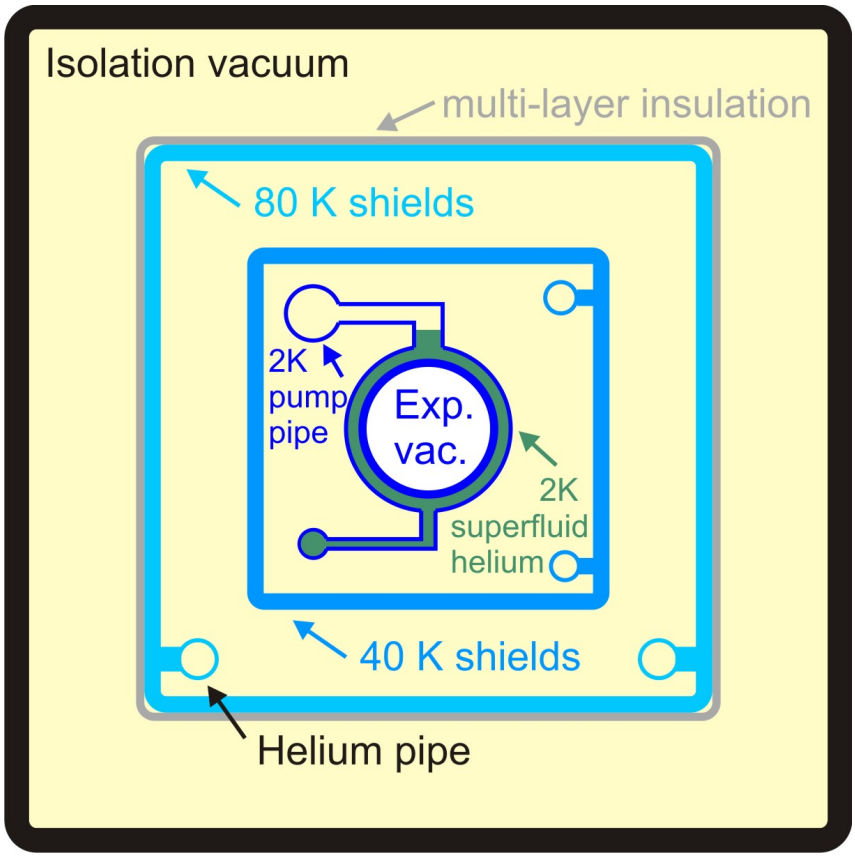

Figure 3.7: *Schematic view of the CTF cross section showing the cooling pipes and the isolation shielding*

Kelvin helium is then pumped back to the refrigeration system and gets cooled again.
The special multi-layer insulation consists of a thin aluminum foil and a layer of glass fibers manufactured by austrian aerospace. Using all the layers the radiation is reduced by approximately 95 %. By this reduced radiation the two shields keep their temperature and the cold chamber just gets a heat input of 40 Kelvin blackbody radiation.
The heat input by convection heat is decreased by the isolation vacuum. The pressure is in the order of 10^{-5} mbar at warm conditions and even 10^{-7} to 10^{-8} mbar when the device is cooled down. Cold surfaces like the shields help to achieve this low pressure by pumping, for instance, nitrogen or oxygen. In addition, two molecular sieves are used to improve the isolation vacuum. These sieves are made out of a granular material with tiny pores which is used as an adsorbent for gases. They are attached to over 30 cm of the 5 Kelvin pipe and cooled in this way.
The last heat input is the thermal flux through the suspension system of the cold chamber. This is reduced by using thin stainless steel wires that hold the chambers in their

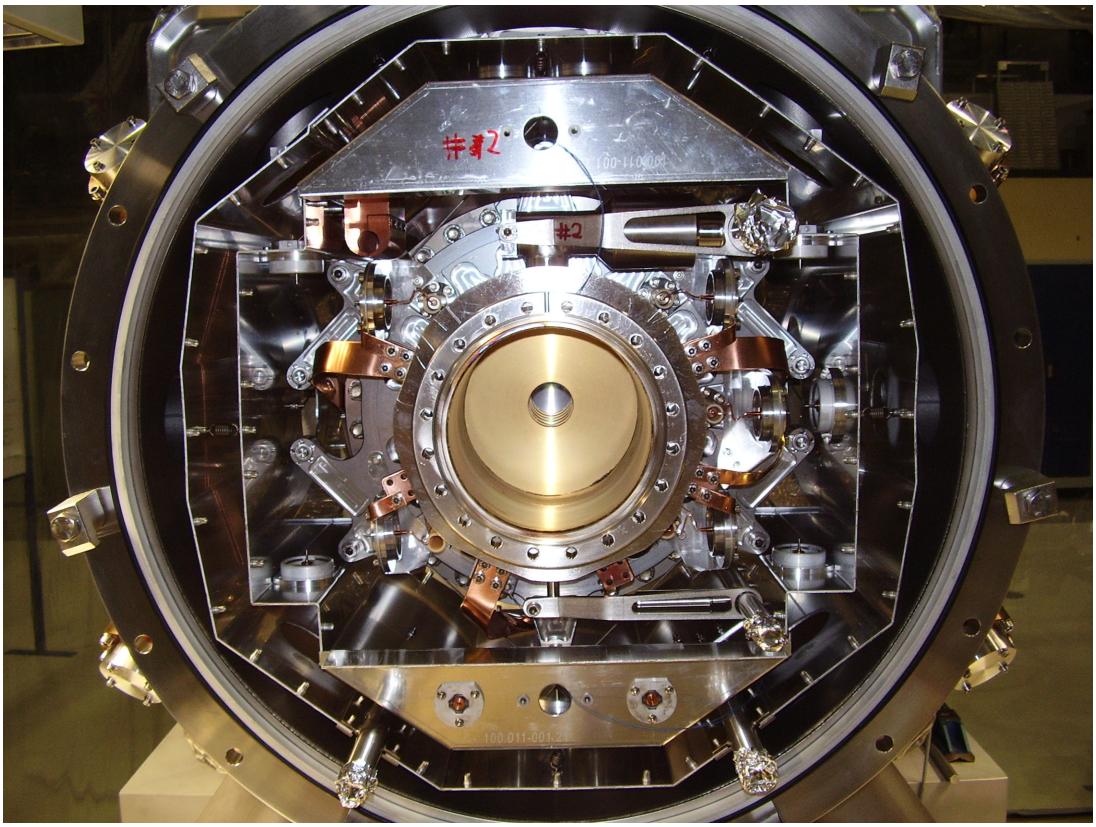

Figure 3.8: *CTF cross section showing the trap electrodes inside the inner vacuum chamber which is surrounded by the cooling unit (left side in fig. 3.2). Copper connections from the cooling unit are connected to the high-voltage feed-throughs.*

position. The wires are also not closely connected to the chamber rather hanging with their ends in a holder. Therefore, a small ball of stainless steel is welded on each end of a wire which reduces the thermal contact. Furthermore, the thermal flux from the beam entrance, exit and the pump stand below of the beam pipe is decreased by bellows (Shown an fig. 3.2). The pipes between the two bellows on each position are connected to the 40 Kelvin shield to reach a stepwise cooling from the warm to the cold regions.
As shown in the picture 3.6 the helium pipes are wrapped in 20 layers of multi-layer insulation which are needed due to safety reasons. In case of an accidental breaking of the isolation vacuum the heat transfer through convection will heat up the cold helium inside the pipes very quickly. The expansion of the helium can break the bellows or the weldings of the pipes. Hence, the multi-layer insulation of the pipes would reduce the heat input and warm up the helium much slower.

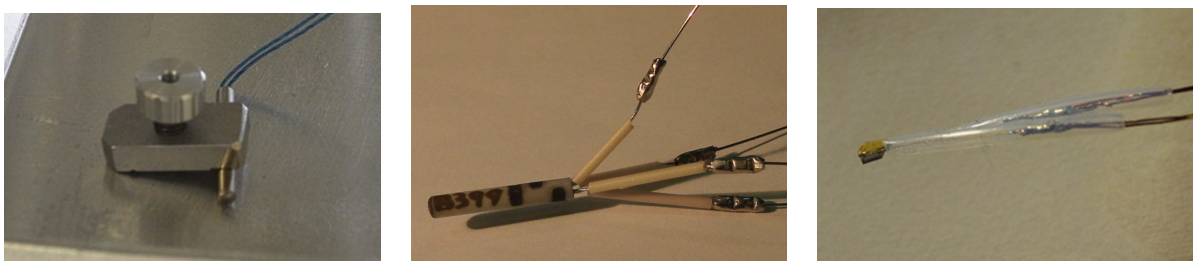

(a) Platinum sensor PT1000 (b) Rhodium iron sensor (c) Silicon diode sensor

Figure 3.9: *The three different temperature sensors which have been used in the CTF*

Temperature sensors

Three types of temperature sensors are in use in the CTF to measure the characteristic cool down curves, the temperatures at cold conditions and also to control the baking procedure. All the different properties of the sensor types are necessary for these various uses.

Figure 3.9 shows the temperature sensors beginning with the Platinum sensor (a), the rhodium iron sensor (b) and the silicon diode sensor (c). The Platinum sensors of type PT1000 are used at many positions in the CTF with a quantity of nearly 50. They are mainly connected to the radiation shields and at some positions on the helium pipes and the cold chamber. As their reliable temperature reaches from nearly 900 Kelvin down to 30 Kelvin they are used to control the cooling process and also the bake-out. For both processes it is important to keep the temperature gradients small especially across flanges of the cold chamber. The refrigeration system uses one of these temperature sensors to control the cooling process and thereby moderate it. To control the baking of the inner vacuum system the platinum sensors on the cold chamber are used.

To measure the final low temperatures on the cold chamber the two remaining sensor types are installed which give more sensitive temperature measurements. The rhodium iron sensor (RhFe) has a temperature range from 0.65 to 500 Kelvin whereas the silicon diodes reach from 1.4 to 500 Kelvin. The RhFe sensors have the advantage of being resistant against the high temperatures of up to 620 Kelvin during baking. They are used at positions which are hard to access after the final assembly. The silicon sensors will probably not work any more after this hot temperature or at least, they will not reach their previous precision. For this reason the silicon diodes have to be removed from their positions on the cold chamber for the baking and reinstalled afterwards. The disadvantages of the RhFe sensors is on the other hand their worse thermal contact to

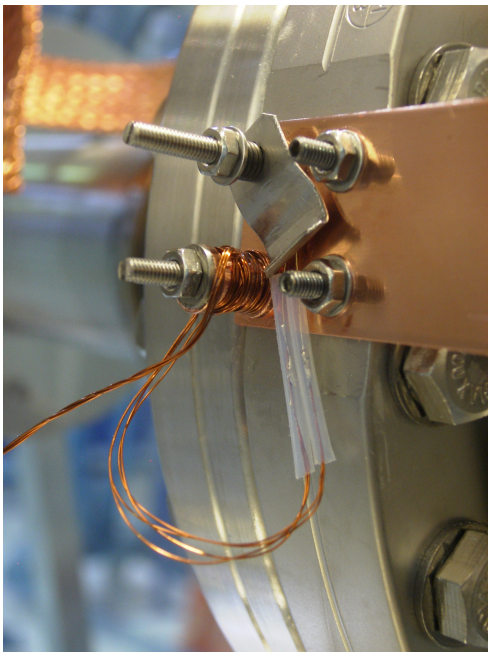

Figure 3.10: *The silicon sensor is clipped behind a small stainless steel plate. The readout wires are thermal anchored on a copper spool at the measuring temperature. Thermal grease was used on the sensor and wires to improve the thermal contact.*

other surfaces due to the encapsulation in ceramic and the more expensive cost.
To reach a precise measurement and due to the fact that the sensor wires have to be very long, a 4-Lead resistance measurement is used for the RhFe and silicon sensors. Additionally one has to make sure that the sensor wires are well cooled. Therefore, they are thermally anchored on a copper spool at the measuring temperature by wrapping the wires around it (figure 3.10). Furthermore the silicon sensors and the wires are attached using thermal grease to improve the thermal contact to the surfaces, which is not possible for those sensors which remain in place during baking. A better accuracy is also accomplished by using individual calibration tables for each of the silicon sensors.

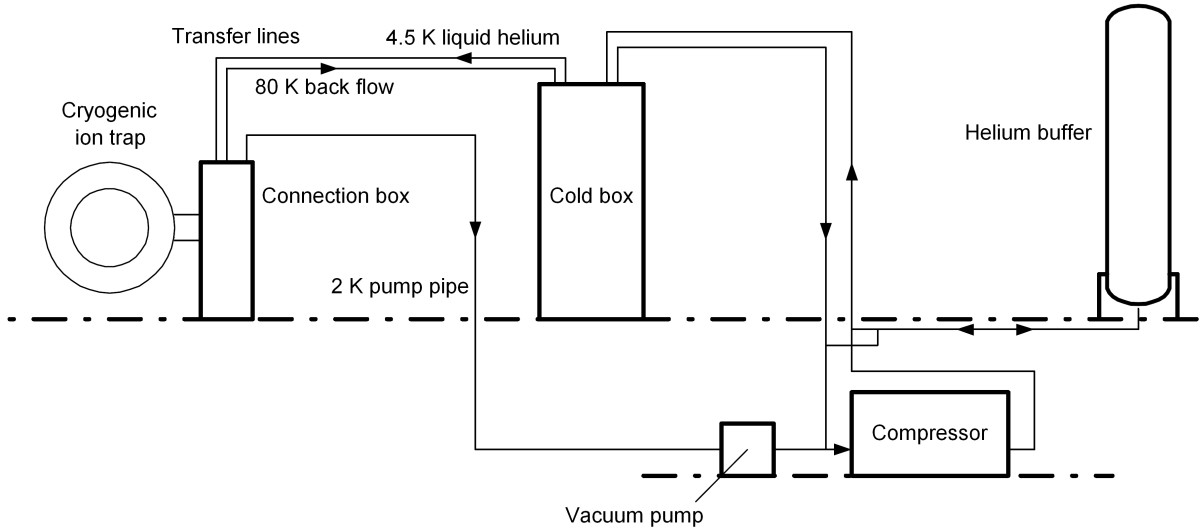

Figure 3.11: *Schematic layout of the cryogenic refrigeration system: The cryogenic ion trap CTF is shown on the left and linked to the connection box. Here, the 2K superfluid helium is produced, after it has been liquefied in the cold box to 4.5K and transferred from the connection box. The vacuum pump, the compressor and the helium buffer are located outside the building.*

Refrigeration system

A complex cryogenic refrigeration system provides the necessary cooling power for the CTF and later for the CSR as well. The system is equipped with two closed helium circuits which are permanently connected to the cryogenic ion trap. During the cooling process a short cut between the two closed circuits is used to generate a homogenous cool-down. A schematic layout of the whole refrigeration system is shown on the figure 3.11. The cryogenic device is shown on the left and linked to the connection box. Here the liquefaction for the 2 Kelvin helium circuit is accomplished, after the pre-cooled helium has been transfered from the cold box. The vacuum pump, the compressor and the helium buffer are positioned outside the building.

The first step in this cycle is the cooling of helium to a temperature near the inversion point. As this temperature at normal conditions is 4.2 Kelvin the helium is cooled in the cold box to approximately 5 Kelvin. A Brayton cooling process is used where the helium gets initially compressed isothermally by transferring the heat to an oil mixture, cooled via performing work on turbines by an isentropic expansion and guided back to the compressor. During the cooling process, the compressed helium gets further pre-cooled

Figure 3.12: *The connection box of the refrigeration system is shown and the cold box is located behind. The red and white striped area on the right is the position where the CTF was connected later.*

in a counter-flow heat exchanger by the cold back streaming helium coming from the turbines and thus, the expansion leads to a iteratively colder helium.
Accordingly, the compressed helium flow will be split up into two different cycles where one of them is still part of the Brayton process and the second is used to liquefy the helium by a Joule-Thompson expansion. This method uses a small thermally isolated nozzle called Joule-Thompson-valve to accomplish the expansion. As the nozzle performs no work the enthalpy stays constant. In case of an ideal gas no changes in the temperature are expected, since the enthalpy $H = U(T)+pV = U(T)+nkT$ has no pressure or volume dependence. In comparison, for a real gas represented by the Van-der-Waals equation a change in temperature appears. Whether a warming or cooling process occurs depends on the current pressure and temperature of the gas. Below the certain inversion values of the pressure and temperature which are usually near the condensation point cooling takes place.
In this case the Joule-Thompson expansion leads to the liquefaction and the helium con-

densates partially in a buffer with a temperature of 4.5 Kelvin. This liquid helium is transferred to the connection box where it is divided into the radiation shield pipe system and the 2 Kelvin cycle. Whereas the first helium stream is used to cool the shields without further changes, the second component is further refrigerated to a superfluid state at 2 Kelvin. This is accomplished by the expansion with a second Joule-Thompson-valve inside the connection box.
The superfluid helium then flows into the 2 Kelvin cycle of the CTF. The 2 Kelvin pump pipe coming from the CTF for the helium back flow is connected to the top of the superfluid helium reservoir in the connection box and thus, pumped back into the helium cycle.
The combination of the Brayton process and the liquefaction by Joule-Thomson expansion is called the Claude process.
The provided cooling power of the refrigeration system is 20 W in the 2 K cycle and 600 W at 80 K.

3.1.3 Vacuum pumping concept

For this vacuum concept a complex setup and many different types of vacuum pumps are required to reach an extremely low pressure in the central region of the cryogenic device, the trapping area itself. The complete setup with the focus on the vacuum system is illustrated on figure 3.13 and will be explained in more detail in this section. Starting with the ion source on the left the ion beam is guided through the beam cleaner towards the trapping area. The detection of the neutralized fragments coming out of the trap takes place on the right side. The experimental progress will be introduced in later sections and is not essential at this point. The common pressures distributed over the whole setup are also shown on the figure.

Vacuum system within the CTF

The experimental vacuum system in the CTF consists of stainless steel pipes connected by CF and COF flanges. The part inside the isolation vacuum chamber can be separated from the attached beam pipes by two hand valves positioned at the entrance and exit sides. To initially pump down the inner vacuum to 10^{-9} mbar, an oil-free piston pump and a turbomolecular pump at the fixed pump stand below the CTF are used. To accomplish lower pressures especially for room temperature operation the ion getter pump below the trap and the cryo pump in the inside are employed. Without previously baking the device a pressure of 10^{-9} mbar can be reached.
To measure those pressures two ion gauges positioned to the left and right of the trap are

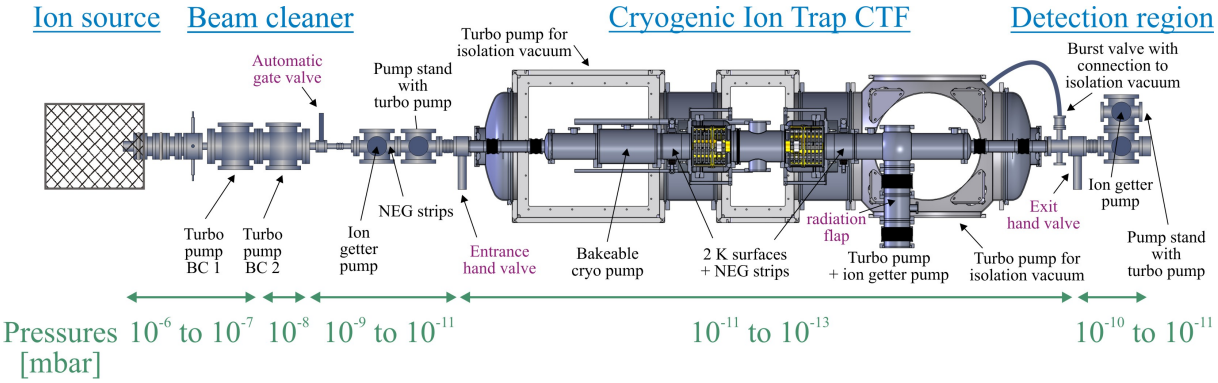

Figure 3.13: *CTF vacuum system including the ion source, injection line and detection region. Locations and types of the used vacuum pumps and valves are shown as well as the common pressures in the differentially pumped areas (Enlarged picture is given in the appendix).*

included. In addition, a third ion gauge is attached to the vacuum system below the CTF near the turbo pump. It is important to notice that the ion gauges in the inside can not be operated at cryogenic conditions. Two main reasons are responsible for this fact: On the one hand the hot cathodes of the ion gauges are producing too much of a heat load into the system which could not be handled by the refrigeration system. Also switching it on only for a short time will not lead to a precise measurement of the pressure, since the gauges have to be degassed for a certain time to make reliable approximations. On the other hand the thermal radiation and energetic particle flow coming from the cathode will desorb frozen gases from the cold chamber walls and thereby worsen the pressure locally. Due to that fact the measurements will influence the conditions in a non-negligible way. Also the expected low pressures of 10^{-13} mbar are not measurable with available gauges and therefore, the concept of estimating the pressure by storage lifetime measurements has been adopted.

To reduce the pressure further two other vacuum pumping methods are employed. On several positions on the inner chamber walls SAES ST707 NEG modules (Non-Evaporable-Getter) are installed which are thin metallic strips with a porous layer mainly consisting of zirconium powder. The residual gas ingredients are bound by chemical reactions with the surface material. Thus, also an effective pumping of the lighter restgases like hydrogen is possible, since other vacuum pumps are worse for those gases. To clean the reactive surfaces of the NEGs and thereby activate them, it is required to bake the vacuum chambers to at least 320 °C. During this process the already bound hydrogen is released from the NEG surfaces and can be pumped by turbo pumps or others. A diffusion process takes place in the NEG strips where the bound hydrogen is transported further into the material and thereby cleaning the surfaces. However, for this kind of pumping technique a baking equipment for the CTF has been included which will be introduced afterwards. At low temperatures the NEG strips lose their pumping properties and the pumping ability of the cold chamber gains in importance. As the final temperatures of about 10 K are fairly below the condensation points of many gases, nitrogen, oxygen or argon will adsorb on the cold surfaces. At the two ring-shaped cooling units even temperatures of 2 K are reached. These temperatures are necessary to reduce the vapor pressure of hydrogen leading to an effective pumping of this major remaining restgas. Baking the system and then cooling to 2 K would provide cleaner surfaces which are expected to increase the probability to adsorb restgas.

To reduce the heat load into the trapping area from the outside a radiation flap has been installed in the pump pipe to the turbo pump below. The operation is realized by sliding a hand gear from the outside and thereby rotating an aluminum plate that closes off the

pipe cross section. The opened position is used to better pump during warm temperature operation or baking. The flap does not generate a vacuum tight closure but the direct thermal radiation is prevented. And as the flap is connected to the 40 K shields only the blackbody radiation of this temperature gets access into the inside. Due to the worse thermal contact the flap will not reach 40 K but anyway the radiation is reduced.
Due to safety reasons a burst valve with a connection tube to the isolation vacuum has been installed. In case of sudden breaking of the inner vacuum system the burst valve will connect both vacuums at an over pressure of around 200 mbar in the inside. This is necessary to protect the bellows on the experimental chamber, since they can not resist a critical over pressure. The origin of this kind of vacuum breaking could be a sudden leak somewhere on the experimental chamber including the regions outside the trap. Moreover, the pressure rise could occur through abrupt desorption of frozen gases either from the cryo pump or the cold chamber walls itself caused by an accidentally shutdown of the cold head or the refrigeration system, respectively.

Differential pumping on the outside

Differential pumping units are necessary for this setup, since the complete vacuum system has a huge distribution of pressures, particularly due to the penning ion source. The vacuum system is separated into different sections by small tubes in the beam pipe. The pressure distribution is also shown on figure 3.13. On the left side, where the high-voltage enclosure with the penning source is positioned, the pressures are in the order of 10^{-6} to 10^{-7} mbar which is necessary for a stable source operation.
The next important differential pumping unit is the beam cleaner (fig. 3.14). The charged particle beam is guided by deflection plates through small pipes and hence, separate the vacuum chambers. The beam is thereby cleaned from neutral fragments coming from the source and only ions with the correct energy and charge state can pass. Besides this the beam cleaner is also used as a chopper to create small ion pulses for trapping. The two sides of the beam cleaner are pumped separately by turbo pumps below and thereby reach a pressure of approximately 10^{-8} mbar at the right side.
The following vacuum region contains an ion getter pump, a pump stand with a turbo pump and moreover a couple of NEG strips. If this section is properly baked pressures of up to 10^{-11} mbar can be reached, dependent on the state of the automatic valve to the beam cleaner and experimental usage.
In front of the entrance hand valve and after the exit valve to the CTF differential pump-

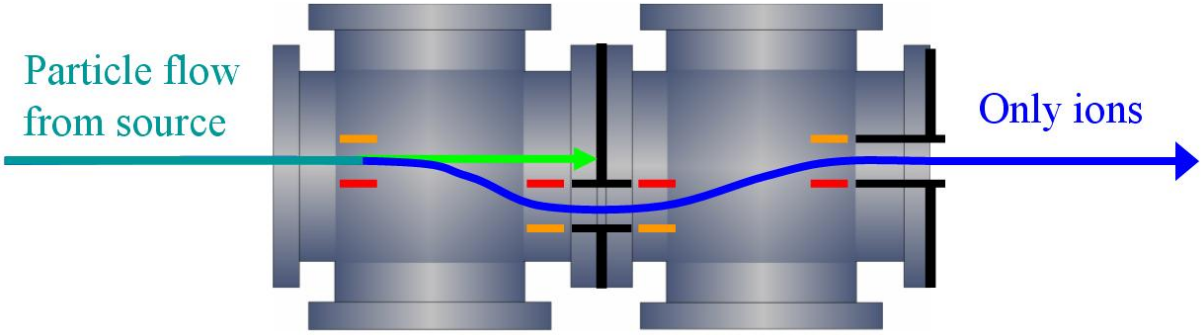

Figure 3.14: *The beam cleaner is an essential component of the differential pumping system which guides the ion beam with deflection plates through tubes. Hence, neutral particles from the source can not access the trapping area.*

ing pipes are installed. Behind the CTF the pressures can be kept much lower than in front due to the far distance to the source and the lower beam intensity reaching this area.

Baking equipment

As mentioned before the ability of baking the whole experimental chamber of the CTF has been included. Therefore, heating coils are installed on each of the different chambers and fed to the outside separately. This is important because of the different chamber masses each heating current needs to be controlled separately.
Furthermore, the first ultra high vacuum bakeable cryo pump has been attached to the beam pipe of the CTF. It consists of a charcoal layer which is positioned concentrically around the beam pipe. The cooling is realized by a copper connection to a cold head which is mounted on the isolation vacuum chamber. The essential feature is the possibility to disconnect the cold head from the cryo pump to protect it during bake-out. Using this technique the cryo pump can also be baked and thereby cleaned.
To activated the NEG strips temperatures of at least 320 °C are needed. During the baking process it is important to decrease the temperature of the cryo pump before the NEG strips reach their activation temperature. Otherwise, too much gas coming out of the cryo pump is directly pumped by the NEGs and pollutes them.
In addition, the 80 Kelvin shields are equipped with a water cooling system consisting of copper pipes mounted onto the shields. The multi-layer insulation on the outside of the

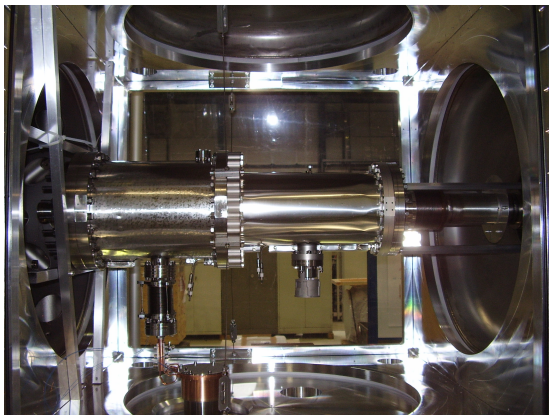

(a) Cryo pump mounted inside the cubic chamber with copper connection to the cold head below

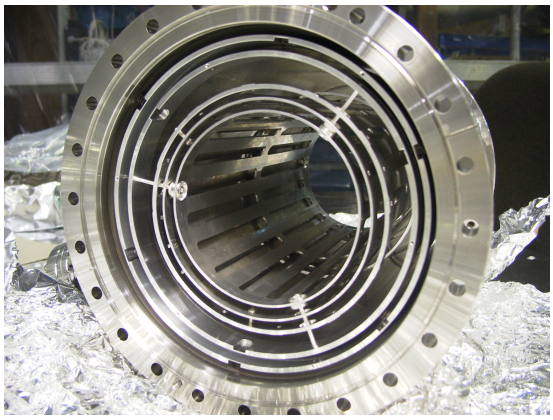

(b) Charcoal layers inside the cryo pump

Figure 3.15: *The first ultra high vacuum bakeable cryo pump which can be disconnected from its cold head for the baking process*

Figure 3.16: *Water cooling pipes on the 80K radiation shields to protect the multi-layer insulation during the bake-out*

80 Kelvin shields can only resist up to 250 °C (120 °C for the CSR) and the water cooling keeps the temperature below this (fig. 3.16).

Isolation vacuum system

The isolation vacuum consists of a huge vacuum chamber which is mainly pumped by two turbo pumps positioned on top of the entrance chamber and the bottom of the exit (fig. 3.13). To initially pump the vacuum a roots pump is connected on the middle chamber to speed up the process. Two molecular sieves are also included in the vacuum system and fixed to the shield helium pipes. During the cool-down the sieves and also all cold parts like the shield or the outside of the cold chamber, respectively, are improving the vacuum conditions by binding gases through condensation. The pressure at room temperature is in the order of 10^{-5} mbar whereas at cold conditions an isolation vacuum of 10^{-7} to 10^{-8} mbar is reached. For the case of an overpressure in the isolation vacuum, a 100 mm safety-lid is installed at the top of the middle chamber.

3.2 Experimental procedure

This section describes the procedure of an experiment starting with the ion injection and preparation, the ion trapping and also the detection and counting of the neutral fragments out of the trap.

3.2.1 Ion injection and beam preparation

Measurements have been mainly performed using singly-charged molecular nitrogen ions N_2^+ with energies between 2 and 10 keV. These ions are created and accelerated to their final energy by a cold-cathode penning ion source. It consists of an anode shaped like a hollow cylinder with end caps on both sides forming the cathodes. Through a gas inlet on one side the nitrogen gas can stream in the center of the anode. By applying a high-voltage of 800 to 1500 V on the anode and keeping a continuous gas stream, a self-preserving ionization process occurs. The primary created electrons start the burning process and ionize more gas by electron impact. To bind the electrons for a longer time a magnetic field parallel to the cylinder axis is attached and forces them to oscillate between the cathodes. By applying a high-voltage on the extraction electrode the ions are drawn through a small hole out of the plasma.
After creation and acceleration the ions are focused by an einzel lens through some slits which define the beam size and thereby the beam current (left side of fig. 3.17). In the next step the ions are guided through the beam cleaner which has already been introduced in the vacuum section. In addition to the deflection plates, which clean the beam from neutral fragments, steerer are included in the entrance and exit region to change the vertical and horizontal position of the beam. The last ion optical element is the second einzel lens which finally focuses the beam in the trapping area. The amount of trapped ions and the population of ion trajectories in the trap is very sensitive on this voltage.
As described in the second chapter the trap itself consists of two stacks of symmetrically mirror electrodes which reflect the beam like an optical resonator. To inject the ions the voltages on the first mirror are switched off or just lowered to create an access to the trap. In the time of reflection on the second mirror these voltages are also turned on and the ions are bound by the potential.
For instance, the trap can be filled completely by using a constant ion beam and switching on the electrode voltages after the beginning of the reflected beam has left the trap. Otherwise, one can inject only a short ion bunch and make use of a more precise switch timing for the trap voltages. For this purpose, the beam cleaner additionally is working

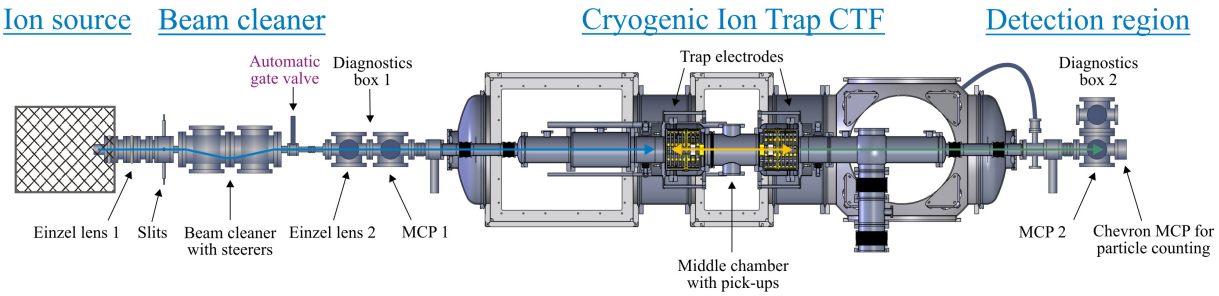

Figure 3.17: *The complete beam line including the ion source, ion optics and diagnostics as well as the CTF and the detection region behind. (Enlarged picture is given in the appendix)*

as chopper to define the bunch length. Therefore, the voltages on the deflection plates can be quickly switched and only a short bunch of a few microseconds can pass.

3.2.2 Ion diagnostics and detection system

The position and profile of the injected ion beam can be verified by two diagnostics boxes (DB1, DB2) positioned in front and behind the CTF, respectively. They both consist of a micro-channel plate (MCP), phosphor screen and camera combination. Secondary electrons are created on an aluminum plate which is moved into the beam, and afterwards they are accelerated towards the MCP by a high-voltage grid on top of the plate.
The micro-channel plate is composed of a thin plate from highly resistive material with regular tiny tubes. These tubes are typically 10 micrometers in diameter and leading from one face to the other. Furthermore, they are parallel to each other but have an angle towards the surfaces. Thereby, perpendicular impacting particles can not access directly and create secondary electrons by hitting the channel walls. A voltage between the two faces accelerates the electrons through the tubes where they release secondary electrons in wall collisions. The resulting electron cloud is accelerated further onto the phosphor screen behind the MCP. This kind of technique can amplify the original signal by several orders of magnitude.
The impacting electrons create fluorescing points on the phosphor screen which are also visible on its backside and can be monitored by a camera. Thereby, the shape and position of the beam inside the beam pipe can be observed.
To perform particle counting for storage lifetime measurements, a third MCP is applied on the end of the beam pipe (far right on fig. 3.17). In this case the ions directly impact on the MCP and create the secondary electrons. Furthermore, the MCP complex consists of two MCPs positioned close behind each other and with a small gap in between. The

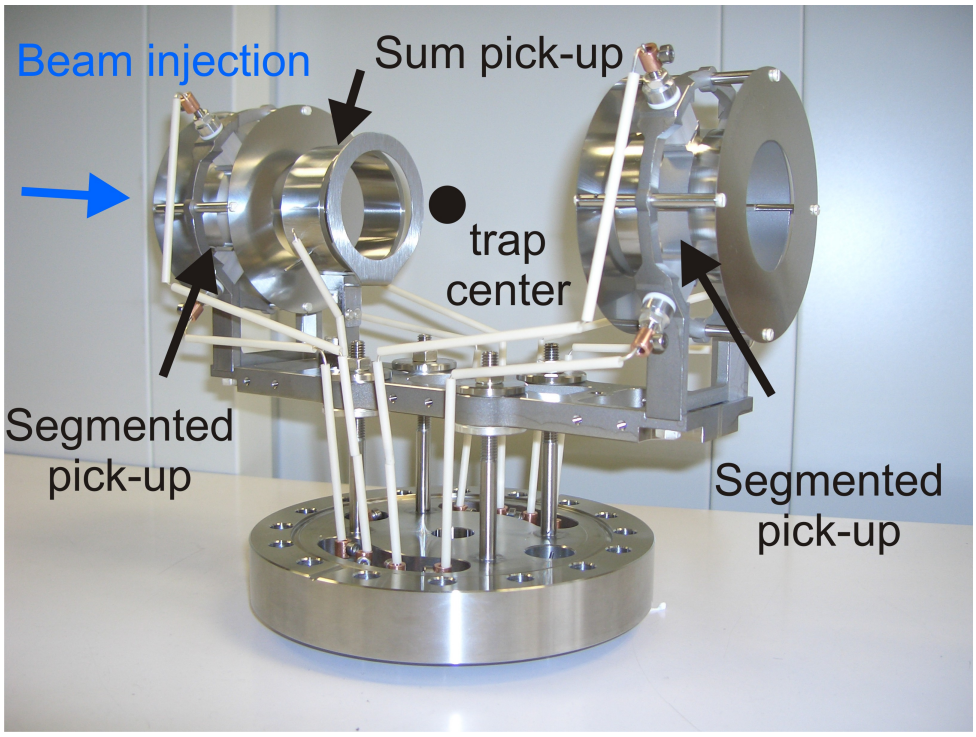

Figure 3.18: *Setup of the pick-ups in the center of the CTF used for non-destructive observation of the beam to determine the bunch length and beam current*

channels still have an angle to their surface but to opposite directions. Thereby, the secondary electrons in the first MCP can not directly pass a channel of the second one and will again create more electrons. The small gap gives the opportunity for electrons from one channel to spread up into more channels which leads to a higher amplification. However, the double-MCP setup yields an intensive signal and is called a Chevron MCP. The particle counting is indeed not realized by using the signal on the phosphor screen and camera behind, it is furthermore accomplished by counting the MCP voltage fluctuations with a common time resolution of 1 MHz. This is quite sufficient as the data has to be binned to a lower resolution anyway (typically 1-100 ms). Technically, the signal is amplified first and guided through a discriminator. The barrier on the discriminator whether a fluctuation is counted or not has to be set to the optimum of the signal to noise ratio.

It is important to know that the angular acceptance of the MCP is approximately ± 8 mrad for neutral fragments coming from the center of the trap, whereas the position acceptance is ± 20 mm which corresponds just to the diameter of the MCP. Compared to the phasespace of the ions in the trap center the position space is far covered by the

MCP face but due to the far distance not the whole angular space which is typically ± 15 mrad (compare fig. 2.5). However, this does not matter for the result of the storage lifetime since it only decreases the statistics.
Furthermore, the trapped ion beam can be monitored by a pick-up setup which is positioned in the center of the trap and gives the opportunity of a non-destructive observation of the beam. When the ion bunch passes through the pick-up a voltage is induced, afterwards amplified and observed on an oscilloscope. A picture of the pick-up is shown on figure 3.18. The sum pick-up is a tube of 2 cm length and 4 cm diameter and is used to measure the total time-dependent current of the ion bunch. The two segmented pick-ups on both sides consist of longitudinal separated tubes into quarters and by substracting the measured voltages of two opposite sides the beam position can also be determined.

3.3 Controlling methods

3.3.1 Control computers

The whole complex measurement, diagnostics and controlling progress is realized by four normal desktop computers. One of them is only responsible for the data recording and displaying of the temperatures inside the CTF. The approximately 50 temperature sensors are read-out each minute and the hourly temperature rate is calculated automatically. This is especially important to monitor and control the cooling and warming processes.
From the second computer the high-voltage parts are addressed like, for instance, the einzel lenses, trap electrodes or MCP voltages. A whole parameter setup also including the source and steerer values can be saved to one file and recalled at a later time.
The timing for the injection and trapping and also the data acquisition of particle counting are all controlled by the third computer. The short time pulses and fast signal processing is realized by a National Instruments timing card device and LabView has been used for all these controlling programs.
And finally, the data analysis has been processed on the last computer by using mainly Origin 8.

3.3.2 Electrical connections

As the trap potential is always symmetric, both corresponding electrodes on each side are connected to the same power supply. In total five power supplies support the voltage for all different electrodes separately. In case of the switched electrode side the voltages are first guided through fast high-voltage switches which are triggered by a TTL signal from the timing card.
A characteristic rising edge of the voltage is shown in figure 3.19. The blue curve shows the high-voltage signal and the green curve the TTL trigger pulse. The time constant τ_C of the rising edge defined by the formula 2.1 has a value of approximately 140 ns. The rising time to 95 % of the maximum voltage is given by 420 ns and is more than an order of magnitude lower than the oscillation time of the ions in the trap.
For the temperature measurements some sensor types are connected to small amplifier boxes close to the feed-through from the isolation vacuum chamber. Especially for the platinum sensors which are only using the 2-lead measurement an early amplification is necessary. For the silicon and rhodium-iron sensors which are read-out through a 4-lead measurement this close amplification is not required but it has been installed also for the

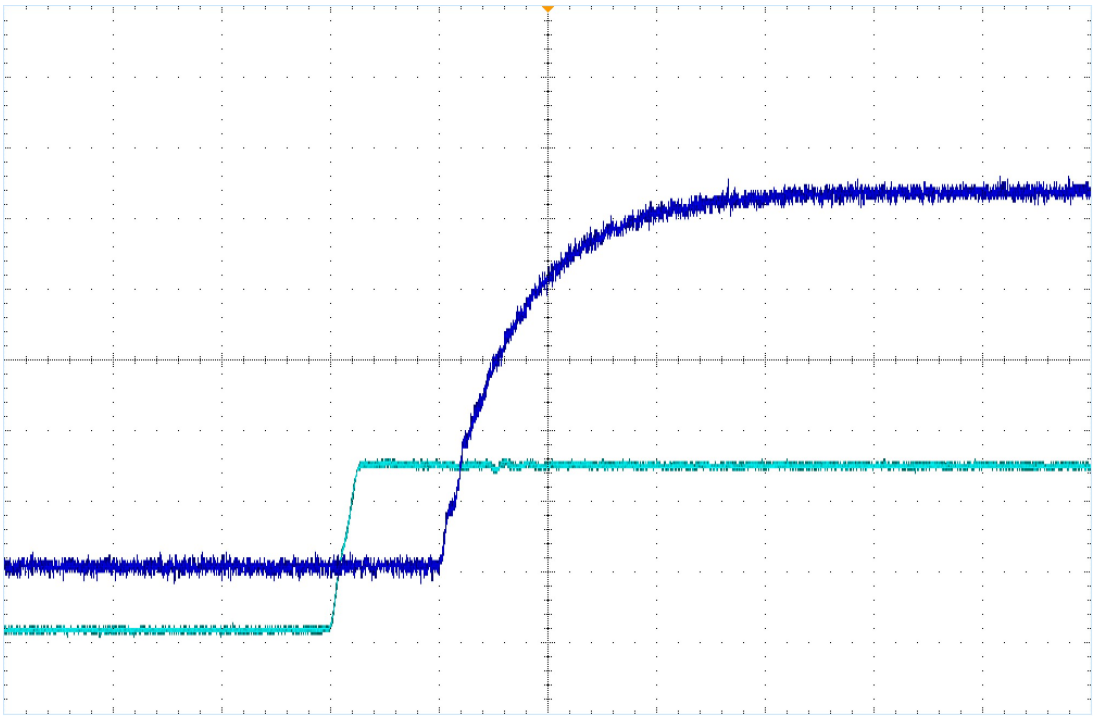

Figure 3.19: *The figure shows the rising edge of a switching pulse coming from a high-voltage switch. The blue curve represents the high-voltage signal whereas the green curve is the activating TTL signal. The grid shows in x-direction the time in steps of 200 ns and in y-direction the voltage with a scale of 2 V for the trigger and 2 kV for the HV signal, respectively. The time constant τ_C defined by the formula 2.1 has a value of approximately 140 ns. This leads to a rising time of 420 ns to reach 95 % of the maximum voltage.*

silicon sensors.

3.3.3 CTF Interlock system

The CTF interlock system has been employed to avoid damaging the device or even people via switching off critical parts under unsuitable conditions. The whole operating mode can be divided into two separated parts, the normal trap operation under cold or warm conditions and the baking situation. The complete interface is show schematically in figure 3.20.

The inputs on the left side of the schematic interlock box are the control signals coming from different systems and indicating whether the corresponding device is operating in normal mode. If an error occurs at an input the connected outputs are switched off due to safety reasons.

The most important part are the connections for the normal trap operation. Therefore,

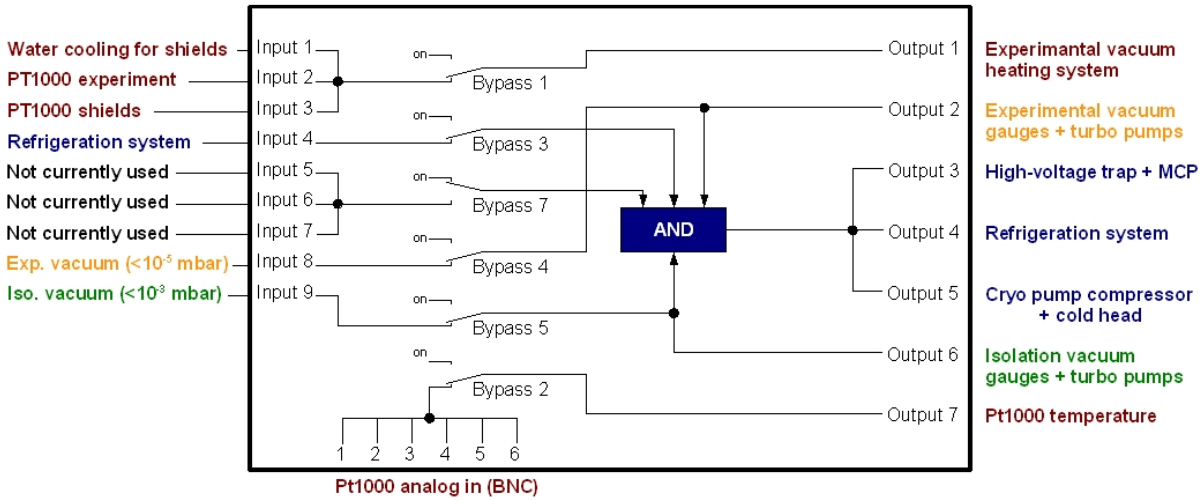

Figure 3.20: *Schematic view of the CTF interlock system: The inputs are control signals which indicate whether the corresponding component is operating within normal mode. The outputs on the other side are used to turn off critical components in case of one or more disabled inputs.*

the outputs 3 to 5 have to be enabled which are the high-voltage on the trap and MCP, the refrigeration system for cold measurements and the cryo pump compressor for the cold head, respectively. They are all switched off if one of the connections to the 'AND' box shows an error. This can be triggered by a problem with the refrigeration system or at least by one of the pressures in the two vacuum systems being above their defined limit. These are 10^{-5} mbar for the experimental and 10^{-3} mbar for the isolation pressure. At normal conditions the pressures are far below the limitation as the experimental pressure is at least 10^{-9} mbar and the isolation vacuum at 10^{-5} mbar, both for warm operation.

If the experimental pressure gets worse, for instance, caused by a sudden vacuum leak or a quickly desorbed amount of frozen gas, the high-voltage on the electrodes and the MCP have to be switched off to prevent an increasing number of discharges which could destroy several parts. A worse pressure also leads to higher heat input through heat convection which may be too large for the refrigeration system.

For a worse pressure in the isolation vacuum it is a very similar situation. The cold chamber and the radiation shields would heat up very fast and due to this huge heat input the refrigeration system would have to be turned off. Also the high-voltage for the electrodes would have to be disconnected because their blank supply lines are only isolated against discharging at sufficient vacuum conditions. In both cases of a worse pressure, the corre-

sponding pressure gauges are turned off, and turbo pumps are separated from the vacuum to protect them.
The second part controls the baking process. Therefore, the water cooling for the shields has to be activated. Furthermore, the temperature sensors on the cold chamber need to be connected to control the baking. They are attached to the interlock box on the bottom side and creating a separate output signal which enables the inputs 2 and 3 for the temperatures.

4. Measurements with the CTF

In this chapter the performed measurements and obtained results from the Cryogenic ion trap are described. Initially, the first cool-down processes are introduced of which the first one has been accomplished with no ion trapping at all. The temperature distribution at cryogenic conditions along the experimental chamber will be compared for three different cool-downs.
After that, the procedure of ion trapping is implemented consisting of the correct injection, focusing and timing settings. These first storage lifetime measurements have been performed at room temperature by initially using a positive Argon ion beam (Ar^+) and later switching to the singly charged molecular nitrogen beam (N_2^+). The nitrogen ions have been also used to measure the storage lifetime during the cool-down procedure and at cryogenic conditions, which will be presented subsequently.

4.1 Cryogenic cooling tests

The refrigeration system was designed to support enough cooling power for the whole Cryogenic Storage Ring (CSR), which means the cooling of the radiation shields to 40 and 80 Kelvin, respectively, and most importantly all the inner experimental chambers to approximately 10 Kelvin and at several positions to even 2 Kelvin. Compared to the CSR with a planned circumference of about 35 meters the cryogenic ion trap has only a tenth of this length. Hence, the cooling power has to be regulated by the refrigeration system, and the cooling process has to be slowed down in such a way than the temperature gradients especially on the cold chamber stay sufficiently small. The cold chamber components which are well connected to the helium pipes quickly reach the temperature of the helium whereas the heat conduction to other positions takes more time. An estimation has led to an adequate deviation in the temperature of 40 Kelvin between the warmest position at the cold chamber and the incoming helium flow.

4.1.1 The first cool-downs

For the first cool-down the refrigeration system has been controlled manually, which means that the helium flow and temperature have been influenced by modulating valves while carefully watching the temperatures inside the CTF. For the next cooling procedure a more automatic mode has been included in the refrigerator control system. Thereby, only one valve was used to control the helium flow. Finally, at the third cool-down a fully automatic system was implemented. Therefore, one temperature sensor inside the CTF has been read by the refrigeration system and was used to control the helium flow and temperature. This sensor is positioned on the cold chamber and has a far distance to helium pipe connections. The incoming helium temperature is regulated to stay within 40 K of this sensor.
In addition, for the first cool-down the two vacuum systems have been connected together and formed a combined vacuum chamber. As no ion trapping was planned for this cooling process the middle chamber had not been included. The main goal was at first to verify the cold temperatures on the cold chamber and the expected temperatures on the radiation shields. For further cool-downs the middle chamber had been installed and measurements with trapped ions have been performed, but in this section the main aspect will be the temperatures and also the measured pressures from the gauges on the outside of the CTF. Here, it also important to note that the turbo pump as well as the ion getter pump have not been used at cryogenic temperatures and hence, they have been separated from the vacuum system by valves. The pressure in this region has been measured to be improved without these connected pumps.

Figure 4.2 shows some important temperatures during the first three cool-downs. All three diagrams have a time scale of 10 days on the x-axis and the temperature in Kelvin. The displayed sensors are silicon diodes or rhodium iron sensors, respectively, which both have a high precision at temperatures down to one Kelvin.
The temperature distribution for the first cool-down shows two conspicuous steps for approximately one day. There, the refrigeration system had been shut down for this time and no temperature measurement were performed. Compared to the other distributions, the temperature is increasing again, and the whole cooling procedure took two days longer. Furthermore, the missing data points in all of the figures were caused by some problems with the temperature data acquisition program which have been improved for future cool-downs.
The silicon sensor on the ion gauge flange represented by the black curve has a far distance to the cooling units or helium pipe connections. In contrast, the silicon sensor on the cryo

pump flange is positioned on a copper bridge between the flange and the cooling unit. Furthermore, the rhodium iron sensor represented by the blue points is mounted directly on the cooling unit, and it is expected to measure the lowest temperature.
In the first figure one can see that the black curve stays even more than 50 Kelvin above the others. This evidence has been used to improve the next cool-downs, and a better thermal connection has been installed. On the second and third figure the temperatures stay closer together and the cooling process is getting more controlled by the automatic regulation.
The strong decrease of the temperatures beginning at roughly 100 Kelvin occurs due to the fact that the thermal conductivity of copper increases. For copper of 99.95 % purity the effect leads to a maximum in the conductivity at 30 Kelvin and nearly one order of magnitude higher value as that at 100 Kelvin. This type of copper was mainly used to connect the shields to helium pipes and to each other. For thermal connections on the cold chamber a high purity copper of 99.997 % has been employed. This material reaches the maximum thermal conductivity at roughly 10 Kelvin at a two orders of magnitude higher value.
In the second and third figure the temperature of the middle chamber is included (green curve). Due to good thermal connections from the vertical cooling unit in the center of the device the temperature can excellently follow the other temperatures. The thermal bond from the vertical cooling unit is connected to the flanges on both sides of the middle chamber and also to a copper foil which is wrapped around the chamber.

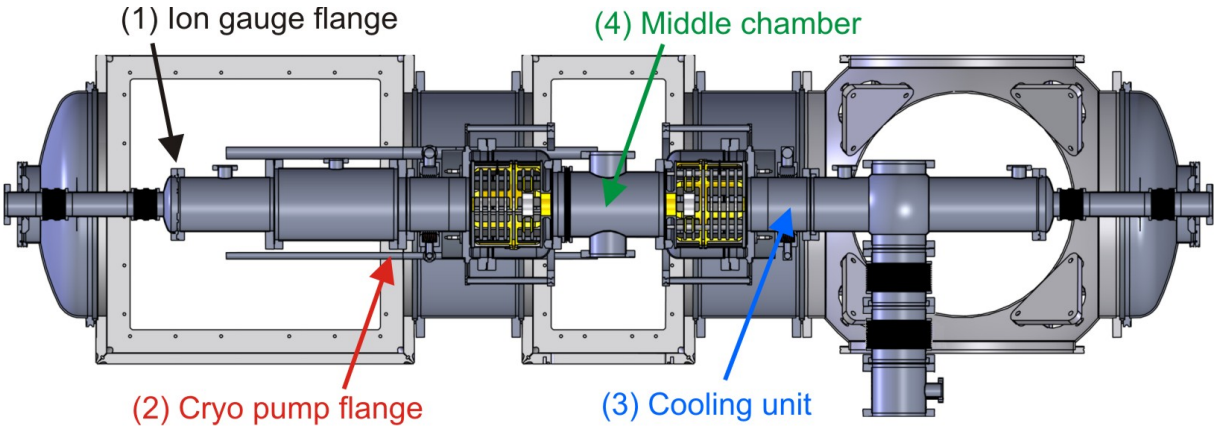

Figure 4.1: *Important temperature sensor locations which have been used in figure 4.2. The sensor on the cooling unit (3) is expected to measure the lowest temperatures whereas in contrast, the sensor on the ion gauge flange (1) has a far distance to the cooling unit. The two other sensors are expected to measure medium temperatures.*

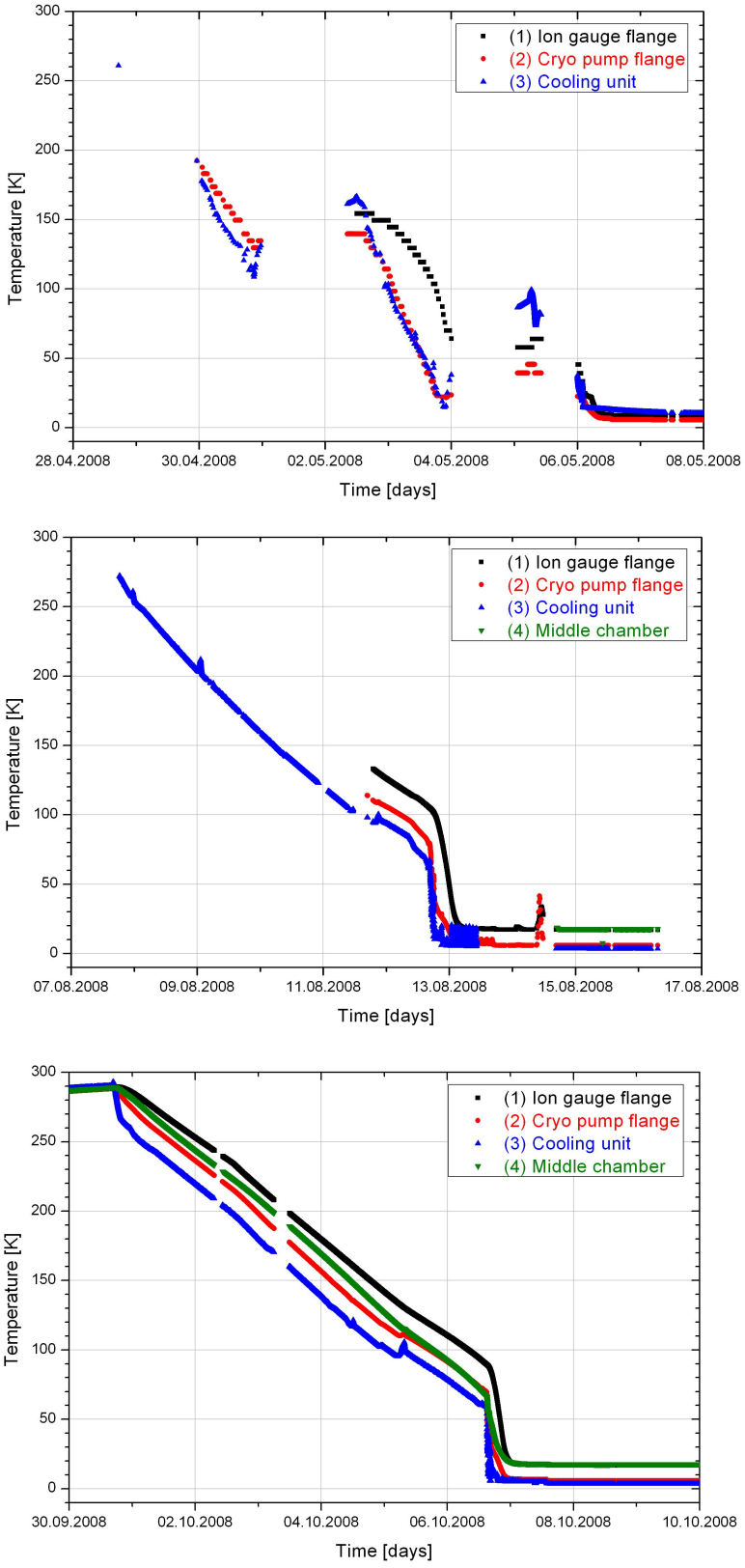

Figure 4.2: *The first three cool-downs which have been accomplished with the CTF. The corresponding sensor locations of these temperatures are given and described in figure 4.1. The middle chamber had not been installed for the first cool-down so no ion trapping was performed.*

The final achieved temperatures at cryogenic conditions will be presented in the next figure and compare the three different cool-downs.
The mean temperature on the cold chamber was measured to be around 17 Kelvin where the lowest temperatures were below 6 Kelvin and for the last cool-downs near 3 Kelvin. Especially for the last two cool-downs, the helium in the 2 Kelvin cycle has even reached 1.8 Kelvin in both the supply and return helium lines.
The 40 Kelvin shields have reached mean temperatures of about 36 to 37 Kelvin for the last two cool-downs and 70 Kelvin were observed at the 80 Kelvin shields. Especially for the 80 Kelvin shields the values of the first cool-down are due to the few temperatures hard to use for a comparison. In summary, the cold chamber has a good overall temperature, the cooling units reached their lowest value, and the 40 and 80 Kelvin shields have achieved lower temperatures than expected.

4.1.2 Cryogenic temperature distribution and thermal coupling

In the following, a closer examination of the lowest accomplished temperatures distributed over the cold chamber will be performed. In figure 4.3 the temperature distribution is shown for all cool-downs, starting on the left side with ion gauge and cryo pump chambers followed by the first cooling unit and electrode stack. After the middle chamber, comes the second electrode chamber and cooling unit as well as the pump cross chamber with the connection to the other pumps below.
At first, two positions of very low temperature are visible which are the regions of the two cooling units. The asymmetric shape in the center of the first figure is due to the fact that some temperature sensors were not used and the middle chamber was not installed for the first cool-down. Furthermore, on all figures the temperatures on the right side of the distribution are noticeably higher. Due to the connection to the pumps below and the exit beam pipe, the pump cross chamber has a higher heat load which is reflected in the higher temperatures.
The pump cross chamber during the first cool-down has not reached the low temperatures of the following cool-downs. The reason could be that the radiation flap positioned in the pump pipe below could not be closed during the first cool-down. It had to stay open for the initial pumping with the turbo and ion getter pump as at this time flap operation from outside the isolation vacuum chamber was not possible. For the following cool-downs a mechanism was included to allow this movement which resulted in a decreased radiation heat load leading to a lower temperature of roughly 5 Kelvin.

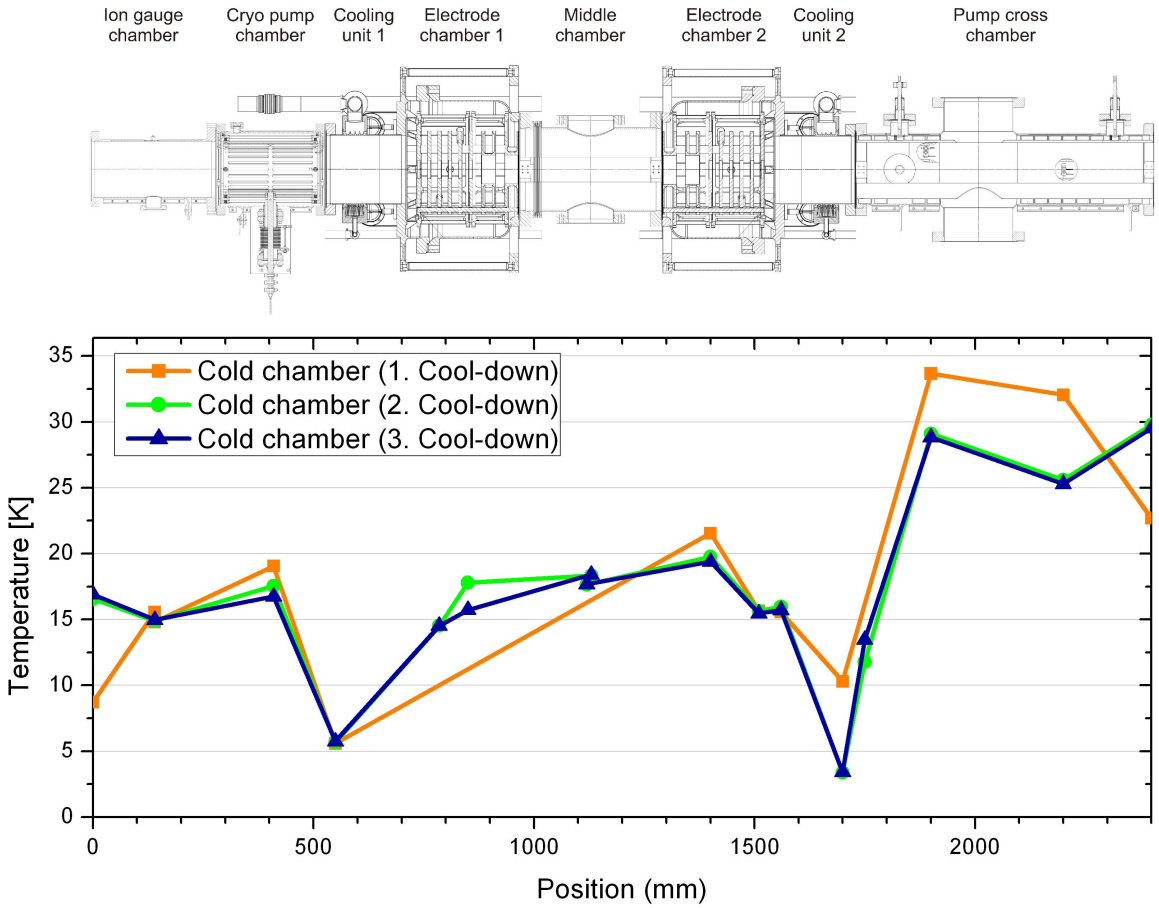

Figure 4.3: *Comparison of the final temperatures for the first three cool-downs distributed over the complete cold chamber.*

Furthermore, the temperature on the right cooling unit has only reached 10 K which could be explained by the additional heat load from the pump chamber but also due to a bad thermal contact between the rhodium iron sensor and the cooling unit chamber. The temperature, however, has improved in later cool-downs.

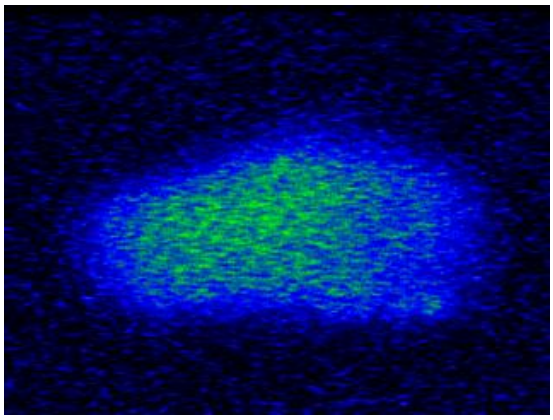

(a) MCP in the diagnostics chamber in front of the CTF

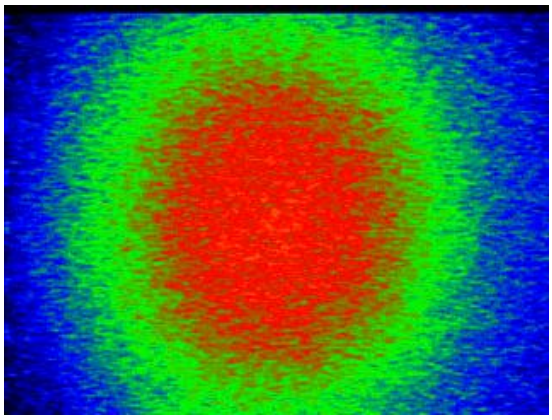

(b) MCP in the diagnostics chamber behind the CTF

Figure 4.4: *The two pictures are taken with the cameras looking at the phosphor screen in the two diagnostics chambers. The colors are produced by the measuring program to increase the contrast. The signal strength is strongly dependent on the beam intensity and the MCP and phosphor screen voltages. However, the more important information for the optimization process is the shape and position of the ion beam signal.*

4.2 Trap operation

The ion optical possibilities for beam preparation and ion diagnostics have already been introduced in section 3.2 of the experimental procedure. This part focuses on the phase when the different optics elements were taken into operation, and the timing scheme for trapping was optimized.

First of all, the ions are produced in the source and accelerated shortly after to their final kinetic energy. Afterwards, they are guided through the beam cleaner using a constant voltage on the deflectors which produces a continuous ion beam. On the first ion diagnostic chamber the beam is observed on the MCP and optimized with respect to its shape and position by lenses and steerers. Accordingly, the beam signal on the second MCP behind the trap is also improved while no electrode voltages are applied at the trap. The observation on the two MCPs leads to an ion beam which is exactly in the center of the beam pipe, and hence, in the center of the trap. Figure 4.4 shows two pictures of the beam taken by the cameras behind the phosphor screens of the diagnostic MCPs.

In the following, the beam is chopped into small bunches by the beam cleaner. As mentioned before, the deflection plates in the beam cleaner can be switched quickly, thereby defining the bunch length. This short beam signal can be observed by the sum pick-up which is positioned in the center of the trap (compare fig. 3.18).

In figure 4.5 three pictures of pick-up bunch signals are shown, observed with the sum

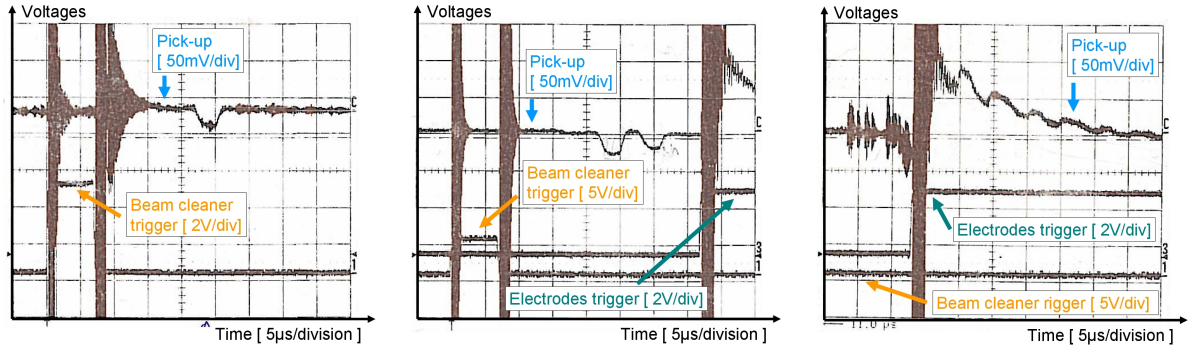

(a) The initial bunch on the sum pick-up without any electrode voltages

(b) Bunch signals with reflection on static exit electrodes

(c) Trapped ion bunches

Figure 4.5: *First trapped ion bunch with Ar^+ at 5 keV recorded with the sum pick-up connected to an amplifier and an oscilloscope. The time duration and strength of the observable pick-up signals was further improved. The strong noise on the pick-up signal is produced via cross talk by the high-voltage switching. A timing scheme is given in fig. 4.6.*

pick-up and recorded by the oscilloscope. The first diagram shows on the upper curve the pick-up voltage and on the lower the beam cleaner trigger signal. Here, the trigger is activated for 7 μs and in this time the beam cleaner deflection plates are at high voltage. Due to the fact that all plates are switched at the same time, a part of the ion bunch will be lost in the beam cleaner. The difference of the trigger duration and the real bunch length is usually 2 to 3 μs depending on the energy. So the bunch signal on the pick-up, represented by the downward pulse, is in this case only 4 μs long. The strong noise on the pick-up signal at the beginning is produced via cross talk by the high voltage switching of the beam cleaner.

At first, the bunch is observed without any trap voltages to verify that the beam is aligned correctly in the center line and, for instance, not accidentally deflected by a charging effect in the beam line. Afterwards, the electrode voltages are turned on and the reflected bunch is also visible (fig. 4.5 (b)). As the trap voltages for the entrance side have been switched purposely after the bunch has left the trap, the bunch is not trapped at this moment. This was done to initially see a clean reflection signal because the switching noise would completely hide it.

On the last picture one can see the trapped bunch via the periodic pulses in the pick-up signal. The electrode trigger switches right after the first bunch signal and again produces strong noise on the pick-up signal. Afterwards, the time duration and strength of the observable pick-up signals has been further improved by changing trap voltages

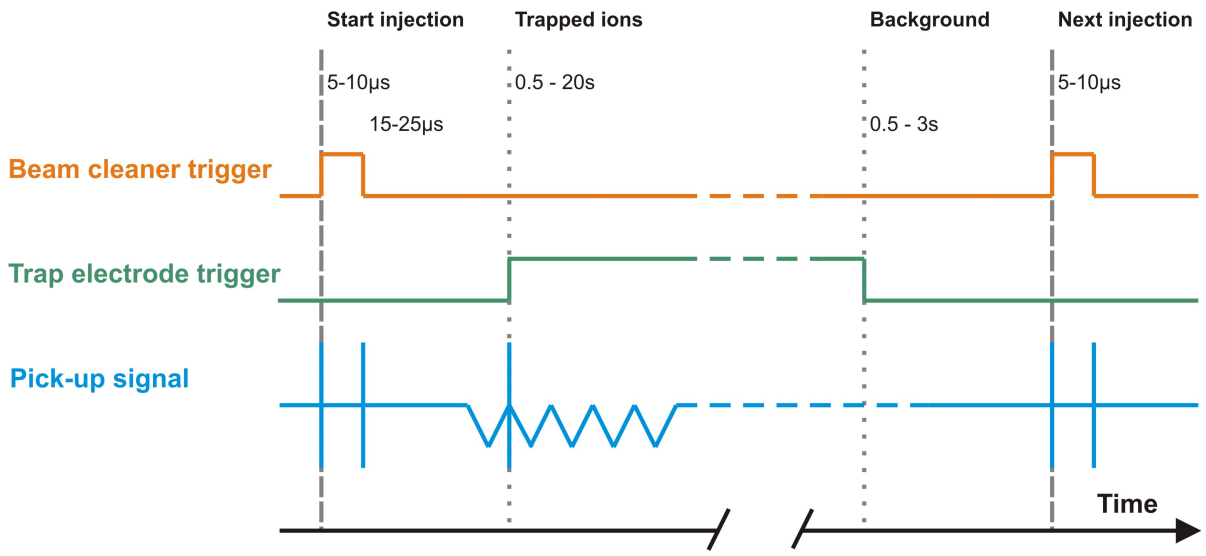

Figure 4.6: *Timing scheme of storage lifetime measurements with trapped ions. The injection is initialized by the beam cleaner trigger. After the time of flight of the ions to the trap, the entrance electrodes are switched on. The duration of the ion trapping and the background measurement has usually been chosen to be around the order of the observed lifetime.*

and injection settings.

Figure 4.6 shows a schematic view of the timing scheme which is used to trap the ions. Depending on the current vacuum conditions and the correlated storage lifetime, the trapping time has been changed in order to collect sufficient statistics. The storage time was usually chosen to be around the order of the storage lifetime.

The background rate of the MCP without stored ions was measured after each injection by switching off the entrance electrode voltages to release the ions and further recording the count rate. The measurement of the background rate is required to gain the real count rate of neutral fragments after substracting the background.

In the case of figure 4.5 (c), the bunch decays very quickly which further on will be changed by more optimization steps. Besides the optimization of the trap voltages, the focusing of the ions into the trap is also changed by the second einzel lens. In addition, the steerers are also used to achieve an improved injection into the trap acceptance.

To estimate the amount of ions reaching the trap, a Faraday cup was temporarily installed in the middle chamber between the trap electrodes. Figure 4.7 shows the ion beam current which reaches the center of the trap depending on the applied beam cleaner voltage. On the right axis the initial beam current is compared to the trap current. The initial beam current from the source was measured in the Faraday cup at the beam cleaner entrance.

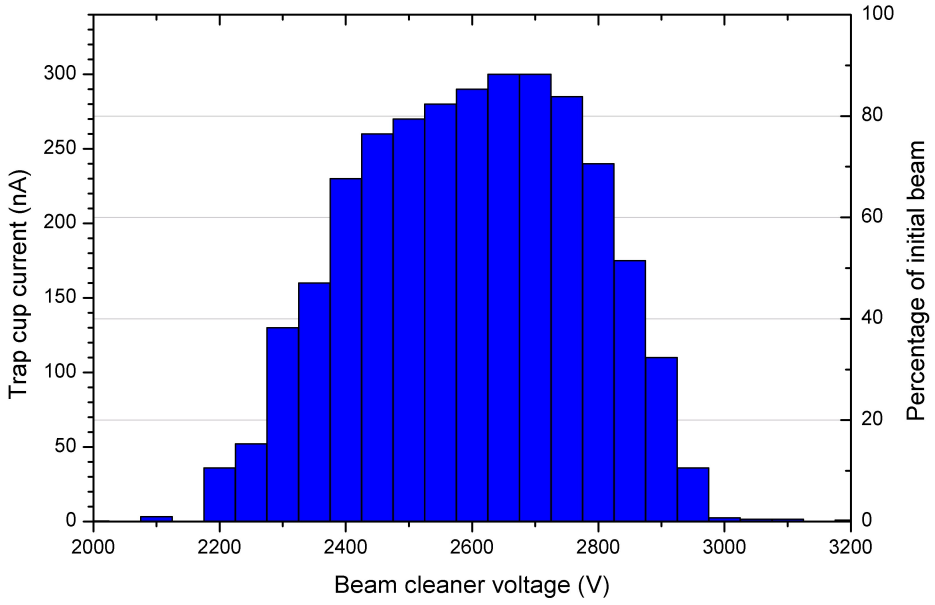

Figure 4.7: *Ion beam current reaching the trap center as a function of the applied beam cleaner voltage. The right axis shows the percentage of the initial beam current which was measured in front of the beam cleaner. A N_2^+ ion beam at 5 keV was used.*

The extraction voltage at the source and thereby the energy distribution of the ions was kept constant for the measurement. By using the optimum voltage with respect to the energy, nearly 90 percent of the initial beam will reach the trapping area. This measurement was accomplished with a N_2^+ beam at a kinetic energy of 5 keV.

4.3 Warm storage lifetime measurements

The first storage lifetime measurements were performed at room temperature by initially using a positive Argon ion beam (Ar^+). Figure 4.8 (a) shows one of the first lifetime curves accomplished with an ion energy of 5 keV and an experimental vacuum of $5 \cdot 10^{-8}$ mbar. The count rate is plotted with a bin size of 1 ms and summarized for 187 injections (starting count rate $2.27 \cdot 10^6\, s^{-1}$). The fit function for an exponential decay leads to a storage lifetime of 46.61 ± 0.04 ms (only statistical error).
For further lifetime studies, the ion beam has been changed to a single charged molecular ions N_2^+. The main reason was the rising vacuum pollution by the injected Argon due to the worse pumping properties of this gas type by the used vacuum pumps.
In figure 4.8 (b) a storage lifetime measurement of N_2^+ ions is shown using the same en-

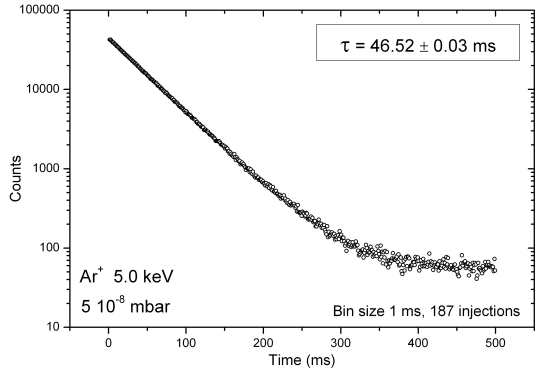

(a) Rate of neutral Ar atoms exiting the trap and measured by the MCP. Trapped Ar^+ ions with 5 keV of kinetic energy and a fitted storage lifetime of 46.61 ± 0.04 ms (only statistical error). The data is summarized over 187 injections and with a bin size of 1 ms.

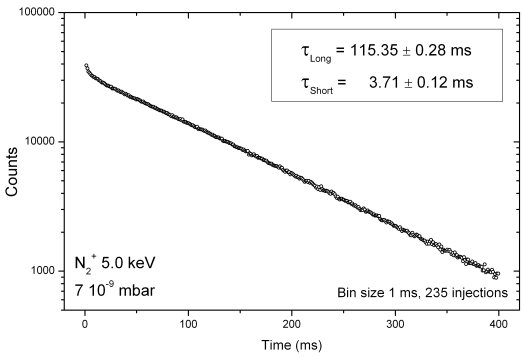

(b) Rate of neutral fragments coming from trapped N_2^+ ions and counted by the MCP. The data is summarized over 187 injections and with a bin size of 1 ms. Fitted long storage lifetime of 115.26±0.23 ms and a short lifetime of 3.54±0.07 ms (only statistical error).

Figure 4.8: *Storage lifetime curves for Ar^+ and N_2^+ at room temperature*

ergy but at a better vacuum of $7 \cdot 10^{-9}$ mbar. Besides the normal storage lifetime, a short component has been observed which only appeared for the changed ion species. The long lifetime has been determined to 115.3 ± 0.2 ms, where the short one is 3.54 ± 0.07 ms (starting count rate $1.66 \cdot 10^6\, s^{-1}$). One should note that the same injection and trap settings were not used for both measurements. Nevertheless, during the whole optimization process for Argon the short lifetime component has never been observed.
Later at cryogenic conditions, a systematic study of the short lifetime components has been performed and will be described in a later section.

4.4 Storage lifetime measurements during cool-down

After the first trapping studies at room temperature conditions were finished, the whole device was cooled down to cryogenic temperatures while performing lifetime measurements. This has been done in order to obtain the linear dependency of the reciprocal lifetime to the pressure or residual gas density (compare eqn. 2.17). As the ion gauge which measures the experimental pressure is operated at a position at room temperature, the residual gas density at this position is also linear dependent on this pressure.
Plotting the inverted lifetime as a function of the estimated residual gas density gives a

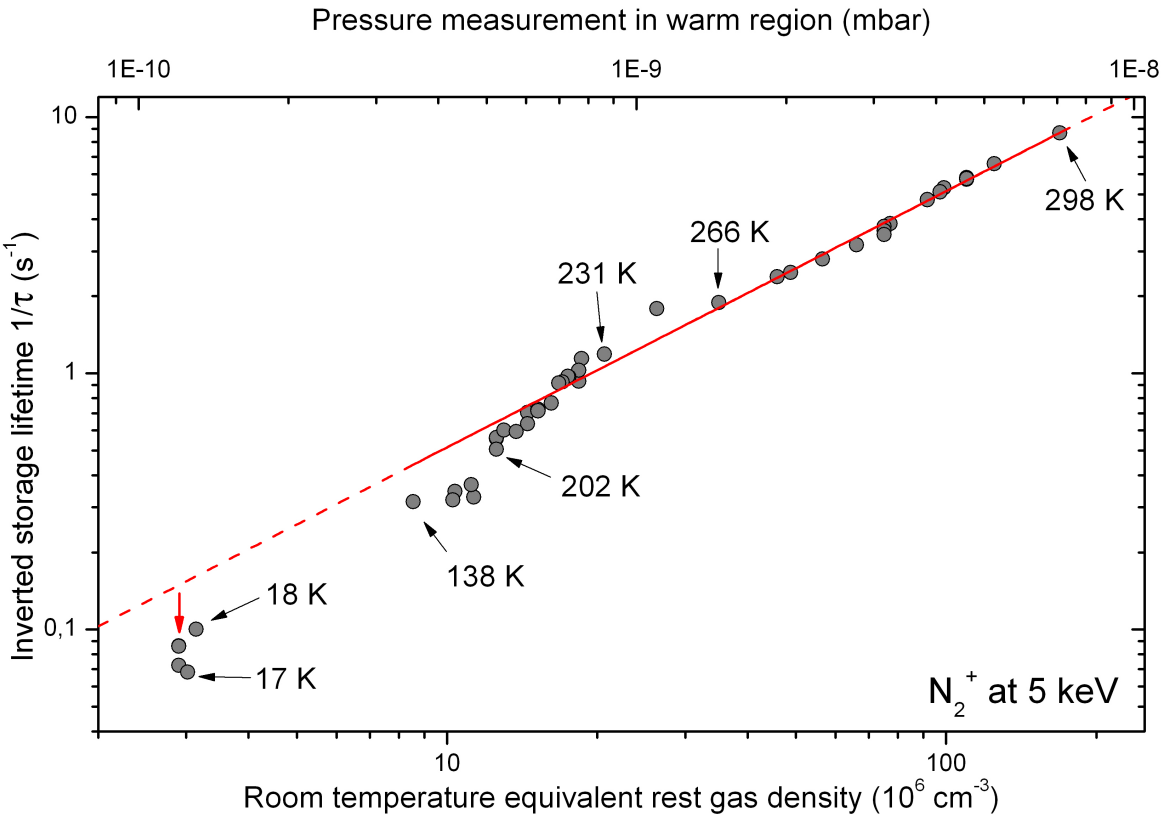

Figure 4.9: *Inverted storage lifetime during cool-down as a function of the pressure in the warm region and the corresponding residual gas density. A linear dependence for high temperatures can be observed whereas for lower ones the warm pressure measurements lead to wrong predictions. The temperature was measured on the middle chamber with a silicon diode sensor (see fig. 4.1). The statistical errors of the lifetime measurements are too small to show it in this plot range.*

very nearly linear curve for the beginning of the cooling process (see figure 4.9). As the temperature decreases the residual gas density also decreases. The red curve shows a linear fit using data points down to 200 Kelvin. The slope is given by $(5.15 \pm 0.04) \cdot 10^{-8}\ cm^3/s$ or $(1.24 \pm 0.01) \cdot 10^{9}\ (s \cdot mbar)^{-1}$, respectively.

At lower residual gas densities, the measurements are more off the linear curve due to the fact that the measured pressure in the warm region is not reflecting the real pressure in the cold trapping area.

At the final cryogenic conditions, the storage lifetime of N_2^+ ion at an energy of 5 keV was measured to be 14.70 ± 0.25 s (starting count rate $43\,s^{-1}$, see fig. 4.10). Using this lifetime and the linear fit in figure 4.9, the achieved pressure conditions can be estimated to be $5.38 \pm 0.10 \cdot 10^{-11}\ mbar$.

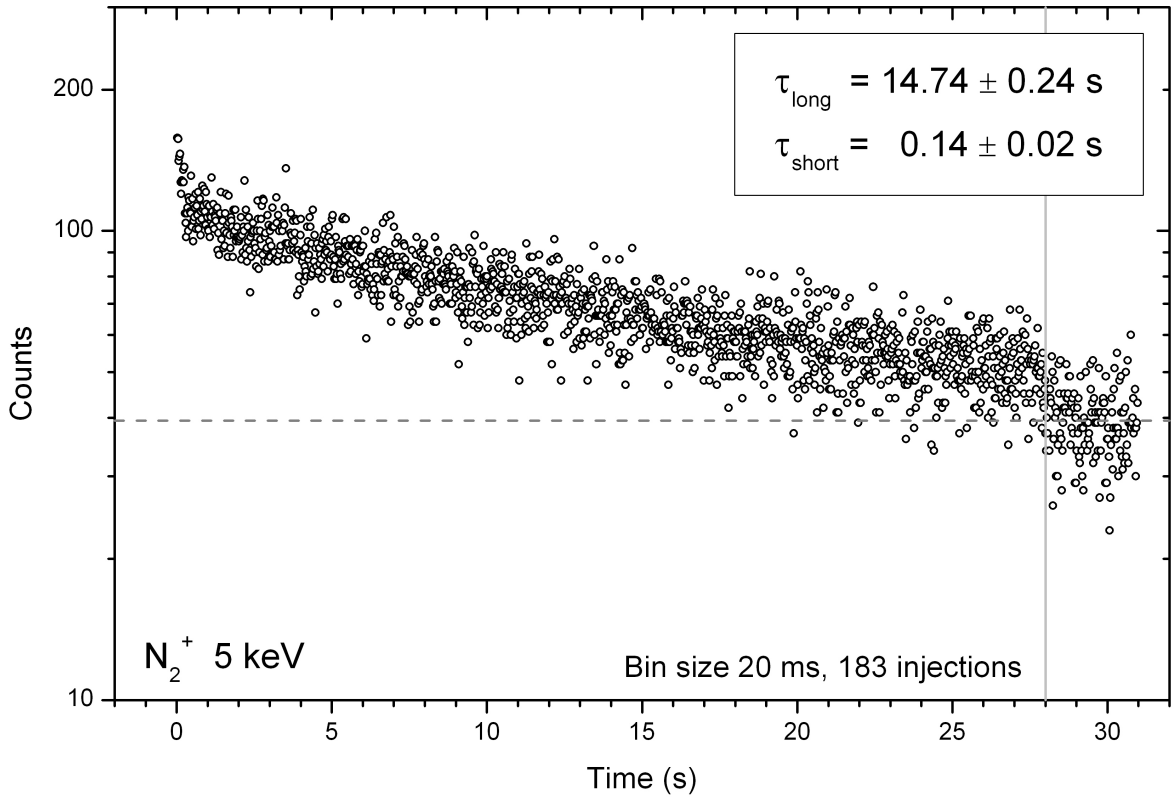

Figure 4.10: *Storage lifetime of N_2^+ ion at 5 keV was measured to be 14.70 ± 0.25 at the final cryogenic conditions. After 28 seconds of ion trapping the electrodes have been switched off to release the ions and measure the MCP background rate for 3 seconds.*

Obviously, the estimated pressure does not reflect the previous expectation of a 10^{-13} mbar. Besides the simplest assumption that the real pressure achieved is one or even two orders of magnitude lower, there is also the possibility that an unknown loss process is limiting the trapping lifetime. To characterize it further, the loss process has to be exponential because the observed count rates have not shown anything else. Furthermore, this process has to be independent of the pressure or at least have a weaker pressure dependence and becomes dominate at low vacuum conditions. However, this just suggests the possibility which will be proven later.

4.5 Ion trapping at cryogenic conditions

After the final cryogenic temperatures have been reached, some detailed investigations of the trap properties have been performed. Here, the influences of electrode voltages and injection settings, for instance, as well as that of pressure variations or of the trap timing on the storage lifetime and number of trapped ions have been explored.

4.5.1 Storage lifetime optimization

Initially, the trap potential was optimized to yield the maximum storage lifetime in order to create conditions which can be compared to the warm measurements. Each electrode voltage has been scanned for a large range of values, and the corresponding lifetime has been determined.
This measurement was also performed for several ion energies, where one result for an ion energy of 7.1 keV is given in figure 4.11. Here, electrode B which is the trap internal einzel lens (compare fig. 2.3), has been changed. The trap acceptance and hence, the number of trapped ions strongly depend on this voltage.
The left panel shows the measurements performed at cryogenic conditions, while the right side represents the corresponding results for room temperature after the warming-up. For both cases the lifetime and the number of observed neutrals N_C (compare eqn. 2.27) show a peak in the center.
The fact that the storage lifetime can be influenced by changing the trap voltages is a hint of the importance of the multiple scattering loss process. As the pressure conditions and initial ion energy stayed constant for each of the measurements, the lifetime of the electron capture loss process must also have been constant. However, by varying the focusing properties of electrode B, the trap acceptance was changed and hence, the lifetime component due to multiple scattering.
The number of observed neutrals also indicates that more ions can be trapped under the same conditions where a longer lifetime is obtained. This can be well explained by an influence of the trap acceptance on the storage lifetime.
Comparing the positions of the maxima between the cryogenic and the warm measurements shows a slight difference of 50 to 100 V. This could be an indication of a low temperature induced misalignment of the trap. The room temperature alignment could have been changed through an inhomogeneous shrinking process of the trap chamber suspension.
In the following section, the trap alignment is verified considering a different method

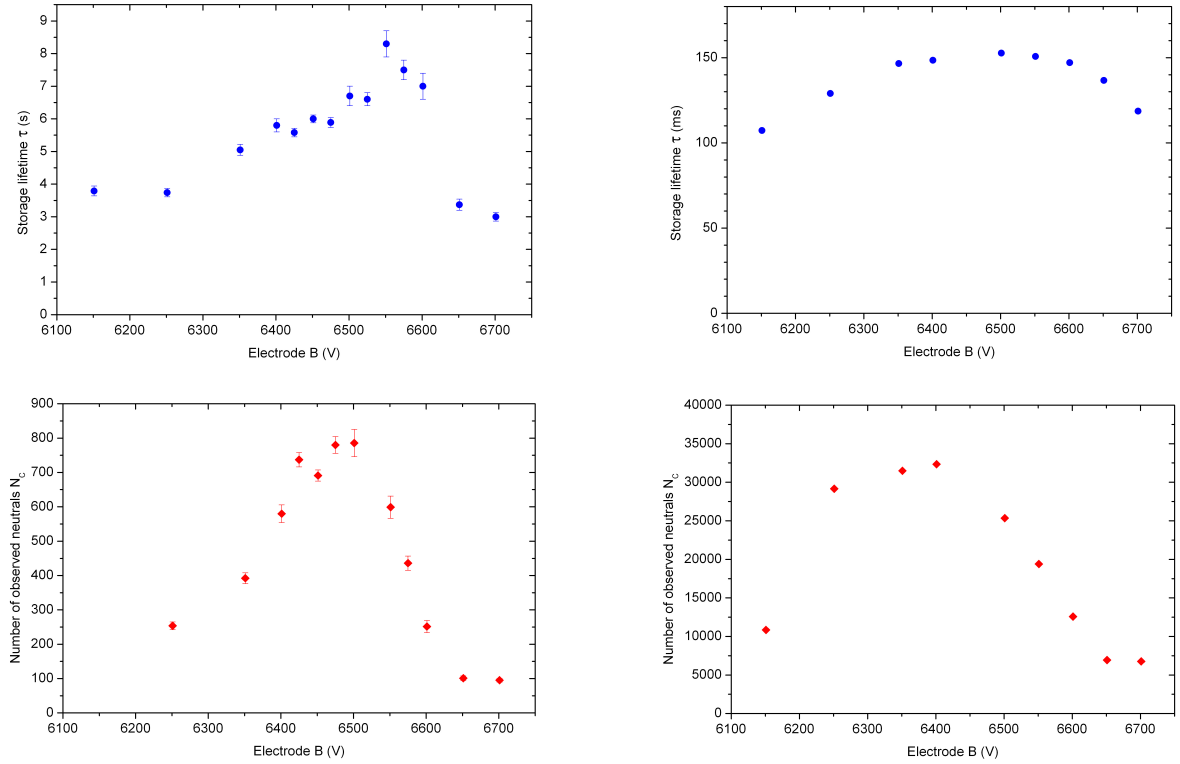

(a) Cryogenic conditions

(b) Warm conditions

Figure 4.11: *Storage lifetime and number of observed neutrals N_C (compare eqn. 2.27) as a function of the voltage on electrode B (see. fig. 2.3). A N_2^+ ion beam was used with an energy of 7.1 keV.*

applying the electrode potentials yielding the maximal lifetime.

4.5.2 Search for a low-temperature induced misalignment

Inhomogeneous shrinking processes of the trap chambers during cooling could have lead to a misalignment of the trap previously aligned at room temperature. These effects could have manifested themselves by nonparallel positions of the two trap mirror stacks at low temperature. To explore this effect, it was attempted to compensate the misalignment by deflecting the ion beam inside the trap. This was realized by applying a voltage on the segmented pick-up in order to operate it as a trap internal steerer. For instance, horizontal deflection by applying opposing voltages on the two upper and lower quarters (see fig. 3.18) was tested.

A rough calculation leads to a deflection angle of approximately 6.8 mrad for an applied voltage of ±50 V, where the pick-up was approximated by two parallel deflection plates

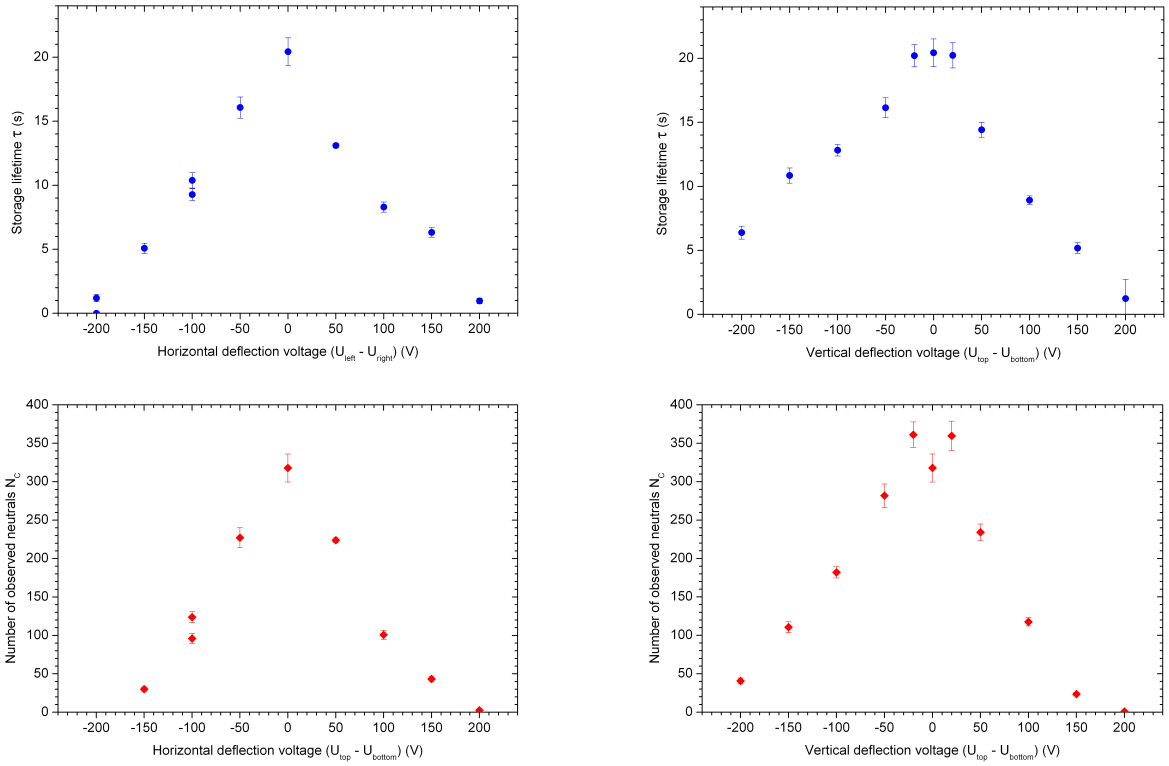

(a) Horizontal deflection

(b) Vertical deflection

Figure 4.12: *Storage lifetime and observed neutrals N_C as a function of the horizontal and vertical deflection voltages applied on the segmented pick-up (compare fig. 3.18). A N_2^+ ion beam was used with an energy of 7.1 keV.*

which have a distance of the pick-up diameter (4cm) and the same length. The assumed energy was 7.1 keV with N_2^+ just as used for the performed experiment.

The results are given in figure 4.12, which shows the storage lifetime and the number of observed neutrals as a function of the horizontal and vertical deflection voltages. The voltages are always given the difference between the voltages of the upper and lower plates, respectively, and the maximum voltages were ±100 V.

In all diagrams, a clear maximum at a zero voltage appears. The lifetime and the observed neutrals decrease strongly and symmetrically with a rising deflection. In summary, the central conclusion of this measurement is that the trap alignment has not changed significantly during the cool-down since the maximal lifetime appears at zero deflection voltage.

4.5.3 Influencing the short lifetime component

The appearance of a short lifetime component τ_s in addition to the normal longer lifetime τ_l has already been mentioned at the beginning of the section on the ion trapping measurements (see fig. 4.8 (b) and fig. 4.10). Under cryogenic conditions a systematic investigation of this observation has been performed. The short lifetime was found to be dependent on the injected ion bunch length and also the time when the trapping electrodes were switched on.
To summarize all the necessary information of the measurements, a complex diagram has been created in figure 4.14. First, the attention should be paid on the lengths and positions of the bars in horizontal direction, ignoring the colors for the moment. The plot represents the longitudinal extension expressed by the time of flight from turning on the beam cleaner voltage, valid for the time when the trapping electrodes are closed.
In the course of time, the ions initially leave the beam cleaner and pass the region of the switched electrode which is currently turned off ($\approx\ 14 - 15.5\,\mu s$). They cross the trap center and get reflected on the static trap side. Afterwards, the beam reaches again the center in opposite direction and the switched electrode region while leaving the trapping area ($\approx\ 22\,\mu s$).

The length of the bunches in comparison to the interval between the entrance electrodes indicates whether the ions are in the active trapping area and also the direction they are propagating. Considering the long lifetime component τ_l given on the y-aixs, one obtains a better lifetime for short ion bunches than for long bunches, where still many ions are on the way to the trap.
The short lifetime component τ_s is represented by the colors, where red stands for a value of 300 ms and yellow for no observed short lifetimeat all. The short bunches are mainly colored in yellow which indicates that no short lifetime was mostly observed for this type of bunches. More precisely, no short lifetime was observed whenever the end of the bunch has completely entered the trapping area.
As a consequence, an incoming ion bunch which is in the switched electrode region at the time when the trap is closed, causes a short lifetime component. A counter-propagating ion bunch at the same position does not generate this effect, and additionally in this case the long lifetime is improved.
To explain this behavior, some concepts have been developed. Ions situated inside the entrance electrode while it is being switched on are expected to gain kinetic energy by the changing electric field. This acceleration process leads to a shifted energy distribution of the trapped ions. Ions with less energy than the borders of the potential can still be

trapped, but probably in more unstable trajectories with a time scale of the observed short lifetime.
Another possibility is the deflection of these ions by the rising electric field, where the deflected fraction of the bunch spreads out and impinges on the chamber walls or electrodes. Under cryogenic conditions, gases like nitrogen or oxygen, for instance, are frozen out on this cold surfaces and get desorbed by the energetic ions. The result is a temporarily worsening of the pressure and a faster decay of the trapped ions.
The concept of accelerated ions and metastable trajectories should be a pressure and temperature independent process, but the short lifetimes have changed by approximately two orders of magnitude between warm and cold measurements (compare fig. 4.8 (b)). On the other hand side, the observation at room temperature can not be explained by desorption of frozen gas. Hence, a combination of both processes could be possible.

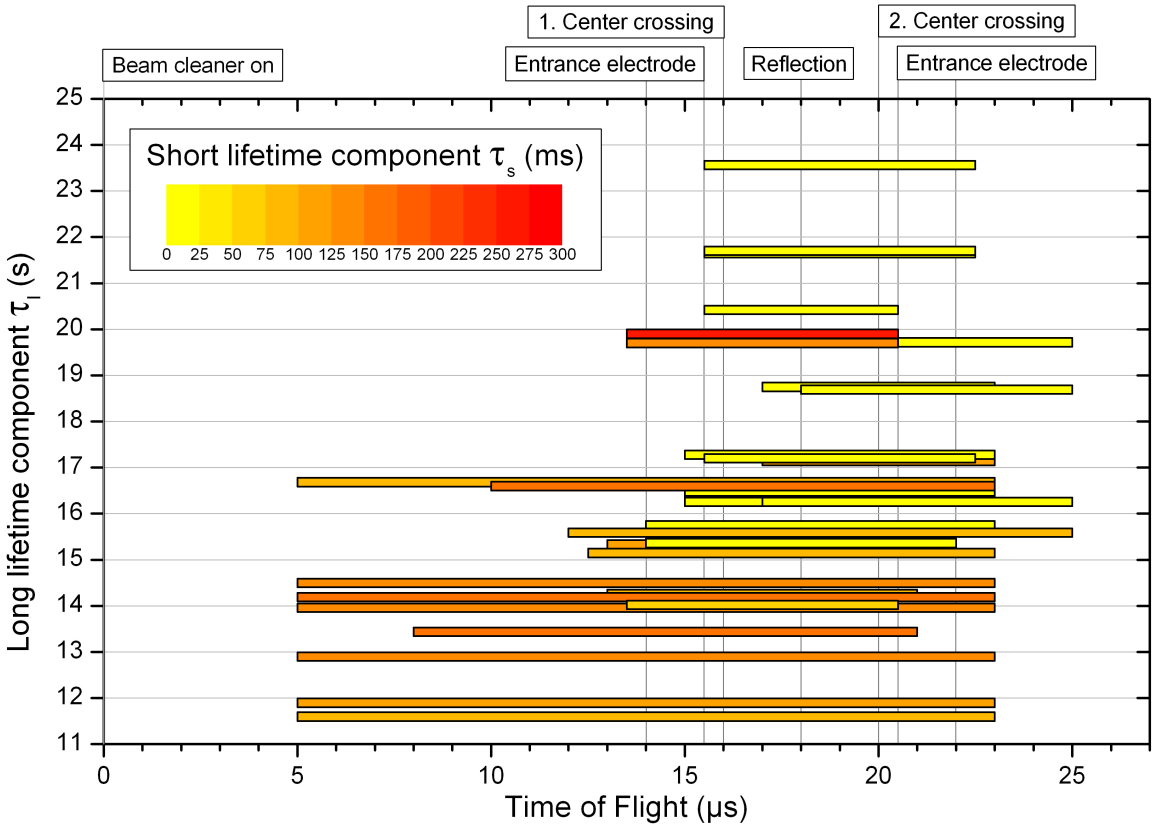

Figure 4.13: *Position and length of ion bunches at the time when the trap electrodes have been switched on with respect to the trap location. The long storage lifetime component τ_l is plotted on the axis and the short component τ_s is shown via the colors. N_2^+ ions with an energy of 7.1 keV have been used.*

Furthermore, the improved long lifetime component for short ion bunches could indicate a long time effect of the changed pressure.
Finally, a systematic investigation at room temperature similar to this measurement has to be done to gain a better understanding of these processes.

4.5.4 Changing pressure to explore trap properties

To explore the trap properties, in particular the storage lifetime, dependent on the vacuum at cryogenic temperatures two types of methods have been used to change the pressure.
In section 4.1 it has been mentioned that at cryogenic temperatures the turbo pump below the CTF for the experimental vacuum has not been used, because the pressure in this region would increase with a connected turbo pump.
For this measurement, the valve which normally separates the experimental vacuum and turbo pump, has been opened to provide a higher pressure. Turbo pumps are particularly suited for pumping heavier gas molecules like nitrogen or oxygen, so the opening releases mainly hydrogen which is also the dominant residual gas component. The intention of this process was to keep the cross sections for the involved loss processes constant and observe only the pressure dependence.
Figure 4.14 shows the measured pressure below the CTF and the determined storage lifetime as a function of the time in hours. Starting at $3 \cdot 10^{-11}$ mbar, the pressure quickly increases by two orders of magnitude. After half an hour, the pressure has decreased again and approaches an equilibrium value of approximately $4 \cdot 10^{-10}$ mbar. The closing procedure lead to a short-term increase in the pressure due to the movement of the valve then slowly approaches the initial pressure.
The corresponding storage lifetime represented by the blue data points shows a spread during this time of roughly 10 % but it stays constant within the plotted statistical error. The conclusion of this measurement is either a pressure independent storage lifetime within this range or the pressure did not change in the trapping area. A dominant pressure independent loss process would exclude electron capture or multiple scattering. This behavior could be an indication of a lifetime limitation due to electrode voltage fluctuations.
The second explanation can not be ruled out considering the distance between the pressure measurement in warm region and the trap at cryogenic temperature. The additional gas stream could possibly not reach the trapping area. Moreover, the gas molecules have to be reflected several times on the cold chamber walls between the ion trap and the gauge and condensate. On the other hand, this process could also lead to a desorption of frozen

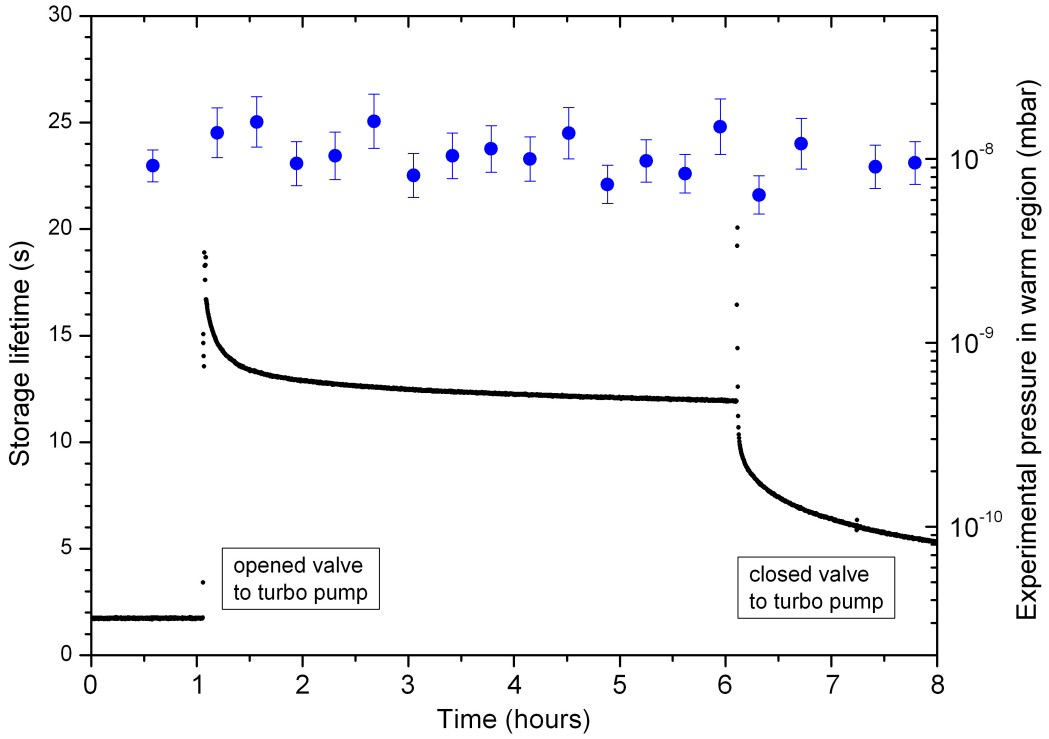

Figure 4.14: *Changing pressure conditions by opening the turbo pump valve to explore the lifetime dependence. The lifetime measurement was performed with N_2^+ at 7.1 keV.*

gases by the warm gas stream.

Thus, in summary, the measurement indicates a pressure-independent loss process which probably limits the storage lifetime in this range.

As a second pressure changing experiment, the radiation flap to the pumping section below the CTF was opened for several hours. The flap is located in the experimental vacuum below the pumping chamber and cooled by the 40 Kelvin helium pipe (compare fig. 3.13). Hence, the ion gauge used for the pressure measurements is separated by the flap from the inner vacuum. It must be pointed out that the flap is not sealing but rather screening the inside from room temperature radiation.

In the corresponding data shown in figure 4.15, the measured pressure in the warm region initially increased when the radiation flap was opened. The room temperature radiation impinging upon the cold chamber walls inside will desorb frozen gas from the cold surfaces which was then detected by the gauge. After a while, for instance, the reachable cold chamber walls are emptied from frozen gas and the pressure decreases again. The pump stand also has access to the cryogenic pumping abilities of the CTF and the pressure

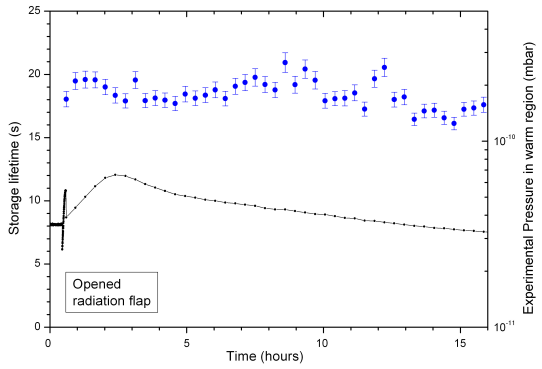

(a) Storage lifetime (N_2^+, 7.1 keV) and experimental pressure measured in warm region below the CTF

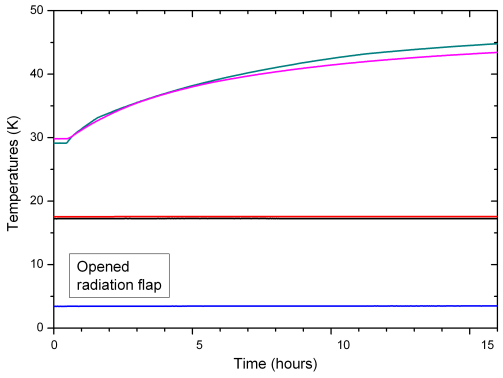

(b) Corresponding temperature changes on the cold chamber: Upper temperatures were measured in the pump chamber (right side in fig. 4.3), lower temperatures at other locations on the cold chambers

Figure 4.15: *Changing pressure conditions by opening the radiation flap to explore the lifetime dependence*

tends to decrease to an even lower pressure than initially.
This shows that the pressure inside must have been lower than measured on the outside and in addition, the pressure estimations given in figure 4.9 predict a higher pressure. This again could indicate that the previously determined lifetimes at cryogenic temperatures do not reflect the pressure conditions in the trapping area.
Considering the lifetime for this measurement, it is not influenced by the pressure changes detected outside. As in the first pressure changing experiment, the reasons could be a pressure independent loss process or the trapping area was not effected by this.
Finally, in figure 4.15 (b) the corresponding temperatures of the cold chambers are shown. The two upper temperatures have been directly measured at the cold chamber above the pump stand and show a warming of the cold chamber due to the radiation. The temperatures below are measured at other positions of the cold chambers, for instance, the middle chamber or cooling unit, and stay constant for this time. So the heat input seems to influence only the chamber above the flap.

4.5.5 Lifetime dependencies for different loss processes

The influences of the various loss processes on the total storage lifetime can be accessed through their different energy dependences. The results of the energy dependent lifetime

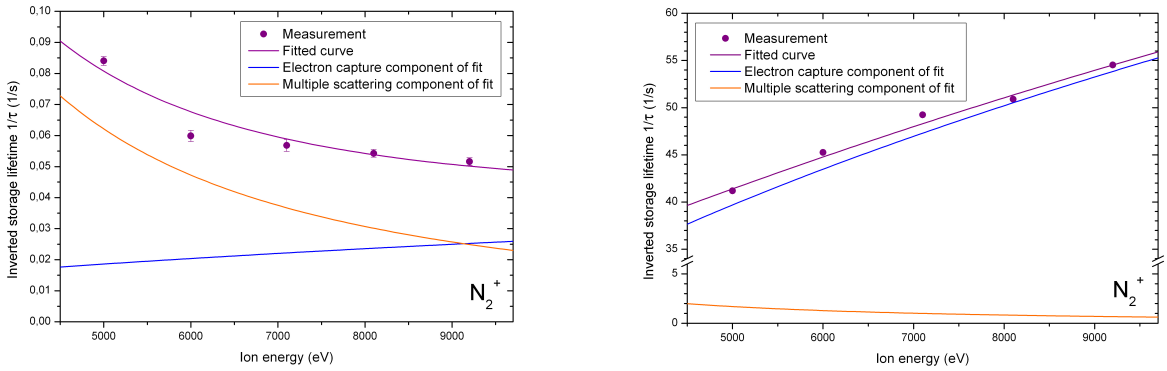

(a) Cryogenic temperatures

(b) Room temperature

Figure 4.16: *Inverted storage lifetime as a function of the ion energy with fitted curves using the energy dependence of electron capture and multiple scattering (eqn. 2.19 and 2.23).*

measurements are given in figure 4.16, where the left side shows the observations under cryogenic conditions and the right side the room temperature measurements.
At first, it should be noted that the inverted storage lifetime is plotted because the different lifetime components are also summed reciprocally. The given ion energies correspond to the mean injection energy of the ions.
For the cryogenic case, the inverted lifetime decreases with the energy while for the warm measurement it increases. This behavior directly indicates that the multiple scattering process is dominate for cold temperatures and, conversely, the electron capture for room temperature, if we would assume that only these two processes contribute (compare equations 2.19 and 2.23).
Fitted curves are also shown in the diagram, where for both cases only the two mentioned processes have been taken into account together with their corresponding energy dependences. In the cryogenic case, the multiple scattering component for low energies is over a factor of three higher than the electron capture process and at the upper end of the measured energy range they become equal. In contrast, for warm temperatures, meaning higher pressure, the electron capture process is by far the dominating one.
If one assumes that the proportionality between the electron capture rate and the pressure can be derived from the warm measurements (Fig. 4.16), one can calculate a pressure estimation for the cold case. The result one obtains is $4.26 \pm 0.94 \cdot 10^{-11}$ *mbar* which agrees with the pressure estimation from the cool-down measurement (sec. 4.4).
Furthermore, a lifetime analysis has been performed by changing the focus of the injected ion beam into the trap via the voltage on the second einzel lens. This einzel lens is the last ion optical element before the trap entrance and is mainly responsible for focus into

the trap acceptance (compare fig. 3.17).
The fitted storage lifetimes as well as the corresponding amplitudes A_C are shown in figure 4.17 for the cryogenic and warm case in comparison. Using equations (2.26) and (2.27), the amplitude is proportional to the number of trapped ions N_0 if the detection efficiency ϵ and the electron capture lifetime τ_C stayed constant. This is valid if the electrode voltages and hence, the trap acceptance as well as the pressure have not changed for the measurement.
The amplitude shows a clear maximum at almost the same position in both cases. For this voltage of roughly 3.5 kV, the best focusing could be achieved and a maximum number of ions were trapped.
In case of the low pressure measurements on the left side, the storage lifetime stays nearly constant but with a small minimum. A decreasing lifetime for a high ion density indicates the loss process due to intrabeam scattering. Usually for a storage ring, the decay is not exponential, and after the density has decreased under a critical value the process becomes less important.
However, this non-exponential part was not observed in the measurements. In case of the trap, the ion density is additionally increased at the point of return where the kinetic ion energy gets rather small. Accordingly, the intrabeam scattering could stay important for a longer time scale during the ion trapping as the main ion losses due to this process occur at the returning points.
The storage lifetime measurements at warm conditions on the right side of figure 4.17 show a slight maximum which indicates a dependence on the multiple scattering process. The improved focusing of the ions into the trap acceptance leads an enhanced time until they are scattered out. The maximum appears very small and combined with the previous energy measurements, electron capture is still the dominant loss process for high pressures as intrabeam scattering would be negligible.
Another method to estimate the pressure for cryogenic conditions can be realized by comparing the fitting amplitudes of the lifetime curves for cryogenic and warm temperatures. Combining the equations (2.26) and (2.27), the fitted amplitude A_C is given by

$$A_C \;=\; 1/2\,\epsilon\,N_0\,\frac{1}{\tau_C}\,. \tag{4.1}$$

Using the definition of the electron capture lifetime (eqn. 2.19), one obtains that the amplitude A_C is proportional to the residual gas density, if the detection efficiency ϵ and the number of initially trapped ions N_0 stay constant. Under these conditions, the ratio of the amplitudes for low and high pressures can be created, leading to a simple equation

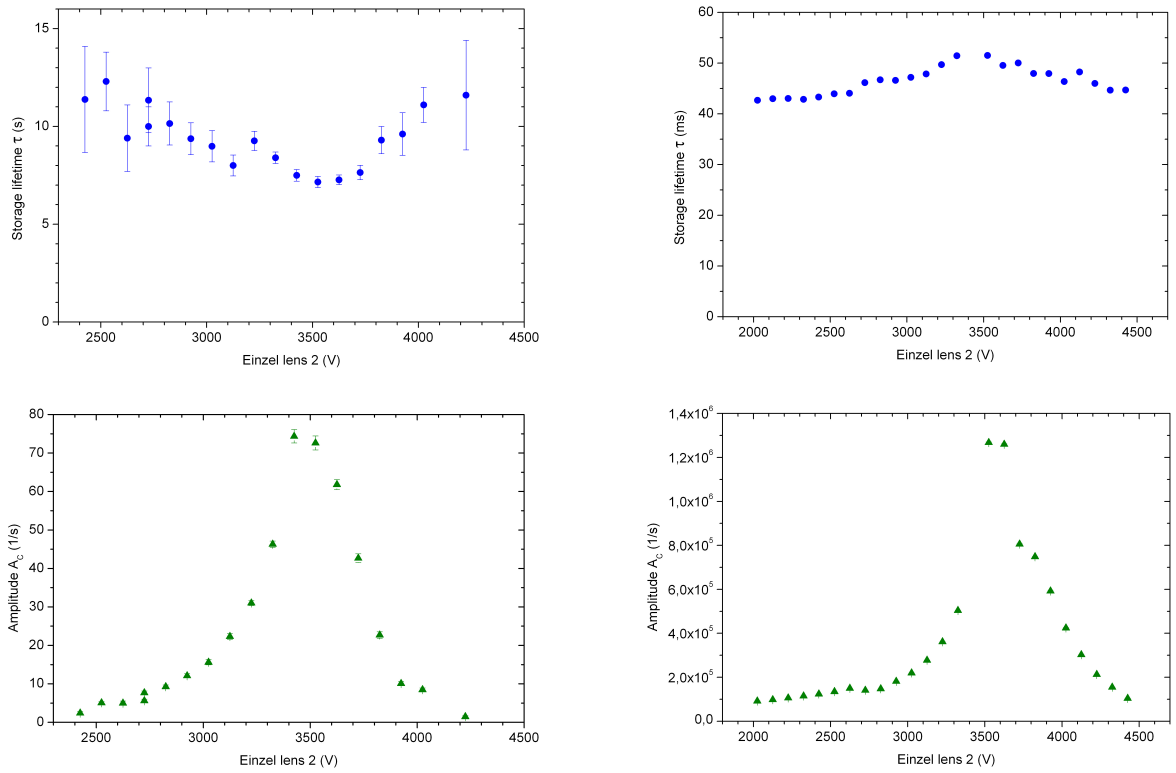

(a) Cryogenic conditions

(b) Warm conditions

Figure 4.17: *Storage lifetime and fitted amplitude A_C as a function of the voltage on einzel lens 2 which changes the injection focus. The amplitude is proportional to the total number of trapped ions because the electrode voltages and the pressure stayed constant.*

for the residual gas density at cold temperatures:

$$n^{cold} = \frac{A_C^{cold}}{A_C^{warm}} n^{warm} . \tag{4.2}$$

Here, n^{cold} and n^{warm} are the residual gas densities for different temperatures; A_C^{cold} and A_C^{warm} the corresponding amplitudes, respectively.
A value of $A_C^{warm} = 1.27 \cdot 10^6\, s^{-1}$ can be determined by using the maximum of the room temperature measurement in figure 4.17. Section 4.5.2 has shown that the alignment of the trap and also the trap acceptance have not changed during the cool-down. Hence, the amount of initially trapped ions at cryogenic temperatures is almost the same as at room temperature. In addition, for the cold temperature measurements neither the trap voltages or ion optics settings have been changed and so the requirements on equation 4.2 are satisfied. The amplitude for the low pressure case is $A_C^{cold} = 72.6\, s^{-1}$.
The corresponding residual gas density and the pressure at room temperature are

$n^{warm} = 2.4 \cdot 10^{14}\, 1/m^3$ and $p^{warm} = 1 \cdot 10^{-8}\, mbar$, respectively. Using these values one obtains a residual gas density at cryogenic conditions of $n^{cold} = 1.4 \cdot 10^{10}\, 1/m^3$, according to a pressure of $5.7 \cdot 10^{-13}\, mbar$.
For this residual gas densities, the expected storage lifetime is in the order of 1000 seconds which far more than the measured value of 24 s. These discrepancies can be explained by the appearance of a pressure independent lifetime most likely induced by the voltage fluctuations on the high-voltage switches. This lifetime has to be in the order of the measured 24 seconds and hence, can not be detected at room temperature. For higher energies these fluctuations are less noticeable which would agree with figure 4.16. Furthermore, for an enlarged trap acceptance the fluctuations should have also less influence on the storage lifetime which has been realized in the measurement of figure 4.11 and shows the described behavior.
The recent storage lifetime measurements at cryogenic temperatures with a previously baked CTF and reduced noise on the high-voltage switches have shown an improvement to around 165 seconds.

5. Conclusions and outlook

In this work, the setup of the new electrostatic Cryogenic Trap for Fast ion beams (CTF), which was mainly constructed to explore cooling techniques and test thermal couplings for the development of the Cryogenic Storage Ring (CSR), has been presented.
The first successful cryogenic cooling tests have been accomplished with an expected final temperature of 2 Kelvin in the cooling units. After the cooling process had been automated by a regulation loop in the control system of the refrigerator, a well controlled cool-down could be achieved. The average temperature of the inner vacuum chamber has been determined to be 17 K, where some improvements still have to be done for the thermal coupling of the CSR to reach at least 10 K. In particular, the heat radiation and conduction input at the entrance and exit as well as at the connection to the pumps below the CTF have to be reduced. At the 40 and 80 Kelvin radiation shields, mean temperatures of 36 K and 70 K, respectively, could be obtained which is below the respective design temperatures.
Accordingly, the trapping of energetic ion beams between 2 and 9 keV have been accomplished by using initially a positive Argon ion beam and a singly charged molecular nitrogen ion beam for further measurements. After storage optimization processes at room temperature, the CTF has been cooled to cryogenic temperatures preforming storage lifetime measurements in parallel. The correlation of the dominant ion storage loss processes and the pressure has been observed which is manifested in a linear dependence of the measured inverted storage lifetime on the pressure. To estimate the extremely high vacuum conditions expected at cryogenic temperatures, the pressure has been calculated with the aid of the determined linear pressure dependence and the measured storage lifetime. This was found to be 15 seconds for an ion energy of 5 keV using trapped nitrogen ions. The pressure was determined to be about $5 \cdot 10^{-11}$ mbar.
During several cryogenic ion trapping measurements, the unchanged alignment of the trap at cold temperatures has been verified, and a study of the previously observed short lifetime component at room temperature was performed. Storage lifetime measurements with different ion energies gave the opportunity to determine the dominant ion loss process for

different pressure conditions which are multiple scattering at at cryogenic temperatures and electron capture at room temperature, respectively.
Furthermore, a pressure variation measurement at cryogenic temperatures has indicated a pressure independent lifetime besides the two mainly expected loss processes mentioned before. A limitation of the total storage lifetime due to this process is very likely the reason leading to a higher pressure estimation than expected. This loss process has probably been identified to be induced by voltage fluctuations on the high-voltage switches of the trap electrodes.
After their reduction, the storage lifetime for an ion energy of 7.1 keV has recently improved to 165 seconds corresponding to a pressure of the order of 10^{-12} mbar. One has to note that for this second measurement period, the CTF has been baked successfully before the cool-down which has reduced the pressure at room temperature by more than one order of magnitude.
By means of another method to estimate the pressure at cold temperatures, which compares the amplitudes of the fitted lifetime curves, a pressure of $6 \cdot 10^{-13}$ mbar could be obtained. Combined with the higher pressure estimation of the linear lifetime correlation, the fluctuations on the trap electrode voltages and the improved lifetime after their reduction, it is most likely that an pressure of the order of 10^{-13} mbar has already been achieved which has not been reflected in the lifetime due to the limitation process.
Further investigations have to be done in order to verify whether the improved lifetime is due to the previous baking process of the CTF and the corresponding pressure improvement at room temperature [22].
However, possible high-voltage fluctuations on the switched electrostatic deflectors are not expected to be a significant problem in the CSR. Only one 6° deflector will be switched to inject the ions into the ring and its short length compared to the ring circumference will not lead to a strong influence on the stored ions. Moreover, this effect can be compensated by the aid of the electron cooler which pushes the ions back towards the center of the acceptance.
As mentioned before, further investigations have to be performed in terms of achieving a longer storage lifetime in the order of 1000 seconds corresponding to the anticipated room temperature equivalent pressure of 10^{-13} mbar in the (10^{-15} mbar range at around 10 K). In addition, more investigations like the experimental determination of the tune or the improvement of the self-bunching mode of the trap will be performed, for which not enough time could be provided.
Furthermore, an investigation of trapped Al_4^- ion clusters will be performed where the cluster temperature will be determined as a function of the trapping duration. The highly

internally excited ions produced in an ion sputter source will cool due to the low black-body radiation field in the cryogenic trapping area. However, the initial internal energy distributed over several rotational and vibrational states can not lead to a detachment of the outer electron. To probe the internal excitation, after different trapping durations the ion clusters will be further excited by a laser beam. Equipped with enough internal energy, the ion clusters will detach the electron. The lower their current excitation at the time of the laser pulse will be, the longer the electron emission process will take and thus, the cluster temperature can be determined.
This investigation has already been performed in a non-cooled ion beam trap by observing the cooling Al_4^- cluster ions for a temperature range of 1400 down to 500 Kelvin [23]. The cryogenic conditions of the CTF give the opportunity to observe the radiative cooling even down to 10 Kelvin.
Finally, the CTF will be moved to a different location to make space for the building and assembly of the CSR, which will commence in May 2009. The CTF will be further operated as a test facility for CSR and also for new scientific investigations. Hence, a new helium pipe connection from the refrigeration system will be installed to cool the device.

Appendix

A CTF with injection line

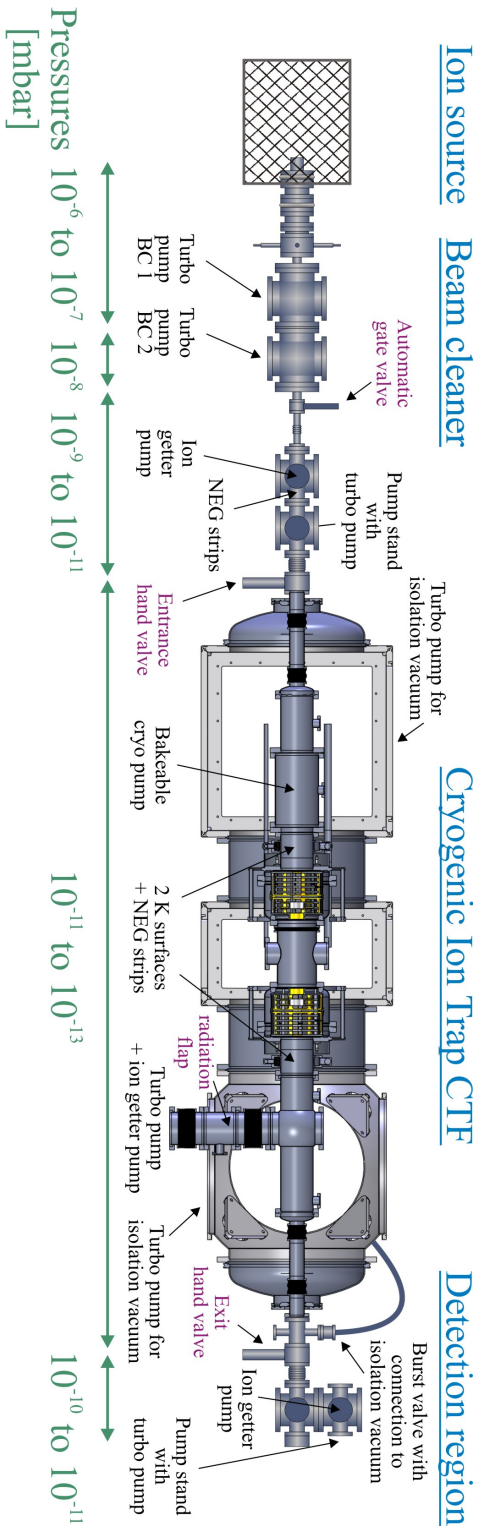

Figure A.1: *CTF vacuum system*

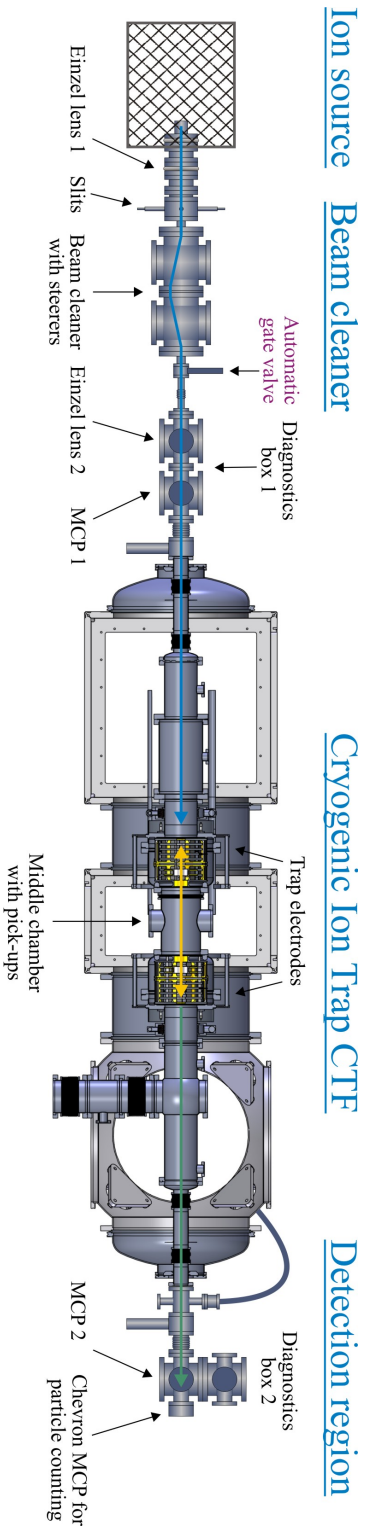

Figure A.2: *CTF with ion optics and diagnostics*

B CTF temperature observation program

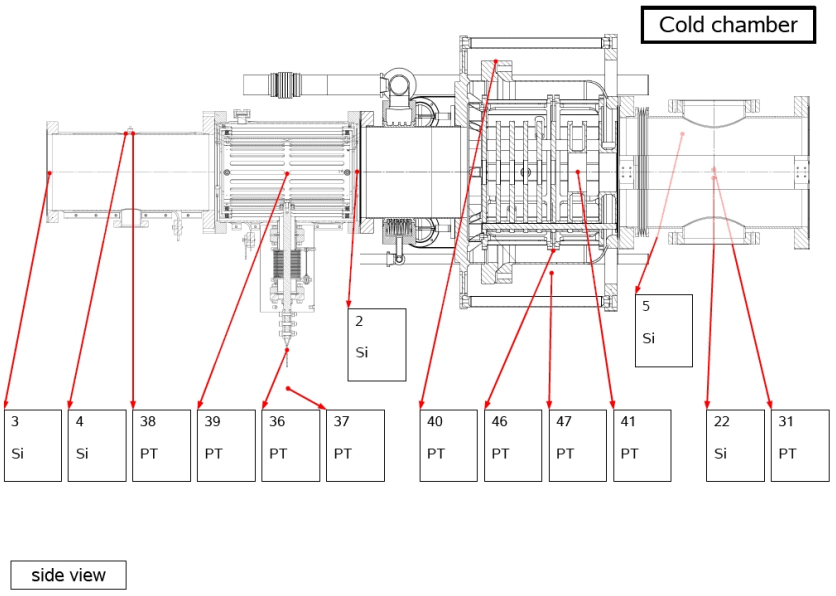

Figure B.1: *Temperature locations on the left side of the CTF*

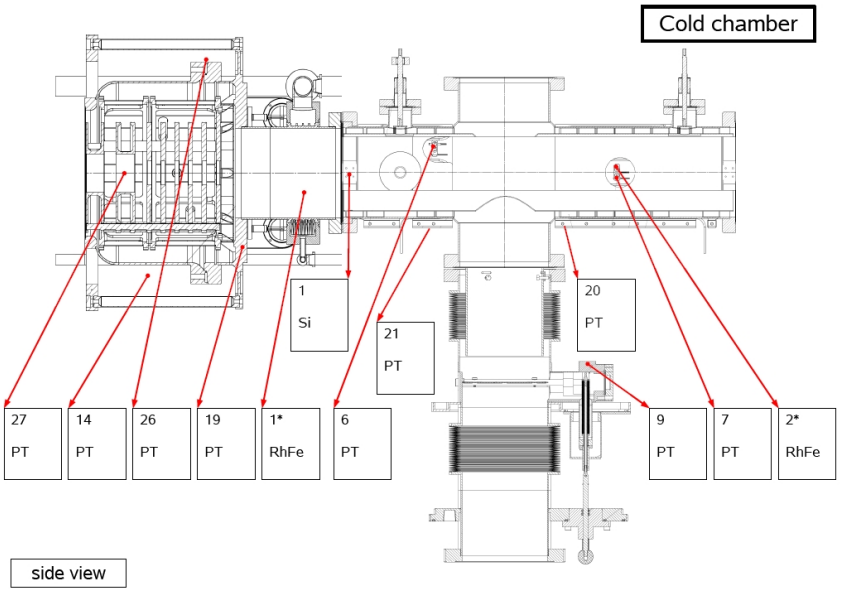

Figure B.2: *Temperature locations on the right side of the CTF*

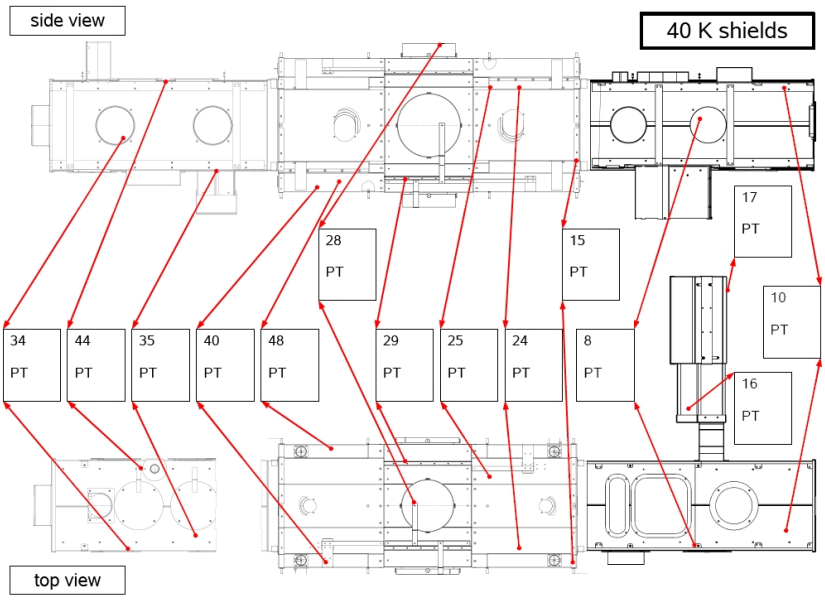

Figure B.3: *Temperature locations on the 40 K radiation shields of the CTF*

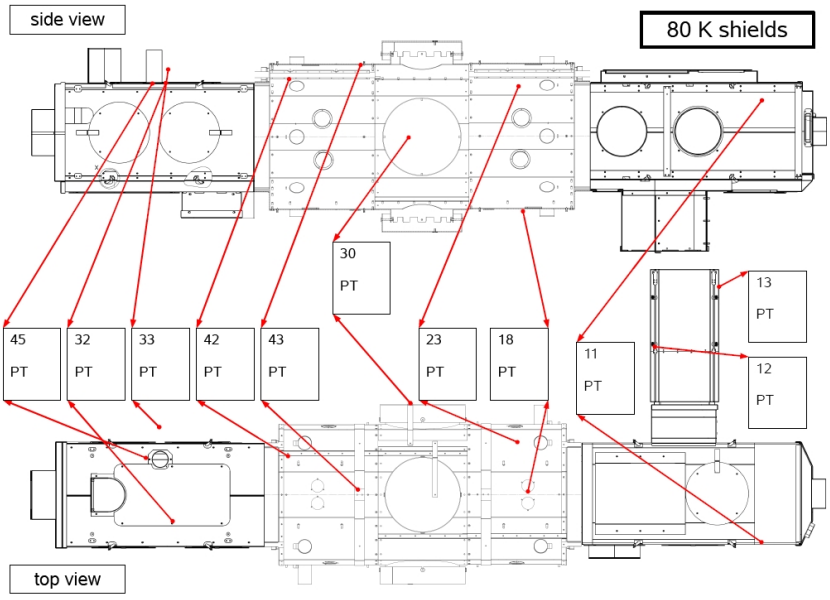

Figure B.4: *Temperature locations on the 80 K radiation shields of the CTF*

C SIMION simulations

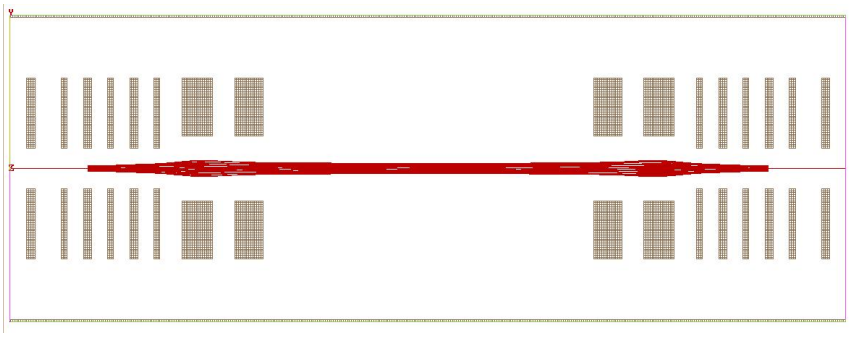

Figure C.1: *Stable trajectory of one N_2^+ ion with 7.1 keV energy simulated with SIMION*

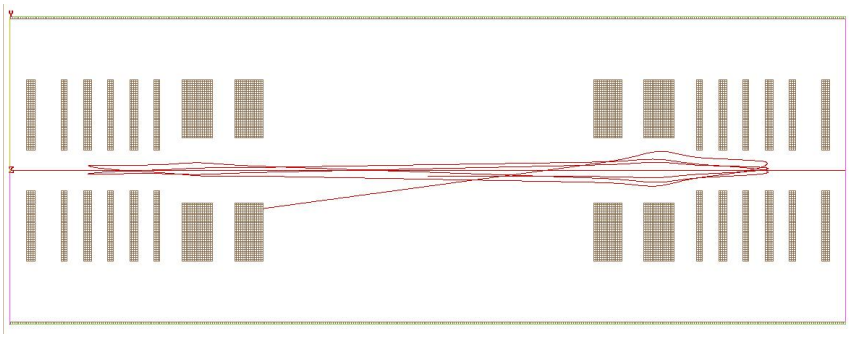

Figure C.2: *Unstable trajectory of one N_2^+ ion with 7.1 keV energy simulated with SIMION*

References

[1] L. H. Andersen, O. Heber and D. Zajfman, *Physics with electrostatic rings and traps*, J. Phys. B: At. Mol. Opt. Phys. **37** (2004), R57–R88.

[2] S. P. Møller, *ELISA, an electrostatic storage ring for atomic physics*, Nucl. Instr. and Meth. in Phys. Rev A **394** (1997), 281–286.

[3] T. Tanabe, K. Chida, K. Noda, I. Watanabe, *An electrostatic storage ring for atomic and molacular science*, Nucl. Instr. and Meth. in Phys. Rev A **482** (2002), 595–605.

[4] D. Zajfman, O. Heber, L. Vejby-Christensen, I. Ben-Itzhak, M. Rappaport, R. Fishman, and M. Dahan, *Electrostatic bottle for long-time storage of fast ion beams*, Phys. Rev. A **55** (1996), 1577.

[5] H. B. Pedersen, S. Altevogt, B. Jordon-Thaden, O. Heber, M. L. Rappaport, D. Schwalm, J. Ullrich, D. Zajfman, R. Treusch, N. Guerassimova, M. Martins, J.-T. Hoeft, M. Wellhöfer and A. Wolf, *Crossed Beam Photodissociation Imaging of HeH^+ with Vacuum Ultraviolet Free-Electron Laser Pulses*, Phys. Rev. Lett. **98** (2007), 223202.

[6] A. Wolf, K. G. Bhushan, I. Ben-Itzhak, N. Altstein, D. Zajfman, O. Heber and M. L. Rappaport, *Lifetime measurement of He^- using an electrostatic ion trap*, Phys. Rev. A **59** (1999), 267.

[7] A. Diner, Y. Toker, D. Strasser, O. Heber, I. Ben-Itzhak, P. D.Witte, A.Wolf, D. Schwalm, M. L. Rappaport, K.G. Bhushan and D. Zajfman, *Size-Dependent Electron-Impact Detachment of Internally Cold C_n^- and Al_n^- Clusters*, Phys. Rev. Lett. **93** (2004), 063402.

[8] D. Zajfman, Y. Rudich, I. Sagi, D. Strasser, D.W. Savin, S. Goldberg, M. Rappaport, O. Heber, *High resolution mass spectrometry using a linear electrostatic ion beam trap*, Int. J. Mass Spectrom. **229** (2003), 55–60.

[9] S. Krohn, Z. Amitay, A. Baer, D. Zajfman, M. Lange, L. Knoll, J. Levin, D. Schwalm, R. Wester, and A. Wolf, *Electron-induced vibrational deexcitation of H_2^+*, Phys. Rev. A **62** (2000), 032713.

[10] M. Lange et al., *Commissioning of the Heidelberg Cryogenic Trap for Fast ion beams (CTF)*, Proc. Europ. Part. Accel. Conf. (EPAC) 2008, Genova, Italy.

[11] T. Sieber et al., *Beam Diagnostics for the Prototype of the Cryogenic Storage Ring CSR*, Proc. Europ. Part. Accel. Conf. (EPAC) 2008, Genova, Italy.

[12] A. Wolf et al., *The Heidelberg CSR: Low-Energy Ion Beams in a Cryogenic Electrostatic Storage Ring*, Proc. COOL05, Galena, USA (2005).

[13] R. v. Hahn et al., *Status of the low energy electrostatic Cryogenic Storage Ring CSR at MPI-K in Heidelberg, Advances in Cryogenic Engineering*, AIP Conference Proceedings 823, Prague (2006).

[14] D. Orlov et al., *Cryogenic and vacuum technological aspects of the low energy electrostatic Cryogenic Storage Ring*, Proc. ICEC2007, Chattanooga, USA (2007).

[15] R. v. Hahn et al., *The Cryogenic Storage Ring Project at Heidelberg*, Proc. Europ. Part. Accel. Conf. (EPAC), Genova, Italy (2008).

[16] D. A. Dahl, *Current status and final design of the Cryogenic Storage Ring in Heidelberg, Germany*, Int. J. Mass. Spect. (2000).

[17] J. R. Sheridan, T. Merlo, and J. A. Enzweiler, *Cross Sections for Asymmetric Charge Transfer and Collisional Dissociation Reactions of Atmospheric Ions at keV Energies*, J. Geophys. Res. **84** (1979), 7302–7306.

[18] P. O. Haugsjaa, R. C. Amme, N. G. Utterback, *Charge-Transfer Cross Sections for N2+ Ions Incident on H2 and D2 between 20 and 1000 eV*, J. Chem. Phys. **49** (1968), 4641–4643.

[19] S. N. Ghosh, W. F. Sheridan, *Experimental Determinations of Charge Transfer Cross Sections and Secondary Electron Emission by Ion Bombardment*, J. Chem. Phys. **26** (1957), 480–485.

[20] N. G. Utterback and G. H. Miller, *Fast Molecular Nitrogen Beam*, Rev. Sci. Instrum. **32** (1961), 1101–1106.

[21] W. Hardt, *A few simple expressions to check vacuum requirements in a proton synchrotron*, Cern report, ISR-300/GS/68-11 (1968).

[22] M. Froese et al., *Current status and final design of the Cryogenic Storage Ring in Heidelberg, Germany*, Part. Accel. Conf. (PAC) 2009, Vancouver, Canada, to be published.

[23] Y. Toker, O. Aviv, M. Eritt, M. L. Rappaport, O. Heber, D. Schwalm, and D. Zajfman, *Radiative cooling of Al_n^- clusters*, Phys. Rev. A **76** (2007), 053201.

[24] D. Strasser, O. Heber, S. Goldberg and D. Zajfman, *Self-bunching induced by negative effective mass instability in an electrostatic ion beam trap*, J. Phys. B: At. Mol. Opt. Phys. **36** (2003), 953–959.

Danksagung

An dieser Stelle möchte ich mich bei allen bedanken, die die Entwicklung dieses Projektes und meine damit verbundene Diplomarbeit vorangetrieben haben:

Der erste herzliche Dank richtet sich an Prof. Andreas Wolf, der mir überhaupt diese Diplomarbeit ermöglicht hat und mir mit seiner hervorragenden Betreuung und den gründlichen Korrekturen dieser Arbeit sehr geholfen hat. Des weiteren, danke ich Prof. Klaus Blaum für die Unterstützung dieses Projektes und für die Bereitschaft die Zweitkorrektur dieser Arbeit zu übernehmen.

Außerdem möchte ich mich bei Robert von Hahn für die vielfach bewilligten Verschiebungen des Aufwärmvorgangs bedanken, die durch so allerlei interessante und verblüffende Messungen begründet wurden und natürlich für die geduldigen Erklärungen bezüglich Kälteanlage und CSR-Konzept.

Bei den drei Kollegen Mike Froese, Michael Lange und Jozef Varju möchte ich mich für die waghalsigen Kletterpartien an der CTF und die lustigen "Peanutbutterjellytimes" bedanken, die wir zusammen neben anstrengendem Schraubendrehen und unzähligen Lebesdauermessungen verbracht haben. Ganz besonderer Danke gebührt meinem kanadische Kollegen Mike, der unter anderem diese Arbeit vor englischen Ausrutschern bewahrt hat und für die langen Diskussionen über mögliche Geister in der Falle aufgrund von merkwürdigen Messergebnissen.

Bei Manfred Grieser möchte ich mich für die geduldigen Erklärungen und die Hilfe bei den Berechnungen und Simulationen bedanken.

Ich danke Dmitry Orlov unter anderem für seine Hilfe mit dem Vakuumsystem und der Kryopumpe, sowie für die vergnügliche Zeit auf der Reeperbahn.

Thomas Sieber und Felix Laux danke ich für die Unterstützung bei Messungen mit dem Pick-up und insbesondere Thomas für den Aufbau des Injektionssystems und der Ionendetektion.

Außerdem geht ein großer Dank an Dirk Kaiser und Michael Frauenfeld, die unter anderem immer geduldig Modifikationen an störrischen Schildteilen vorgenommen haben und auch sonst immer für ein angenehmes Arbeitsklima gesorgt haben.

Meinen beiden Bürokollegen Robin Bastert und Florian Fellenberger (natürlich auch Mike) möchte ich für die vielen Tipps und Aufmunterungen beim Schreiben dieser Arbeit danken (R.:"Hey, ich hab schon 30 Seiten, obwohl ich erst vor einem halben Jahr angefangen hab...").

Der Kochgruppe danke ich für die hervorragenden Gerichte und die angenehme Mittagsatmosphäre, die mich regelmäßig vor alternativem Essen bewahrt hat.

Zuletzt möchte ich mich herzlich bei meinen Eltern bedanken, die mich immer unterstützt, mir dieses Studium überhaupt ermöglicht haben und lange versucht haben zu verstehen was und warum ich das hier überhaupt mache. Des weiteren möchte ich meine Schwester hier nicht unerwähnt lassen, bei der ich nicht dieses Interesse an der Naturwissenschaft wecken konnte, die aber trotzdem ihren eigenen glücklichen Weg gehen wird.
Zum Finale diese Familienabschnittes geht ein ganz lieber Dank an meine Freundin, die mich immer unterstützt hat und viel Verständnis für meine zunehmende Abwesenheit hatte.

Erklärung:

Ich versichere hiermit, daß ich diese Arbeit selbständig verfaßt und keine anderen als die angegebenen Quellen und Hilfsmittel benutzt habe.

Heidelberg, den .....

.....
(Unterschrift)